

**Department of Urban Innovation**  
**Specialization in Coastal Engineering**  
**Yokohama National University**



**A comprehensive study on beach morphology, pore water  
pressure gradient and local acceleration in association of  
numerical and statistical simulations**

By

**Mohammad Tabasi**

A dissertation submitted in partial fulfillment of the requirements for the degree  
of Doctor of Philosophy in Engineering

Academic Advisor: Prof. Takayuki SUZUKI

September, 2022

## **Abstract**

The thesis can be broadly divided into several coastal-related types of research to investigate the bed response in the nearshore zone. In the beginning of this study, a barred beach profile was constructed and installed in a small-scale laboratory wave flume. The beach profile was composed of a fixed profile containing a sandpit in the middle part of the flume. Different wave conditions were provided to evaluate the effect of sediment compaction on the vertical pore water pressure and sediment suspension. The pressure gradients were achieved by finite difference of measurements from an array of transducers.

The magnitude of pore water pressure, pressure gradient, and sediment concentration with low and high sediment compaction were compared. In general, the magnitude of pressure gradients within the sediment layers with high compaction were larger compared to the low compaction conditions. Similarly, the recorded pore water pressure and sediment concentration were examined, and different behaviors such as the differences in the magnitude of the pore water pressure and pressure gradients due to different sediment compaction levels under almost the same hydrodynamic conditions were observed. The average of peak pressure gradients within the sediment layers under high compaction conditions was 1.4 times larger than the low compaction conditions. These results indicate the necessity of a detailed investigation of sediment's influence on pore water pressure gradient and sediment concentration.

Wave-induced pressure gradients and local accelerations are important interconnected physical mechanisms involving several hydrodynamic and morphodynamic coastal phenomena. Therefore, to provide a reliable and realistic hydrodynamic and morphodynamic simulation, the dependencies among different parameters, such as water level, pressure gradient, local acceleration, and sediment concentration should be considered. Herein, a copula-based simulation is

presented for modeling multivariate parameters and maintaining their statistical characteristics within the surf zone. Archimedean and elliptical copula families are applied to investigate the dependency construction between the parameters in two case studies: one from a field site on the east coast of Japan, and another from a large-scale laboratory barred beach profile.

The dependency between variables is evaluated using Kendall's  $\tau$  correlation coefficient. The water level, pressure gradient, and local acceleration are shown to be significantly correlated. The correlation coefficients between the variables for the natural beach are lower than the laboratory data. For the laboratory data, the correlation coefficients are very close to 1. For the field data, the highest correlation coefficient values achieved for the water level and pressure gradient. The marginal probabilistic distribution functions and their joint probabilities are estimated to simulate the variables using a copula approach. The performance of the simulations is evaluated via the goodness-of-fit test. The analysis shows that the laboratory data are comparable to the field measurements, implying that the laboratory simulation results can be applied universally to model multivariable joint distributions with similar hydrodynamic conditions. The Generalized Extreme Value (GEV) distribution as a TCDF with three parameters showed excellent agreement with the laboratory experimental data. Meanwhile, the Extreme Value (EV) and logistic distributions with two parameters indicated excellent trends for the Empirical Cumulative Distribution Functions (ECDFs) involving the laboratory data, unlike the case for the field dataset calculations. However, the GEV distribution required two empirical parameters, and compared with the EV and logistic distributions, the computational procedure was more complicated.

Next, for investigating the bed response in the surf zone area. A statistical approach, the copula approach, has been exploited to simulate the dependent variables for coastal applications. A computer program was written and performed

in MATLAB for copula simulation. This program is consisted of several modules to achieve reasonable results. The pressure gradient was a key parameter investigated and simulated in this part of the study to simulate the bed response. Field, large, and small-scale laboratory datasets were used to validate the model performance. A small-scale laboratory experiment was conducted at Yokohama National University's Coastal Engineering laboratory to measure and investigate the effect of sediment compaction on pore water pressure gradient using a 2D wave flume. The performance of the model has been also evaluated using datasets measured at Hasaki Oceanographical Research Station (HORS), Japan, and data obtained from O.H. Hinsdale Wave Research Laboratory of Oregon State University, USA. The performance of the model was evaluated using the Akaike Information Criteria (AICc). The AICc test results revealed that both Archimedean and elliptical copulas can generate and extrapolate correlated parameters using limited observational data.

Then, numerical simulations have been conducted to estimate different parameters in the ocean and coastal environments from the offshore region to the surf and swash zone as the main part of the research. Therefore, a numerical model was written and performed under the MATLAB environment. The beach profile evolution model consisting of three sub-models was applied to validate the model with field data in different locations. Each module calculates a distinct part of the model as follows: 1) Wave and hydrodynamics; 2) sediment transport, and 3) beach profile update. Therefore, several parameters should be simulated to achieve beach profile changes.

Finally, the model was evaluated by datasets obtained from different coastal areas all around the world. Although sediment transport is a very sophisticated mechanism, it is very helpful to understand various coastal parameters by conducting a morphological project. Until now, most beach profile models are not able to simulate berm formation accurately. The model simulates the evolution of

the berm in connection to erosion and accretion based on different wave conditions at Narrabeen Beach in southeast Australia as well as the southern coasts of the Caspian Sea. Multiple erosion/formation couplets that appeared within the modeled period were simulated successfully. Finally, the model computation time was low, and depending on the simulation duration, the model compiling time was within seconds to minutes.

## **Acknowledgment**

I am very pleased and honored to accomplish my PhD studies at Yokohama National University which is a friendly academic environment. It was also a great experience to conduct coastal engineering PhD studies in Japan as a leading country in developing this research field.

First of all, to my academic supervisor, Prof. Takayuki Suzuki, it was a great honor to conduct my PhD research under your supervision. It is also a great honor to have had the chance to be a member of your research team. You have played a significant role in guiding this research. You provided an enormous amount of continuous support, guidance, and encouraging me to develop our research ideas.

Secondly, I would like to thank my co-advisors, Prof. Yoshiyuki Nakamura, Assoc. Prof. Hiroto Higa, Assis. Prof. Martin Mäll for their insightful comments, questions, and support during this research. I would also like to extend my gratitude to Prof. Daniel Thomas Cox from Oregon State University for using his former student's data and receiving his valuable advice and comment throughout our joint statistical simulation.

Further acknowledgments would be allocated to all the remaining committee members; Prof. Koichi Maekawa, Prof. Hiroshi Katsuchi, Prof. Mamoru Kikumoto for their constructive comments, and questions in order to improve this research.

I owe a lot to the government of Japan for providing me financial support through Monbukagakusho (MEXT) scholarship to study at Yokohama National University which made my dream about studying in PhD level come true. I also really appreciate all YNU staff and estuarian and coastal engineering students for their kind collaboration and support.

Last but not least, to my parents, I cannot be thankful enough for your unwavering support throughout my entire education. You always encouraged me to do my best.

## Table of Contents

1	Introduction .....	1
1.1	Background and motivation.....	1
1.2	Objectives .....	2
1.2.1	Surf zone bed response .....	2
1.2.2	Swash zone beach profile change.....	3
1.3	Research methodology.....	4
1.4	Thesis outline.....	4
2	Literature review.....	5
2.1	Statistical simulation of beach profiles.....	5
2.2	Numerical simulation of beach profiles.....	9
3	Influence of sediment compaction on wave-induced pore pressure gradient	12
3.1	Introduction.....	12
3.2	Experiment setup and description.....	12
3.2.1	Flume setup and instrumentation.....	12
3.2.2	Instrument calibration.....	13
3.2.3	Trial conditions.....	16
3.3	Results and discussion .....	18
3.3.1	Phase averaged pore water pressure .....	18
3.3.2	Pore water pressure.....	18
3.3.3	Vertical pressure gradient.....	20
3.3.4	Sediment concentration .....	23

3.4	Conclusion .....	23
4	Statistical simulation of seabed response in surf zone .....	26
4.1	Introduction.....	26
4.2	Empirical and theoretical cumulative distribution functions.....	26
4.3	Copula theory.....	28
4.4	Dependency construction using copula approach .....	30
4.4.1	Archimedean copulas .....	30
4.4.2	Elliptical copulas .....	31
4.4.2.1	Gaussian copula .....	31
4.4.2.2	Student's t copula.....	32
4.5	Simulation based on constructed copulas .....	33
4.6	Data acquisition .....	34
4.6.1	Field setup and data .....	34
4.6.2	Laboratory instrumentation and data.....	37
4.7	Data analysis .....	40
4.7.1	Dependent field data.....	40
4.7.2	Dependent laboratory data.....	42
4.8	Discussion.....	43
4.8.1	Multivariate analysis for copula simulation .....	43
4.8.2	Distributions and estimations of CDFs.....	45
4.8.3	Fitting data to different copulas and comparison of GOFs ....	48
4.9	Model application .....	56
5	Modeling of berm formation and erosion.....	61
5.1	Introduction.....	61

5.2	Beach locations and data description.....	62
5.2.1	Southern coast of Caspian Sea.....	62
5.2.2	Narrabeen-Collaroy beach.....	64
5.3	Model description .....	67
5.3.1	Berm formation.....	69
5.3.2	Berm erosion.....	70
5.4	Model setup.....	71
5.5	Results.....	72
5.5.1	Caspian Sea.....	73
5.5.2	Narrabeen.....	77
5.5.2.1	Sediment transport calibration .....	78
5.5.2.2	Criteria for distinguishing erosion and accretion.....	78
5.5.2.3	Monthly simulation.....	84
5.5.2.4	Simulation for different periods.....	89
6	Conclusion .....	94
7	Reference .....	98

## List of Tables

Table 3-1 Wave and sediment condition.....	17
Table 4-1 Theoretical Cumulative Distribution Function (TCDF) and corresponding fitting parameters. ....	27
Table 4-2 Archimedean copula governing functions. ....	31
Table 4-3 Summary of wave condition .....	39
Table 4-4 Kendall's $\tau$ correlation coefficient between measured parameters. ....	44
Table 4-5 Probability distribution parameters and GOF results for normalized field and laboratory data. ....	46
Table 4-6 AICc test results for simulations.....	49
Table 4-7 Summary of wave, Shields, Sleath parameters, and sheet flow thickness .....	58
Table 5-1 Classification of Brier Skill Score (BSS) by Van Rijn et al. (2003) .....	72
Table 5-2 Duration of model simulation and wave parameters for selected beach.....	73

## List of Figures

Figure 1-1 Beach Profile changes in nearshore area. ....	3
Figure 3-1 (a): Experimental setup including the location of Wave Gauges (WG), Pressure Transducers (PT), and Conductivity Concentration Meter (CCM). (b): Schematic of the pressure transducer array. ....	13
Figure 3-2 Recorded voltages for calibration procedure of wave gauges. ....	14
Figure 3-3 Recorded voltages for calibration procedure of pressure transducers .....	15
Figure 3-4 Recorded voltages for the calibration procedure of sediment concentration meter .....	16
Figure 3-5 High and low compaction condition samples.....	17
Figure 3-6 Pore pressure measurements from Pressure Transducers (PT). ....	18
Figure 3-7 Comparison between measured pore pressures by each Pressure Transducer (PT) with low and high sediment compactions .....	19
Figure 3-8 a) Definition of time lag. b) Time lag differences between different sediment compactions for each Pressure Transducer (PT).....	20
Figure 3-9 (a) and (b): Comparison of vertical pressure gradient between low and high compaction conditions for the waves with the heights of about 8 cm and 10 cm and the same wave period. (c) and (d): Comparing the effect of wave period using normalized $t/T$ under roughly equivalent wave height conditions for both low and high sediment compaction conditions. ....	22
Figure 3-10 Maximum vertical pressure gradient under (a): wave crest and (b): wave trough.....	22
Figure 3-11 Averaged sediment concentration. ....	23

Figure 4-1 Location of Hasaki Oceanographical Research Station (HORS)	35
Figure 4-2 Instrument arrangement: (a) Pressure transducers and sediment concentration profiler arrangement, (b) the instrument locations from the top view of the deck, and cross-shore beach profile morphology	36
Figure 4-3 Time series of measured parameters at HORS	37
Figure 4-4 Instrumentation and experimental setup	40
Figure 4-5 Scatterplots of pressure gradients (a), accelerations(c), and bottom sediment concentration (e) induced by different water levels ( $\eta$ ) above the still water level. Red dots denote maximum values corresponding to the maximum water level ( $\eta_{max}$ ); (b), (d), and (f) show maximum pressure gradients, accelerations, bottom sediment concentration, respectively. (g) Scatterplot of ( $\partial u/\partial t_{max}$ , $\partial(P/\rho)/\partial x_{max}$ )	42
Figure 4-6 Scatterplots of ( $\partial(P/\rho)/\partial x_{max}$ , <i>Wave height</i> ), ( $\partial u/\partial t_{max}$ , <i>Wave height</i> ), and ( $\partial u/\partial t_{max}$ , $\partial(P/\rho)/\partial x_{max}$ ) represented by (a), (b), and (c), respectively	43
Figure 4-7 Comparison between scatterplots of normalized field and laboratory data	44
Figure 4-8 ECDFs of measured data and TCDFs applicable to normalized field data	47
Figure 4-9 ECDFs of measured data and TCDFs applicable to normalized laboratory data	47
Figure 4-10 Comparison of p-values (A) and TCDFs fitting parameters (B) for field and experimental data	48
Figure 4-11 Scatterplots of joint probability for observed and simulated field data for ( $\eta_{max}$ , $\partial(P/\rho)/\partial x_{max}$ ). Observed and simulated data shown by red and blue dots, respectively	50

Figure 4-12 Scatterplots of observed and simulated field data for  $(\eta_{max}, \partial(P/\rho)/\partial x_{max})$ . Observed and simulated data shown by red and blue dots, respectively. .... 51

Figure 4-13 Scatterplots of joint probability for observed and simulated field data for  $(Hs, max, \partial u/\partial t_{max})$ . The observed and simulated data are shown by the red and blue dots, respectively. .... 51

Figure 4-14 Scatterplots of observed and simulated field data for  $(Hs, max, \partial u/\partial t_{max})$ . The observed and simulated data are shown by the red and blue dots, respectively. .... 52

Figure 4-15 Scatterplots of joint probability for observed and simulated field data for  $(\partial(P/\rho)/\partial x_{max}, \partial u/\partial t_{max})$ . The observed and simulated data are shown by the red and blue dots, respectively. .... 52

Figure 4-16 Scatterplots of observed and simulated field data for  $(\partial(P/\rho)/\partial x_{max}, \partial u/\partial t_{max})$ . The observed and simulated data are shown by the red and blue dots, respectively. .... 53

Figure 4-17 Scatterplots of joint probability for observed and simulated laboratory data for  $(Hs, max, \partial(P/\rho)/\partial x_{max})$ . The observed and simulated data are shown by the red and blue dots, respectively. .... 53

Figure 4-18 Scatterplots of observed and simulated laboratory data for  $(Hs, max, \partial(P/\rho)/\partial x_{max})$ . The observed and simulated data are shown by the red and blue dots, respectively. .... 54

Figure 4-19 Scatterplots of joint probability for observed and simulated laboratory data for  $(Hs, max, \partial u/\partial t_{max})$ . The observed and simulated data are shown by the red and blue dots, respectively. .... 54

Figure 4-20 Scatterplots of observed and simulated laboratory data for  $(Hs, max, \partial u/\partial t_{max})$ . The observed and simulated data are shown by the red and blue dots, respectively. .... 55

Figure 4-21 Scatterplots of joint probability for observed and simulated laboratory data for $(\partial(P/\rho)/\partial x_{max}, \partial u/\partial t_{max})$ . The observed and simulated data are shown by the red and blue dots, respectively. ....	55
Figure 4-22 Scatterplots of observed and simulated laboratory data for $(\partial(P/\rho)/\partial x_{max}, \partial u/\partial t_{max})$ . The observed and simulated data are shown by the red and blue dots, respectively. ....	56
Figure 4-23 Scatterplots of observed and simulated laboratory data for Sleath number and sheet flow thickness. Observed and simulated data shown by red and blue dots, respectively. ....	60
Figure 5-1 Locations of measured (field) beach profiles in the Caspian Sea (Iran). ....	64
Figure 5-2 Wave condition for each coastal region of Caspian Sea; (a) significant wave height and (b) mean wave period. ....	64
Figure 5-3 Narrabeen and cross-shore beach profile locations .....	66
Figure 5-4 SVI values for Narrabeen .....	66
Figure 5-5 Schematic diagram of berm formation and erosion .....	69
Figure 5-6 Sediment transport rate by Suzuki and Mochizuki (2014). ....	71
Figure 5-7 Right panels: Evolution of berm formation in Astara (a), Dastak (b), Larim (c), and Miankaleh (d) for measured (blue dashed line) and simulated beach profiles (red asterisk line). Green lines represent initial beach profiles. Left panels: Hindcast wave rose. ....	76
Figure 5-8 Right panels: Evolution of berm erosion in Namakabrud (a) and Mahmudabad (b) for measured (blue dashed line) and simulated beach profiles (red asterisk line). Green lines represent initial beach profiles. Left panels: Hindcast wave rose. ....	77
Figure 5-9 Calculated wave criterion values based on Sunamura (1980). 82	
Figure 5-10 Calculated wave criterion values based on Larson and Kraus (1989). ....	83

Figure 5-11 Sediment erosion and accretion separation values defined in model. ....	85
Figure 5-12 Wave height condition for 2010. ....	85
Figure 5-13 Monthly beach profile simulation results for 2010. ....	86
Figure 5-14 Wave height condition for 2011. ....	87
Figure 5-15 Monthly beach profile simulation results for 2011. ....	87
Figure 5-16 Wave height condition for 2012. ....	88
Figure 5-17 Monthly beach profile simulation results for 2012. ....	88
Figure 5-18 Monthly beach profile simulation results for 2013. ....	89
Figure 5-19 Beach profile simulation for different durations in 2010. ....	90
Figure 5-20 Beach profile simulation for different durations in 2011. ....	91
Figure 5-21 Beach profile simulation for different durations in 2012. ....	92
Figure 5-22 Beach profile simulation for different durations in 2013. ....	93

# **1 Introduction**

## **1.1 Background and motivation**

As waves propagate from the offshore towards onshore, the sediment beneath the waves is under the influence of wave characteristics, and the waves inevitably become steeper due to beach morphology. Therefore, coastal bed profiles and water waves have a mutual interaction, and there is a close relationship between the shape of bed profiles and waves. Coastal regions experience different waves and tidal levels continuously; therefore, beach face responds to fluid motion. According to wave characteristics and tidal conditions, sediment moves either landward or seaward.

Surf zone sandbars and swash zone berms are ephemeral nearshore bathymetric features that play a fundamental role in beach profile morphology (Ribas et al., 2012; Tabasi et al., 2017; Tabasi et al., 2018; Bryan et al., 2019). Field sites have been established along many coastlines to measure coastal hydrodynamic and morphodynamic characteristics, depending on the available budget and data necessity. Therefore, instruments for recording data may be deployed for a short or long duration. In some critical locations, for gathering data over seasons or years, instruments are installed permanently with the requirement for regular maintenance. However, owing to time and financial limitations, long-term data recording is not practical. Moreover, the gathered datasets may include missing data either due to the maintenance procedure of instruments, intentional pausing of recording to maintain the safety of instruments during coastal disasters or extreme events, and failure of instruments. Because of the abovementioned issues and coastal regions where no captured data are available, it is reasonable to simulate data using different methods. The simulated data should be modified and validated using the data recorded from a nearby location.

## 1.2 Objectives

### 1.2.1 Surf zone bed response

Surf zone sandbars enhance depth-induced wave breaking and subsequently initiate complex fluid motions generated by breaking waves in the surf zone. As a result of these fluid motions and the resulting sediment suspension and transport, the morphology of the nearshore can change rapidly. Because the morphological response of surf zone sandbars is governed by nearshore hydrodynamics, the prediction of surf zone sandbar morphological evolution is associated with the understanding of nearshore waves and current characteristics.

Generating data using different methods is important in turbulent environments, such as the surf zone, where not only do hydrodynamic parameters change abruptly, but also morphological components such as the sandbar shape change rapidly. Therefore, an improved prediction of hydrodynamic and morphodynamic parameters is closely associated with the understanding of several interconnected mechanisms, such as acceleration, velocity skewness, and pressure gradient, to obtain accurate surf zone sand bar shapes. Although several morphodynamic models have been proposed (e.g., Roelvink et al., 2010; Kuriyama, 2012; Tabasi et al., 2020), a comprehensive model that includes all interconnected mechanisms applicable to various coastal areas has not yet been developed. Therefore, the beach profile shape according to the hydrodynamic condition is changing, continuously (Figure 1-1).

One of the objectives in this study is to provide a computationally efficient approach to model the joint probability and distribution for the height of the wave crest above the still-water level ( $\eta_{max}$ ), the maximum horizontal pressure gradient ( $\partial(P/\rho)/\partial x_{max}$ ) induced by  $\eta_{max}$ , and the maximum local horizontal acceleration ( $\partial u/\partial t_{max}$ ) induced by  $\eta_{max}$  within the surf zone of a natural coastal zone and a large-scale wave flume using a fully statistical approach.

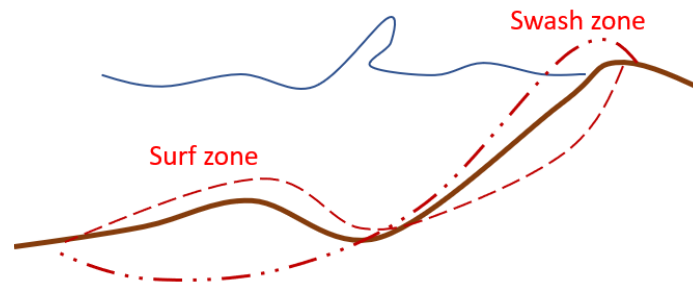


*Figure 1-1 Beach Profile changes in nearshore area.*

### **1.2.2 Swash zone beach profile change**

Berm is a well-known beach profile feature that changes based on the wave conditions. Berms typically form during mild wave conditions and erode during storms. When the fluid motion is low, the sand grains move as a bed-load sediment transport. If the fluid motion increases, then a saturated layer of sediment starts moving as sheet-flow sediment transport. Once the fluid motion becomes sufficiently high, the hydrodynamic forces lift the sand particles into the water column, and suspended sediment transport will be dominant.

The berm encounters uprush and backwash. Consequently, intermittent flows vary rapidly in this wet/dry zone and high gradients and values of sediment concentration and transport are yielded. Because of the high gradients of the flow velocities, all mechanisms of sediment transport should be considered and expected to contribute to berm formation and erosion analysis. In other words, all the mechanisms may affect berm formation and erosion. However, because of the complex mechanisms between water and sediment layers, it is difficult to model and calculate all the relationships.

### **1.3 Research methodology**

In order to investigate bed response from the surf zone to swash zone several objectives described in the previous section. To achieve these objectives the following methodology were adopted.

- Objective 1: The effect of sediment compaction on wave-induced pore water pressure for the offshore sandbars
  - Methodology: Small-scale laboratory investigation
- Objective 2: Simulation of wave-induced pore water pressure, local acceleration within the surf zone
  - Methodology: Statistical simulation (Copula approach)
- Objective 3: Beach profile change in the swash zone
  - Methodology: Numerical simulation

### **1.4 Thesis outline**

This thesis consists of experimental, statistical, and numerical simulations carried for the objectives mentioned in the previous section. Large-scale laboratory experiment and field datasets were also used to validate the performance of simulations. In the following chapters, first, the literature reviews of previous works consist of field, laboratory experiments, and simulations are presented in chapter 2. Then in chapter 3, the small-scale laboratory experiment to investigate the influence of sediment compaction on wave-induced pore pressure gradient are described. In chapter 4, statistical simulation using copula approach as well as validation of simulation using large-scale laboratory and field datasets are discussed. Chapter 5 presents numerical modeling of berm formation and erosion at the southern coasts of the Caspian Sea and Narrabeen-Collaroy beach in Iran and Australia, respectively. Finally, the discussion is presented in chapter 6.

## **2 Literature review**

### **2.1 Statistical simulation of beach profiles**

Sediment transport mechanisms have been investigated through various laboratory experiments (Wang et al., 2002; Berard et al., 2017), field observations (Aagaard et al., 2002; Mariño-Tapia et al., 2007), and sediment transport models (Ruggiero et al., 2009; Tabasi et al., 2020). Regarding sediment transport, not only wave action but also the characteristics of the seabed sediment layer will affect its motion. The wave-induced pressure gradient within sediment layers significantly influences various coastal mechanisms (Suzuki et al., 2009) and is one of the key parameters for investigating sediment transport. Researchers are attempting to include and evaluate several interconnected parameters in morphodynamic models. Suzuki et al. (2009) and Anderson et al. (2017) have shown that pressure gradients within sediment layers driven by waves and currents resulted in surf zone sandbar migrations. Subsequently, they investigated the pore water pressure gradient and current acceleration based on the wave height.

Various methods can be used to simulate water level, pressure gradients and accelerations. Fundamentally, the flow properties can be determined by solving the Navier-Stokes equations. However, due to turbulence terms in these equations, the exact solution of these equations is still incomplete except for very small control volumes. Nevertheless, these equations can be simplified by neglecting the term describing viscous motions of the flow to yield the Euler equations. Using intensive numerical models, pressure gradients and accelerations can be obtained using Euler's inviscid momentum equations for a short duration. For solving these equations, the volume of fluid should be discretized or divided into several cells which is known as mesh. Open-source software (e.g., OpenFOAM, DualSPHysics) is readily available to obtain water level, pressure gradients, and accelerations via momentum equations (Brown et al., 2016; Lowe et al., 2019).

However, depending on the required accuracy and the complexity of the flow, a more sophisticated discretization method with a high mesh resolution is required. Thus, the implementation of the numerical model will be more complicated. Because of the complicated model setup and code-compiling processes, the model computation time is often extremely long. Nevertheless, numerical simulations can be very useful approaches to predict and realize a wide variety of water environment processes.

Linear wave theory describes the propagation of waves or fluid surface changes assuming that the fluid is inviscid, incompressible, irrotational, and the surface of the fluid has a sinusoidal shape. However, the linear wave theory is valid for uniform small-amplitude waves and the linear wave model should be modified by including the effects of second-order nonlinearities such as Stokes drift, wave crest conservation, and mean mass conservation. Among the second-order wave approaches for solving the nonlinear waves, Stokes's approach is very well-known. This approach proposes a solution for applying the boundary condition at the free surface position expanding the potential flow quantities in a Taylor series. Depending on the required accuracy, higher-order nonlinear wave approaches can be estimated accordingly. Valuable reviews about different wave theories and proposed models for the simulation of the water surface can be found in (Forristall, 2000; Tayfun and Fedele, 2007; Myrhaug et al., 2015).

Statistical methods are useful for simulating wave and wave-induced parameters such as wave heights, pressure gradients, and accelerations. For example, wave heights can be simulated using statistical-based wave spectra such as Neuman, JONSWAP, ITTC, and P-M spectrums. These spectra have been performed and evaluated in several coastal engineering studies such as Dawson et al. (1993); Ryabkova et al. (2019); Edwards et al. (2021). Similarly, Monte Carlo is a reliable simulation method (Bang Huseby et al., 2013; Clarindo et al., 2021) and can be used to account for the joint probability of correlated coastal parameters.

Statistical multivariate regression models have been used to represent the relationships between dependent different parameters (Condon and Sheng, 2012). Although regression modeling is a very common method and almost all statistical packages are equipped with regression tools, the reliability of regression models generally decreases as the number of parameters increases.

Because of the complexities of coastal phenomena, the interdependency of coastal parameters should be considered in the calculations. In statistics, if the magnitude of one variable affects the magnitude of other variables, then the particular variable can be considered dependent. The dependency between two variables can be described using correlation coefficients. As mentioned above, owing to the importance of the dependency between variables, several methods have been proposed to model the bivariate joint probability of two variables. Plackett (1965) proposed a method for constructing a one-parameter bivariate distribution based on marginal functions. Vrijling and Bruinsma (1980) applied marginal distributions to model the significant wave height ( $H_s$ ) and wave steepness ( $S_p$ ). In this model, the peak period ( $T_p$ ) is described as a function of ( $H_s, S_p$ ). Bitner–Gregersen and Haver (1989) developed a conditional modeling approach to model the joint distribution of  $H_s$  and  $T_p$  using regression curves. Zachary et al. (1998) presented a non-parametric approach to model meta-ocean parameters. Repko et al. (2004) described and compared five approaches to model the dependency between  $H_s$  and  $T_p$ . Sellés Valls (2019) summarized that five bivariate models presented limitations when variables other than  $H_s$  and  $T_p$  were used.

The copula approach, originally proposed by Sklar (1959), allows for the marginal distribution of dependent variables to be estimated separately based on a dependent structure, and numerous studies have been conducted to investigate the applicability to a range of problems. Nelsen (2006) described the construction of different copulas and their properties, whereas Schmidt (2006) provided a more

concise guide into the theory of the copula approach. In coastal science and engineering, by De Waal and Van Gelder (2005) proposed the Burr–Pareto–logistic copula to model extreme significant wave heights and wave periods during severe storm events. De Michele et al. (2007) established a four-dimensional model for the analysis of significant wave height, storm duration, inter-arrival time, and wave direction. Salvadori et al. (2011) proposed multi-parameter multivariate extreme value (MEV) copulas to assess return periods and design qualities. Wahl et al. (2011) applied the Gumbel–Hougaard copula to analyze storm surge parameters. Subsequently, Wahl et al. (2012) extended the proposed bivariate statistical model to investigate the extreme significant wave height and peak sea level. Corbella and Stretch (2013) applied Archimedean and MEV copulas to simulate storm parameters such as peak wave period, storm duration, and inter-arrival time.

More recently, Li et al. (2014a) estimated coastal dune erosion along the Dutch coast via a statistical simulation of storm events developed by Li et al. (2014b), who employed a Gaussian copula to simulate the dependency relation of  $(H_{s,max}, h, D, T_p)$ , where  $H_{s,max}$  is the maximum significant wave height during storms;  $h$  is the water dept,  $D$  is the storm duration;  $T_p$  is the peak wave period. Salvadori et al. (2016) presented a multivariate copula-based framework for performing multivariate design during disasters and providing failure probabilities. Jane et al. (2016) developed a copula-based approach focusing on the Gaussian and Student’s t copulas to predict  $H_s$  and the wave direction ( $\theta$ ) at different locations along the southern coast of England. Lin et al. (2020) proposed a copula mixture model to provide a long-term joint distribution for  $H_s$  and a mean zero-crossing wave period ( $T_z$ ).

## 2.2 Numerical simulation of beach profiles

For several reasons such as beach protection, nourishment, and the design of the coastal constructions, nearshore morphodynamic behavior is very important. However, movement in the nearshore zone or in the inner surf and swash zone due to very turbulent flow motion is the most uncertain sediment relevance process in the coastal environments. Sediment transport in the offshore area compared to the nearshore area can be fairly well understood and predicted owing to the less turbulent hydrodynamic condition. Moreover, in the nearshore area, sands are submerged by uprush and backwash frequently. Water flows in the uprush and backwash have not the same behavior. Since the main force for flowing the backwash is the gravity, the duration of backwash should be longer than the uprush (Hughes et al. 1997). Therefore, the exchange of sands between the emerged and submerged beach should be expected.

Despite the importance of nearshore zone, sediment transport rate and beach profile evolution investigated in different studies are not accurate in most cases specially in the swash zone. It can be because of unsteady flows, and hence high turbulence levels, large sediment transport rate, and rapid morphological change (Puelo et al 2000). Alsina et al. (2009) also indicated that many of the uncertainty in the sediment transport estimation are due to the unsteady flows in the nearshore area. Additionally, the beach face morphological conditions affect the nearshore hydrodynamic. For example, on the mild slope or dissipative beaches with low Iribarren numbers, the nearshore hydrodynamic condition is less turbulent than the steep slope beaches with high Iribarren numbers.

The number of studies investigated nearshore hydrodynamics is relatively larger than studies about morphodynamic mechanisms in the nearshore area (e.g., Petti and Longo, 2001; longgo et al. 2002). In other words, morphodynamic models in dealing with the nearshore have had very slow development. However, Butt and Russell (2000), Masselink ad Puleo (2006), and Brocchini and Baldock

(2008) represented valuable reviews about the nearshore hydrodynamic modeling in connection with the nearshore morphodynamic processes.

According to the beach shape and hydrodynamic conditions, sediments move in both longshore and cross-shore directions. The amount sediment transport in each direction can also be different based on the hydrodynamic conditions. Similarly, the amount of sediment erosion or accretion can be different based on the hydrodynamic conditions. Morphodynamic models for the estimation of sediment transport and beach profile simulation can be classified into descriptive, equilibrium profile, empirical, statistical, process-based, and statistical process-based models. Additionally, based on the spatial scale of the application morphodynamic models are categorized into coastline, beach profile, and area modeling. In plain language, coastline models predict the shoreline changes. Beach profile models simulate cross-shore beach profile evolution while the area models predict beach profile changes in both cross-shore and longshore directions with different resolutions.

Descriptive models such as Sonu (1973), Short (1978), Dean (1973) mainly introduce important coastal parameter to represent erosive and accretive sequences, relationship between the wave breaking point and bar migration. Equilibrium beach profile models described in several research works such as Brunn (1962), Swart (1975), Van de Graaff (1977), Dean (1973), Vellinga (1982) indicate that although profile might change to different shapes based the different coastal events, the final beach profile has a tendency to the equilibrium shape. Empirical models such as Larson and Kraus (1989), Kriebel and Dean (1993), Sallenger (2000), and Larson et al. (2004) estimate the beach profile response to the different coastal events based empirical equations derived from the previous observations. Therefore, empirical models need to be optimized or calibrated for each case study. Statistical models such as Armenio et al. (2019) mostly analyze the effect of long-term morphodynamic data to predict the potential changes due to long-term

parameters such as climate change. Process-based models (e.g., Southgate and Narin 1993, Kobayashi et al. 2008, Roelvink et al. 2010, Tabasi et al, 2017, 2018) which are commonly used for the morphodynamic modeling attempt to simulate morphodynamic behavior of the coastal areas in association with the physics of the system. However, a wide range of empirical equations especially in the sediment transport modules are included in the process-based models. Statistical-process based models such as Pender and Karunarathna (2019) are aiming to predict medium to long-term morphological changes.

Due to the importance of beach erosion in the consequence of storms as a coastal hazard, morphological models have focused more on the beach profile erosion than beach profile recovery. However, a reasonable prediction of beach profile recovery after an erosional event is essential for various purposes such as beach nourishment estimation or shoreline position prediction. In this study a process-based morphodynamic model containing empirical formulation is proposed to predict berm morphological changes at Narrabeen beach. In this paper, field study and achieved data are explained first. Then the performance of the model, optimization, and calibration procedure are described and evaluated.

### **3 Influence of sediment compaction on wave-induced pore pressure gradient**

#### **3.1 Introduction**

Sediment transport mechanisms have been investigated through various laboratory experiments, field observations, and sediment transport models. Regarding sediment transport, not only wave action but also the characteristics of the seabed sediment layer will affect its motion. The wave-induced vertical pressure gradient within sediment layers significantly influences various coastal mechanisms and is one of the key parameters for investigating sediment transport. Furthermore, vertical pressure gradient relates to the level of sediment compaction or porosity, and some models include the effect of porosity in numerical beach morphology models.

The hydrodynamic characteristics within the sediment layers rely on the wave and current conditions and the sediment conditions such as median grain size ( $D_{50}$ ) and the sediment compaction. Most researchers are devoted to investigating the effect of wave characteristics such as steepness on the vertical pressure gradient within sediment layers. However, only few researches are available that focus on the effect of sediment compaction on vertical pressure gradient within sediment layers. Therefore, in the present study, the effect of sediment compaction on vertical pressure gradient using a small-scale laboratory experiment was analyzed to emphasize the influence of this parameter on different coastal mechanisms.

#### **3.2 Experiment setup and description**

##### **3.2.1 Flume setup and instrumentation**

The experiment was conducted in a small-scale wave flume at Yokohama National University that is 17 m long, 0.6 m wide, and 0.6 m deep with glass

sidewalls (Figure. 3-1a). A fixed wooden sandpit was constructed and installed in the flume as an artificial sandbar (1.5 m long, 0.6 m wide, and 0.15 m deep). An array of pore pressure transducers (BPR-A-50KPS, Kyowa) composed of four transducers with 4 cm center to center spacing in a vertical row was installed in the center of the sandpit with a 10 cm distance from the flume sidewall (Figure. 3-1b).

The sandpit was filled with well-sorted sand with a median grain size of 0.08 mm. The cables of each transducer were fixed to the flume side wall and buried in the sediment for minimal flow interference. The heads of pressure transducers were installed after ensuring complete saturation. The frequency of pressure recording was set at 100 Hz without affecting calibration. For all trials, five capacitance wave gauges were mounted on the flume from the offshore side to the onshore edge of the sandpit to record water surface elevations along the flume. A sediment concentration meter was installed 1 cm above the bed at the same cross-shore location of the array of pressure transducers. For each trial, regular waves were generated by the piston-type wave generator.

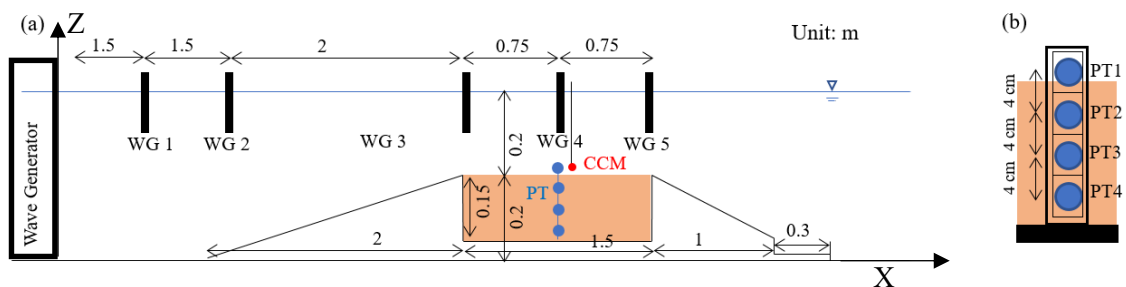


Figure 3-1 (a): Experimental setup including the location of Wave Gauges (WG), Pressure Transducers (PT), and Conductivity Concentration Meter (CCM). (b): Schematic of the pressure transducer array.

### 3.2.2 Instrument calibration

Before, conducting trials wave gauges, pressure transducers and concentration meter were calibrated. In addition, their sensitivities were check by reconducting calibration procedure for several times. The wave height was

measured using wave gauges manufactured by Keisokugiken Co., Ltd. and recorded with a digital recorder midi LOGGER GL900 manufactured by GRAPHTEAC. The wave gauges measure changes in wave height and water depth using changes in electrical voltage and convert them to a height scale for achieving changes in wave height and water depth. Since each wave gauge has individual characteristic values, it is necessary to install it on the lifting device and calibrate it. The calibration results of five wave height meters are shown in Figure 3-2. Using the equation of the regression line obtained by this, the wave height data of the length unit is calculated.

Regarding the installation of the wave height meter, CH1 was installed at a position 1.5m away from the wave generator, and CH2 was installed at the tip of the slope, aiming to measure the wave height before being affected by shallow water deformation. CH3 was installed at the front end of the moving bed area, CH4 was installed at the center, and CH5 was installed at the rear end. In addition, especially for CH4, we also aim to measure the wave height at the pressure measurement point.

$$\begin{cases} CH1: y = 3.8749x - 0.0303 \\ CH2: y = 4.389x + 0.0134 \\ CH3: y = 4.475x + 0.0757 \\ CH4: y = 3.7213x + 0.0386 \\ CH5: y = 3.9065x + 0.0315 \end{cases} \quad (1)$$

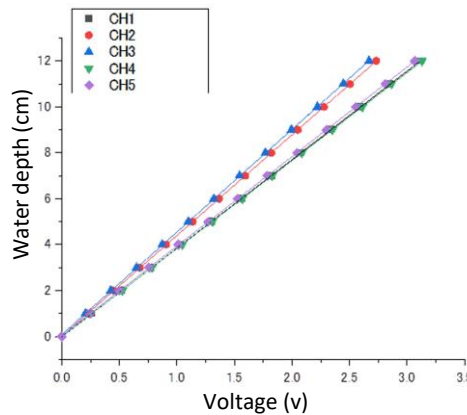


Figure 3-2 Recorded voltages for calibration procedure of wave gauges

Each pressure transducer was submerged into the water at different levels. The recorded voltage values of pressure transducers corresponding to different relative water depth were assumed as hydrostatic water pressure. The recorded voltages and their corresponding actual hydrostatic water pressures are represented in Figure 3-3. The calibration procedure was conducted using the linear regression method to obtain the relationship between recorded voltages and hydrostatic water pressures. Therefore, pressure can be related to voltage measured by each pressure transducer as follows:

$$\begin{cases} P_1 = 1.202V_1 - 0.8772 \\ P_2 = 1.1735V_2 - 0.598 \\ P_3 = 2.1569V_3 - 0.4518 \\ P_4 = 2.0231V_4 - 0.4332 \end{cases} \quad (2)$$

where P and V are pressure and voltage, respectively. The subscripts denote the location of transducers.

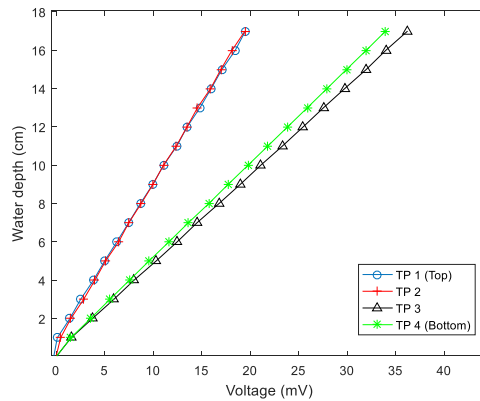


Figure 3-3 Recorded voltages for calibration procedure of pressure transducers

For calibrating concentration meter, 20 gr of sediment which was used to fill the sandpit was added to 20 l water of a bucket for several times. To achieve a homogenous mixture an electrical mixer was used during the voltage recording procedure (Figure 3-4). A similar strategy to that used in pressure transducer calibration procedure was employed. The calibration results for pressure transducers and concentration meter indicated that the sensors had a good linear

correlation with the actual hydrostatic water pressure and sediment concentration. The concentration can be estimated by:

$$C = 0.0064V^2 + .01888V - 0.0484 \quad (3)$$

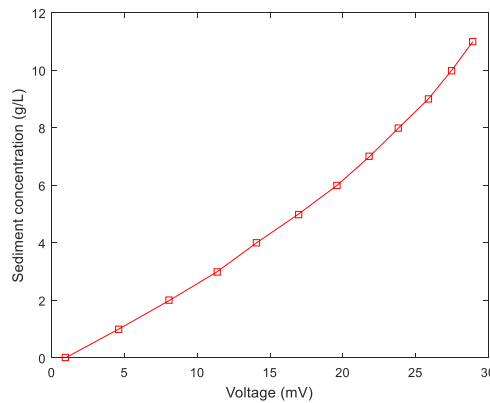


Figure 3-4 Recorded voltages for the calibration procedure of sediment concentration meter

### 3.2.3 Trial conditions

In total, 16 trials were conducted. For each trial, 10 waves after five minutes from the wave generation were used for the analysis. The sediments filled in the sandpit were classified into low and high compaction conditions. In this experiment, first, the sediment layers were compacted to obtain a high compaction condition. Then, by twisting an L-shape bar in the sediment (sandpit) the low compaction condition was achieved (Figure 3-5). To evaluate the level of sediment compaction, the shear strength of sediment was measured by a torque meter at different sediment layers (top, middle, and bottom).

The measurement was conducted at three different cross-shore locations with about 20 cm distance from each flume sidewall to arrange the dataset. In other words, the sediment compaction was investigated at six locations and three different elevations within the sediment. Thus, the shear strength of the sediment was, in total, measured at eighteen points to evaluate the level of sediment

compaction or porosity. All hydrodynamic and sediment compaction conditions are summarized in Table 3-1.



Figure 3-5 High and low compaction condition samples.

Table 3-1 Wave and sediment condition.

Trial No.	Sediment Condition	$\tau_{top}$ (kN/m <sup>2</sup> )	$\tau_{middle}$ (kN/m <sup>2</sup> )	$\tau_{bottom}$ (kN/m <sup>2</sup> )	$H_{(WG1)}$ (cm)	$T$ (s)	$H_{(WG4)}$ (cm)	$L_{(WG4)}$ (m)	$H_{(WG4)}/L_{(WG4)}$
1	High compaction	5.8	19.5	41.5	7.1	1.2	7.9	1.1	0.075
2		6.9	24.7	49.2	7.0	1.4	7.7	1.2	0.063
3		5.0	23.4	48.4	6.8	1.6	8.4	1.5	0.057
4		5.0	22.5	39.0	7.5	2.0	9.1	1.9	0.047
5		5.4	21.2	45.1	9.4	1.0	9.7	0.9	0.104
6		4.7	23.6	44.8	8.7	1.2	10.3	1.8	0.087
7		5.7	19.8	49.7	8.6	1.4	10.0	1.4	0.072
8		5.4	20.3	39.3	8.5	1.6	10.9	1.6	0.066
9	Low compaction	7.3	11.9	32.4	6.7	1.2	7.8	1.0	0.075
10		5.0	7.6	27.8	6.6	1.4	7.6	1.2	0.063
11		4.0	6.5	25.0	7.1	1.6	8.3	1.4	0.057
12		5.2	8.6	28.3	7.3	2.0	9.1	1.9	0.048
13		5.3	9.6	24.5	8.8	1.0	9.7	0.9	0.104
14		3.9	6.2	25.0	8.9	1.2	10.5	1.2	0.088
15		4.6	7.0	27.2	8.8	1.4	10.2	1.4	0.073
16		4.5	8.3	25.8	8.3	1.6	11.1	1.7	0.066

### 3.3 Results and discussion

#### 3.3.1 Phase averaged pore water pressure

The pore water pressure was measured by the pressure transducers. First, the zero-up crossing method was used to select and identify wave-induced hydrodynamic parameters. Then, for visual analysis and better comparison, the hydrodynamic parameters were adjusted to  $t=0$ . Figure 3-6 shows the phase averaged pore water pressure of trial 1, and time lags between the maximum and minimum pressures were found. As the depth of sediment increased, the lag showed larger values. Since most of the studies are devoted to investigating the vertical pressure gradient on the interface of the water and sediment, this phenomenon has not been included in many studies regarding the estimation of vertical pressure gradients.

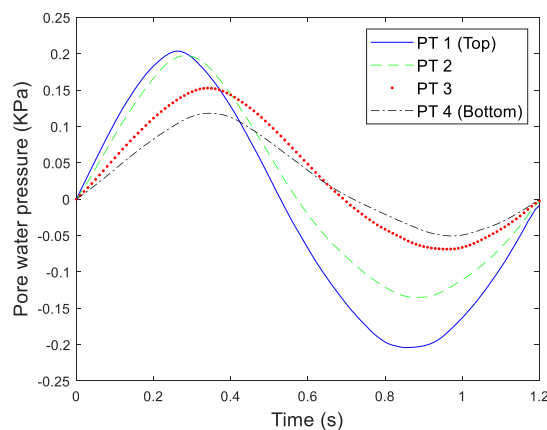


Figure 3-6 Pore pressure measurements from Pressure Transducers (PT).

#### 3.3.2 Pore water pressure

Figure 3-7 represents the pore water pressure measured by each pressure transducers within the sediment layers as well as a comparison between low and high sediment compaction conditions for trials with the wave height of 8 cm (trials 1 to 4 and trials 9 to 12). It should be noted that downward-directed pore water pressure within the sediment layers is owing to the increase of the water column

beneath the wave crest. Conversely, the pore water pressure should be upward-directed beneath the wave trough. Because pressure transducer 1 was just located above the bed, the sediment condition did not affect the measured pressure. Therefore, the measured data of pressure transducer 1 showed nearly the same results for high and low compaction conditions and the influence of different sediment conditions were not observed.

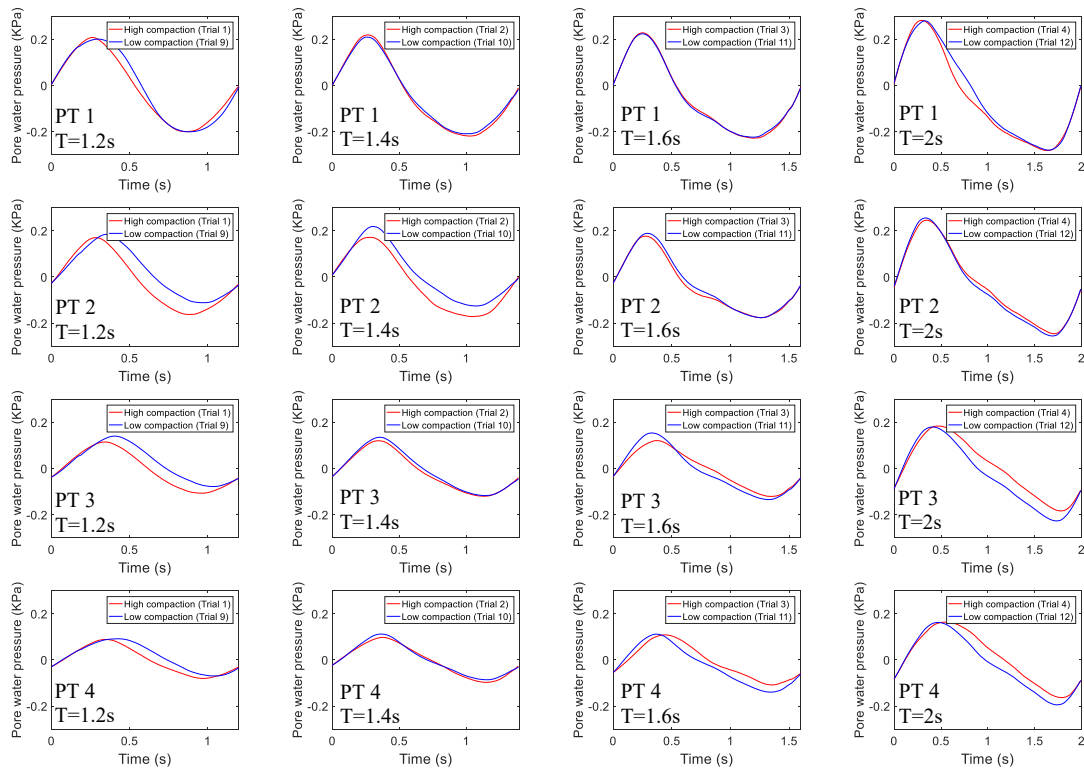


Figure 3-7 Comparison between measured pore pressures by each Pressure Transducer (PT) with low and high sediment compactions

Figure 3-8 shows the time lag differences between measured pore water pressures of high and low sediment compactions, which were calculated for each pressure transducer. The moment that the pore water pressure direction changed, i.e., the moment that is corresponding to  $p=0$  was selected for calculating the time lag difference as follows:

$$\text{Time lag} = t(P_0(L)) - t(P_0(H)) \quad (4)$$

where  $t(P_0(L))$  and  $t(P_0(H))$  are the time corresponding to  $p = 0$  for low and high sediment compaction, respectively. The red arrow in Figure 3-8 shows the definition of time lag.

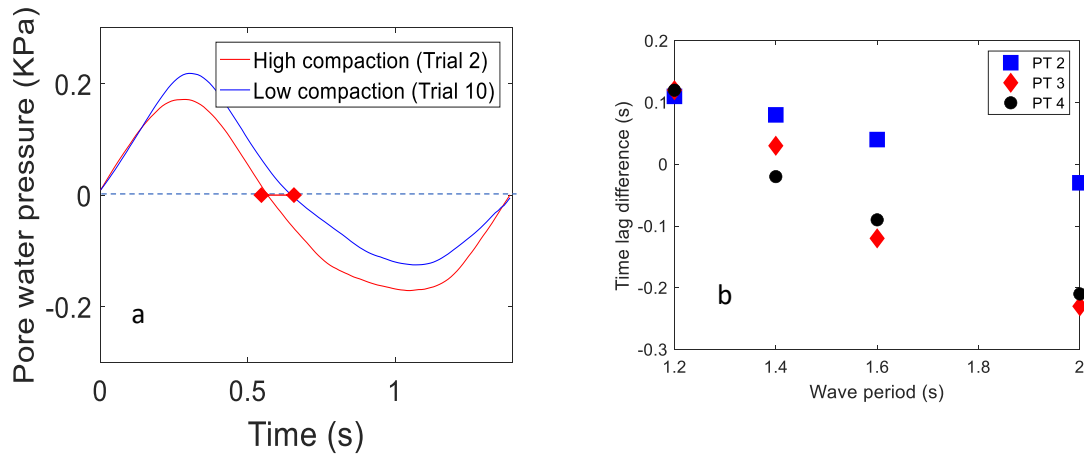


Figure 3-8 a) Definition of time lag. b) Time lag differences between different sediment compactions for each Pressure Transducer (PT).

It can be concluded that for each sediment layer, by increasing the wave periods, the time lag differences were decreased. On the other hand, for waves with shorter periods, the time lag differences had quite similar values. Conversely, the time lag differences for trials with longer periods had a wide range of values.

### 3.3.3 Vertical pressure gradient

Vertical pressure gradient was estimated using third-order finite differencing formulas, which has been used in several studies. The vertical pore water pressure gradient was estimated by

$$\frac{\partial p}{\partial z} = \frac{p_{T1} - 27p_{T2} + 27p_{T3} + p_{T4}}{6\Delta z} \quad (5)$$

where  $\Delta z$  is the distance between transducers, i.e., 4 cm. Negative values for vertical pressure gradient indicate a downward direction.

Figures. 3-9a and b show a comparison between vertical pressure gradients for trials with high and low sediment compaction conditions for different wave periods, i.e., trials 1 and 9, and trials 2 and 10, respectively. It is evident that in all trials the magnitude of vertical pressure gradients for high sediment compaction conditions was larger than corresponding trials with low sediment compaction conditions.

Figures 3-9c and d show a comparison between the vertical pressure gradients of waves with almost equivalent wave heights to assess the effect of wave periods using normalized  $t/T$ . It can be concluded that regardless of sediment compaction level, waves with longer periods induced higher pore pressure gradients within the sediment layers.

However, the range of sediment compactions under high compaction conditions were 4.7 to 6.9  $kN/m^2$ , 19.5 to 24.7  $kN/m^2$ , and 39.0 to 49.2  $kN/m^2$  for the top, middle, and bottom sediment layers, respectively. Similarly, the range of sediment compactions under low sediment compaction conditions were varied between 3.9 and 7.3  $kN/m^2$ , 7 and 11.9  $kN/m^2$ , and 24.5 and 32.4  $kN/m^2$  for the top, middle, and bottom sediment layers, respectively. Thus, the average of peak vertical pressure gradients across all high compaction sediment trials was 1.4 times larger than low compaction trials.

Moreover, the maximum magnitude of vertical pressure gradients within sediment layers were analyzed. Figure 3-10 shows the maximum magnitude of pressure gradients under wave crest as well as wave trough compared with the wave steepness ( $H/L$ ). The results emphasis that the magnitudes of maximum vertical pressure gradients under wave crest and wave trough were larger in trials with high sediment compaction conditions. Decreasing and increasing trends for maximum pressure gradients by increasing the wave steepness can be observed in Figure 3-10a and b, respectively. On the other hand, it is hard to find a certain relationship between the wave steepness and the differences between the

maximum vertical pressure gradients under low and high sediment compaction conditions.

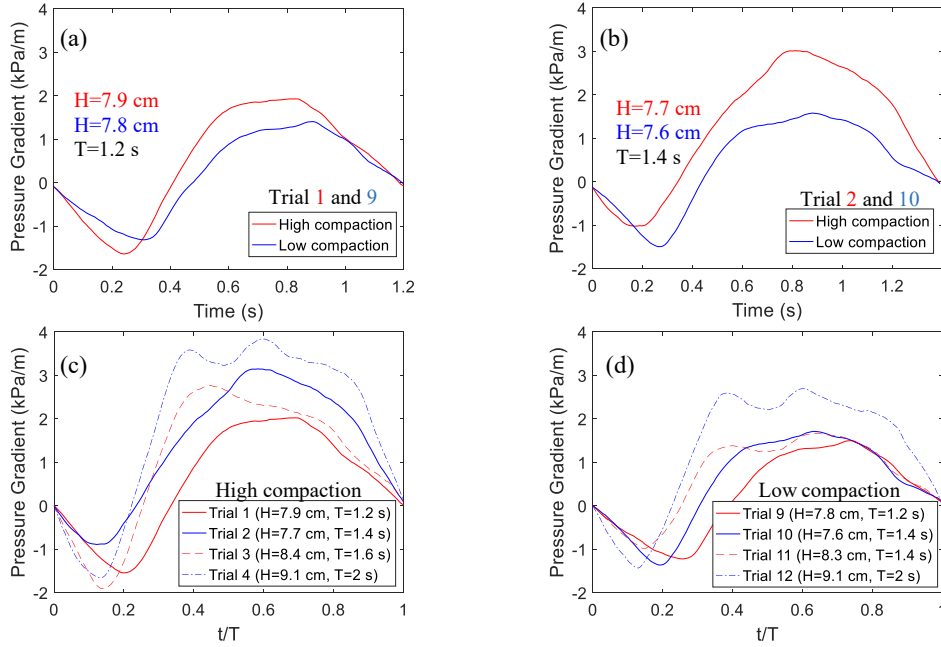


Figure 3-9 (a) and (b): Comparison of vertical pressure gradient between low and high compaction conditions for the waves with the heights of about 8 cm and 10 cm and the same wave period. (c) and (d): Comparing the effect of wave period using normalized  $t/T$  under roughly equivalent wave height conditions for both low and high sediment compaction conditions.

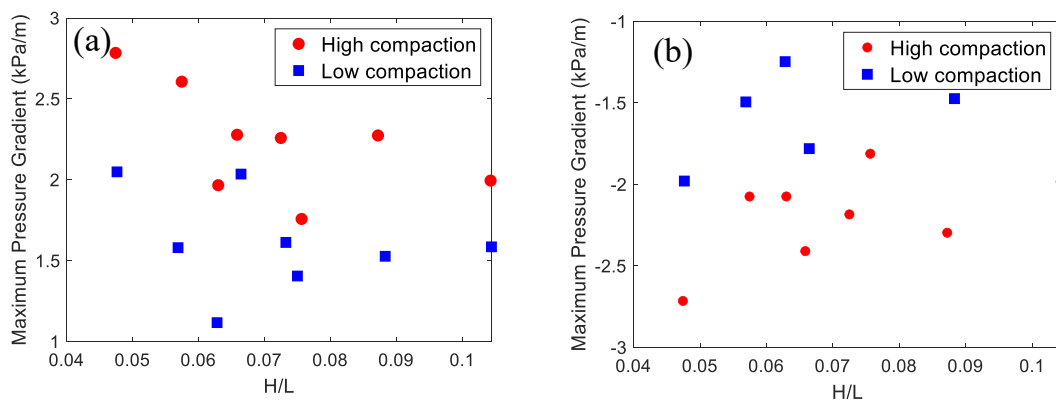


Figure 3-10 Maximum vertical pressure gradient under (a): wave crest and (b): wave trough.

### 3.3.4 Sediment concentration

Figure 3-11 demonstrates sediment concentration against wave steepness. Although the values were varied even in the same sediment compaction trials, differences between sediment concentrations for trials with low and high sediment compaction conditions were seen specially in the middle range of the wave steepness. In other words, sediment concentration values with low steepness were almost the same. Similarly, very close sediment concentration values were observed for waves with the high wave steepness.

As it was mentioned before, the upper sediment layers under both high and low sediment compaction levels, after passing some waves over the sandbar become very similar. It might be possible that steeper waves can change the upper sediment layer the level of compaction quickly. Therefore, the sediment concentrations under the same hydrodynamic conditions can show similar values.

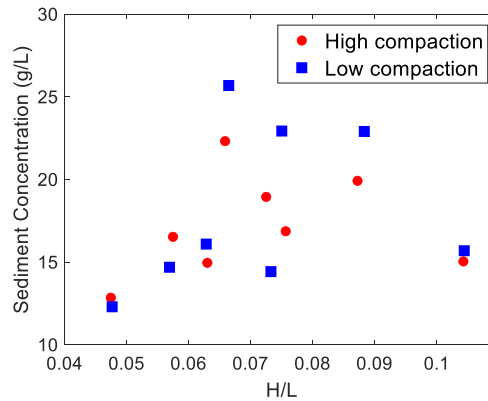


Figure 3-11 Averaged sediment concentration.

### 3.4 Conclusion

In this study, the response of sandbar as an important component of the beach profile to different hydrodynamic conditions under different sediment compaction levels was treated analytically. Observations in this research provided

a more holistic understanding of the effect of sediment compaction on the pore water pressure gradient within the sediment layers.

A sandbar was created within a small-scale 2D wave flume. Eight different wave conditions, with a 10-minute duration, were generated to transform across the sandbar profile with high and low sediment compaction conditions. Vertical components of pore water pressure were measured using an array of four pressure transducers buried within the sandbar. Sand grains suspended by waves were monitored using a concentration meter during the experiment.

The results indicate that in contrast to vertical pressure gradients, the magnitudes of maximum pore water pressure for trials with low sediment compaction conditions were larger than trials with high sediment compaction conditions. Additionally, the results revealed that the magnitudes of minimum pore water pressures had similar behavior to vertical pressure gradients. In other words, maximum pressure gradients in all trials revealed larger values under high compaction sediment conditions but larger values for the minimum and maximum pore water pressures and minimum pressure gradients were not observed in some trials.

In each trial, the pore water pressure near the bed surface was higher than at the lower sediment layers. It was observed for both low and high sediment compaction conditions. The range of differences between the maximum and minimum pore water pressure became smaller for the lower sediment layers. It was more significant for pore water pressures induced by waves with the shorter periods.

The level of sediment compaction had a significant effect on vertical pressure gradients. The rate of sediment compactions for the upper layer were observed almost the same for all trials. However, the rate of sediment compactions for the middle and top layers were up to about 2 and 1.6 times larger than the low compaction sediment conditions, respectively. Accordingly, the range of vertical

pressure gradients within sediments layers for high compaction conditions were varied from 1.1 to 1.8 times larger than low compaction conditions.

Depending on the pressure transducer positions and sediment compaction conditions, time lags between the measured pore water pressures were observed. These time lags can be due to both sediment compaction and the distance from the bed surface. Generally, the lower sediment layers showed larger time lags.

## 4 Statistical simulation of seabed response in surf zone

### 4.1 Introduction

The aim of this study is to provide a computationally efficient approach to model the joint probability and distribution for the height of the wave crest above the still-water level ( $\eta_{max}$ ), the maximum horizontal pressure gradient ( $\partial(P/\rho)/\partial x_{max}$ ) induced by  $\eta_{max}$ , and the maximum local horizontal acceleration ( $\partial u/\partial t_{max}$ ) induced by  $\eta_{max}$  within the surf zone of a natural coastal zone and a large-scale wave flume using a fully statistical approach. Initially, several theoretical marginal distribution functions were employed to fit the empirical cumulative probability of ( $\eta_{max}$ ,  $\partial(P/\rho)/\partial x_{max}$ ,  $\partial u/\partial t_{max}$ ). Subsequently, copula approaches were used to provide the dependence structures between variables. The importance of the pressure gradient and current acceleration for surf zone sandbars has been investigated extensively. Although numerous studies have been conducted to investigate the interdependency of coastal parameters using copula-based statistical modeling, the performance of copula approaches for simulating pressure gradients and acceleration is yet to be investigated.

### 4.2 Empirical and theoretical cumulative distribution functions

A The empirical cumulative distribution function (ECDF) in statistics represents the cumulative distribution probability of the measured data and is defined as follows:

$$P(n) = \frac{1}{n+1} \sum_{i=1}^n \alpha_i \quad (1)$$

where  $n$  is the total amount of measured data, and  $\sum_{i=1}^n \alpha_i$  represents the  $i$ th rank of the measured data.

Theoretical cumulative distribution functions (TCDFs, also known as marginal functions) have been proposed to fit the cumulative distribution probability based on their statistical characteristics. Extreme value (EV), normal, generalized extreme value (GEV), logistic, Nakagami, Rician, Weibull, inverse Gaussian, and gamma distributions were tested for fitting. Table 4-1 shows the equations of the TCDFs and their parameters selected for this study. The parameters of the TCDFs can be varied over a wide range to fit the curve of TCDFs with the ECDF.

Table 4-1 Theoretical Cumulative Distribution Function (TCDF) and corresponding fitting parameters.

Name	Equation	Parameter A	Parameter B	Parameter C
Extreme value	$y = \sigma^{-1} \exp\left(\frac{x-\mu}{\sigma}\right) \exp\left(-\exp\left(\frac{x-\mu}{\sigma}\right)\right)$	$\mu$ : location parameter	$\sigma$ : scale parameter	-
Normal	$y = \frac{1}{\sigma\sqrt{2\pi}} e^{-\frac{(x-\mu)^2}{2\sigma^2}}$	$\mu$ : mean	$\sigma$ : standard deviation	-
Generalized Extreme Value	$y = \sigma^{-1} \exp\left(-\left(1+k\frac{(x-\mu)}{\sigma}\right)^{\frac{1}{k}}\right) \left(1+k\frac{(x-\mu)}{\sigma}\right)^{-1-\frac{1}{k}}$	$k$ : shape parameter	$\sigma$ : scale parameter	$\mu$ : location parameter
Logistic	$y = \frac{\exp\left(\frac{x-\mu}{\sigma}\right)}{\sigma\left(1+\exp\left(\frac{x-\mu}{\sigma}\right)\right)^2}$	$\mu$ : mean	$\sigma$ : scale parameter	-
Nakagami	$y = 2\left(\frac{\mu}{\omega}\right)^\mu \frac{1}{\Gamma(\mu)} x^{(2\mu-1)} e^{-\frac{\mu}{\omega}x^2}$	$\mu$ : shape parameter	$\omega$ : scale parameter	-
Rician	$y = I_0\left(\frac{xs}{\sigma^2}\right) \frac{x}{\sigma^2} e^{-\frac{x^2+s^2}{2\sigma^2}}$	$s$ : noncentrality parameter	$\sigma$ : scale parameter	-
Weibull	$y = \frac{b}{a}\left(\frac{x}{a}\right)^{b-1} e^{-\left(\frac{x}{a}\right)^b}$	$a$ : scale parameter	$b$ : shape parameter	-
Inverse Gaussian	$y = \sqrt{\frac{\lambda}{2\pi x^3}} \exp\left(-\frac{\lambda}{2x\mu^2}(x-\mu)^2\right)$	$\mu$ : scale parameter	$\lambda$ : shape parameter	-
Gamma	$y = \frac{1}{b^a\Gamma(a)} x^{(a-1)} e^{-\frac{x}{b}}$	$a$ : shape parameter	$b$ : scale parameter	-

To achieve a good estimation of the parameters, the maximum likelihood estimation (MLE) method was used. The goodness of fit (GOF) between the TCDFs and ECDFs was assessed using the two-sample Kolmogorov–Smirnov (KS) test. The KS test, expressed as  $F_n(x)$ , is a nonparametric hypothesis test that evaluates the difference between the TCDF and ECDF values. In other words, the KS test can be used to reach a decision regarding the GOF of selected TCDFs using the following equation:

$$F_n(x) = \frac{1}{n} \sum_{i=1}^n I_{[-\infty, x]}(X_i) \quad (2)$$

where  $I_{[-\infty, x]}(X_i)$  are indicator functions. The KS test is based on the null hypothesis. If  $X_i < x$ , then the indicator function equals 1, which indicates the rejection of the null hypothesis; otherwise, the indicator factor equals 0, and the GOF of the cumulative distribution functions (CDFs) can be evaluated and ranked using asymptotic p-values ranging from 0 to 1.

### 4.3 Copula theory

A Theoretical foundation for the application of copulas is derived from Sklar's theorem (Sklar, 1959). According to Sklar's theorem, a copula function  $C$  describes the dependence structure between TCDFs, as follows:

$$F(x_1, x_2, \dots, x_n) = C[F_1(x_1), F_2(x_2), \dots, F_n(x_n)] \quad (3)$$

where  $F_1(x_1), F_2(x_2), \dots, F_n(x_n)$  are TCDFs, and  $x_1, x_2, \dots, x_n$  are random variables. By considering  $(X, Y)$  as two dependent variables, a joint distribution by specifying marginal univariate distributions,  $u = F_X(x)$  and  $v = F_Y(y)$ , can be constructed as  $F_{XY}(x, y)$ . Let

$$F_{XY}(x, y) = C(u, v) \quad (4)$$

where  $C$  is a copula function for any  $x$  and  $y$ . The unique values for  $C(u, v)$  can be obtained when  $F_X(x)$  and  $F_Y(y)$  are both continuous. Conversely, by considering  $C(u, v)$  as a copula and  $F_X(x)$  and  $F_Y(y)$  as distribution functions,  $C(u, v)$  can be a joint distribution function with margins of  $F_X(x)$  and  $F_Y(y)$ . Based on the assumption that the marginal functions are continuous, the random variables  $u$  and  $v$  are uniformly distributed within the range of 0 to 1. Copula

models are multivariate models with cumulative marginal distribution functions. Hence, the range values and domain for a copula model are distributed in the interval  $[0, 1]$ .

Based on Sklar's theorem, the joint density for marginal distributions with densities of  $f_X(x)$  and  $f_Y(y)$  can be defined as

$$f_{XY}(x, y) = f_X(x)f_Y(y)c(u, v) \quad (5)$$

where  $c(u, v)$  is the copula density, which is expressed as

$$c(u, v) = \frac{\partial^2 C(u, v)}{\partial u \partial v}. \quad (6)$$

In addition, the conditional distribution function can be derived via the partial differentiation of the joint distribution functions, as follows:

$$P(V \leq v|U = u) = \frac{\partial C(u, v)}{\partial u} \text{ and } P(U \leq u|V = v) = \frac{\partial C(u, v)}{\partial v}.$$

Let  $F_{X|Y}(x|y) = P(V \leq v|U = u)$  and  $F_{Y|X}(y|x) = P(U \leq u|V = v)$ . Therefore, the conditional density can be expressed as follows:  $f_{X|Y}(x|y) = f_X(x)c(u, v)$  and  $f_{Y|X}(y|x) = f_Y(y)c(u, v)$ .

One of the advantages of the copula compared with the other joint distribution models is the freedom to select any TCDFs for the variables; this is because the copula approach creates a dependency structure between correlated variables by selecting the TCDFs independently. Various types of bivariate parametric copula families and classes have been proposed. Each of these families or classes exhibits various characteristics. Among them, Archimedean and elliptical families, which are frequently applied in coastal engineering, were selected for this study.

#### 4.4 Dependency construction using copula approach

To construct a dependence structure among the water level, local acceleration, and pressure gradient, Archimedean copulas (including the Clayton, Frank, and Gumbel–Hougaard copulas) and elliptical copulas (including the Gaussian and Student's t copulas) were considered in this study. In general, these copulas encompass a wide range of dependency and correlation patterns. However, the compatibility of these copulas with the dependence variables must be ensured via GOF tests. The theoretical proofs and mathematical justifications for the construction of these copulas are presented below.

##### 4.4.1 Archimedean copulas

In practice, Archimedean copulas are frequently applied in several fields of study (Kwon and Lall, 2016; Bacigál et al., 2019; Garcia-Jorcano and Benito, 2020). Because the family of Archimedean copulas comprises a wide range of possible dependency patterns and properties, they can be easily constructed (Nelsen, 2006). Generally, an Archimedean copula based on an algebraic method can be written as follows:

$$C(u, v) = \varphi^{-1}(\varphi(u) + \varphi(v)) \quad (7)$$

where  $u = F_X(x)$  and  $v = F_Y(y)$  are marginal functions;  $\varphi$  is the generator function with domain  $\theta = [0, \infty)$ ;  $\varphi^{-1}$  is the inverse function of  $\varphi$  and can be generally expressed as

$$\varphi^{-1}(t, \theta) = \begin{cases} \varphi^{-1}(t, \theta) & \text{if } 0 \leq t \leq \varphi(0, \theta) \\ 0 & \text{if } \varphi(0, \theta) \leq t \leq \infty \end{cases} \quad (8)$$

where  $t$  is a random number between zero and one. Clayton, Gumbel, and Frank copulas, which are the most well-known one-parameter families of Archimedean copulas, were used in this study. These copula functions, their

generator functions, and the domain of the generator functions are shown in Table 4-2.

Archimedean copulas present different and special tail dependencies based on their generator functions. For example, the Gumbel copula presents upper tail dependence and is more appropriate for data with significant dependencies at higher values than at low values. By contrast, the Clayton copula presents a lower tail dependence and is suitable for data with significant low-value dependencies, whereas the Frank copula presents no tail dependence and is an appropriate model for data with weak dependencies.

*Table 4-2 Archimedean copula governing functions.*

Copula	Function	Generator	$\theta \in$
Clayton	$[\max(u^{-\theta} + v^{-\theta} - 1, 0)]^{-1/\theta}$	$(t^{-\theta} - 1)/\theta$	$(1, +\infty)$
Gumbel-Hougaard	$\exp(-[(-\ln u)^\theta + (-\ln v)^\theta]^{1/\theta})$	$(-\ln t)^\theta$	$[1, +\infty)$
Frank	$-\frac{1}{\theta} \ln\left(1 + \frac{(e^{-\theta u} - 1)(e^{-\theta v} - 1)}{(e^{-\theta} - 1)}\right)$	$-\ln \frac{e^{-\theta t} - 1}{e^{-\theta} - 1}$	$(-\infty, +\infty)$

#### 4.4.2 Elliptical copulas

The Gaussian and Student's t copulas, as the most typically recommended members of the elliptical copulas, were applied to simulate the variables in this study. The main advantage of elliptical copulas is that they can easily generalize to a high number of dimensions. The elliptical copulas mentioned above are presented below.

##### 4.4.2.1 Gaussian copula

The Gaussian or normal copula is a member of the elliptical copula family. This copula can easily simulate a high number of dimensions as it is an  $n$ -variate

distribution over the unit cube  $[0, 1]^n$ . By assuming  $x_1, \dots, x_n$  as a set of correlated variables with a correlation matrix  $R \in [-1, 1]^{n \times n}$ , the Gaussian copula can be defined as

$$C_R(u) = \varphi_R(\varphi^{-1}(u_1), \dots, \varphi^{-1}(u_n)) \quad (9)$$

where  $\varphi_R$  denotes the  $n$ -dimensional normal distribution function, and  $\varphi^{-1}$  the inverse cumulative distribution function of the standard normal. Therefore, the multivariate CDF is expressed as

$$\begin{aligned} F(x_1, \dots, x_n) &= C(F_1(x_1), \dots, F_n(x_n)) \\ &= \varphi_R(\varphi^{-1}(F_1(x_1)), \dots, \varphi^{-1}(F_n(x_n))) \end{aligned} \quad (10)$$

Finally, the mathematical formulation of the Gaussian copula can be written as follows:

$$\begin{aligned} C(u, v) &= \int_{-\infty}^{\varphi^{-1}(u)} \int_{-\infty}^{\varphi^{-1}(v)} \frac{1}{2\pi(1-\theta^2)^{1/2}} \exp\left\{-\frac{x^2 - 2\theta xy + y^2}{2(1-\theta^2)}\right\} dx dy \\ &\quad -1 \leq \theta \leq 1 \end{aligned} \quad (11)$$

#### 4.4.2.2 Student's t copula

The Student's t copula represents the dependence structure of a multivariate Student's t distribution. In fact, the Student's t distribution is a generalization of the Gaussian distribution, and the Gaussian copula is a limited version of the Student's t copula with a limited degree of freedom. Compared with the Gaussian copula, the Student's t copula performs better in capturing the dependence between variables in a dataset.

If  $x_1, \dots, x_n$  is a set of correlated variables with a correlation matrix  $R \in [-1, 1]^{n \times n}$ , then the Student's t copula can be defined as

$$C_{vR}(u) = t_{vR}(t^{-1}(u_1), \dots, t^{-1}(u_n)) \quad (12)$$

where  $t_{vR}$  denotes the one-dimensional Student's t distribution function with  $v$  degrees of freedom, and  $t^{-1}$  the inverse Student's t cumulative distribution function with  $v$  degrees of freedom. The Student's t copula can be expressed as follows:

$$C(u, v) = \int_{-\infty}^{t^{-1}(u)} \int_{-\infty}^{t^{-1}(v)} \frac{1}{2\pi(1-\theta^2)^{1/2}} \left\{ 1 + \frac{x^2 - 2\theta xy + y^2}{v(1-\theta^2)} \right\}^{-(\delta+2)/2} dx dy \quad -1 \leq \theta \leq 1, \delta \geq 2 \quad (13)$$

#### 4.5 Simulation based on constructed copulas

To simulate dependent multivariate data using a copula, the following procedures were implemented. First, the linear correlation coefficient was calculated to specify the linear correlation between variables. In this regard, Kendall's  $\tau$  or Spearman's  $\rho$  are appropriate. Kendall's  $\tau$ , which ranges from -1 to 1, is a non-parametric approach for measuring the association between two variables. The correlation between two variables is perfect when the coefficient value is 1. Similarly, a value of -1 indicates a perfect negative correlation between two variables. Moreover, the coefficient is expected to be approximately zero when the two variables are independent. Kendall's  $\tau$  depends only on the copula  $C$ , and for a pair of dependent variables  $(u, v)$ , it is defined as

$$\tau = 4 \int_0^1 \int_0^1 C(u, v) dC(u, v) - 1. \quad (14)$$

For Archimedean and elliptical copulas, Kendall's  $\tau$  can be expressed as a function of the generator. For example, Kendall's  $\tau$  for Archimedean copulas can be estimated as follows:

$$\tau = 1 + 4 \int_0^1 \frac{\varphi(t)}{\varphi'(t)} dt. \quad (15)$$

Similar to Kendall's  $\tau$ , Spearman's  $\rho$  assesses the correlation level between two variables. In addition, the values of Spearman's  $\rho$  are between -1 and 1. Spearman's  $\rho$  is expressed as follows:

$$\rho = 12 \int_0^1 \int_0^1 C(u, v) du dv - 3. \quad (16)$$

Here,  $\rho$  can be expressed as a function of the generator. For Archimedean copulas,  $\rho$  is defined as

$$\tau = 3 + 12 \int_0^1 \frac{\varphi(t)}{\varphi'(t)} dt. \quad (17)$$

Second, the TCDF of each variable was estimated and fitted to their calculated ECDFs. Subsequently, the data were fitted to different copulas using the MLE method. Next, random values between 0 and 1 were generated from the fitted copulas. Finally, the generated values were inverted to achieve the original scale data using inverse functions.

## 4.6 Data acquisition

### 4.6.1 Field setup and data

The field data employed in this study were based on a field experiment conducted by Suzuki et al. (2009) during a five-day experiment on February 16–20, 2007, at the Hasaki Oceanographical Research Station (HORS), a research facility operated by the Port and Airport Research Institute in Japan. The HORS is located in Ibaraki Prefecture, approximately 100 km east of Tokyo, and faces the Pacific Ocean (Figure 4-1). The shoreline orientation was 31° anticlockwise from the north. A 427-m-long pier equipped with different instruments for various field measurements was located perpendicular to the Hasaki shoreline. The HORS is

situated on a sandy coast composed of fine sand with a median sediment grain of approximately 0.18 mm, as reported by Katoh and Yanagishima (1995). The mean water level during the experiment was 0.651 m, based on the datum level at the HORS (Tokyo Peil: 0.687 m). Additionally, the low and high water levels were -0.196 and 1.252 m, respectively. Hence, the HORS had a mean tide range of 1.5 m during the experiment. The offshore wave data was recorded at a depth of 23.4 m off the Kashima port.

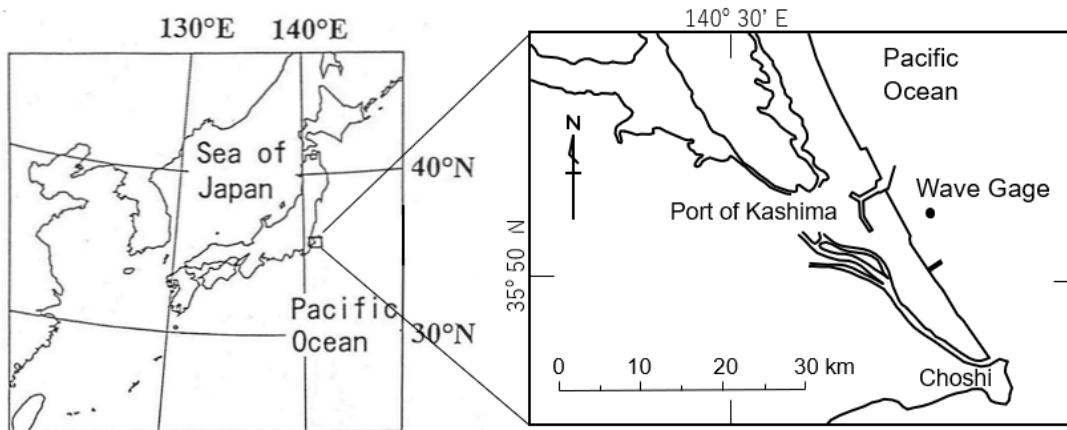


Figure 4-1 Location of Hasaki Oceanographical Research Station (HORS)

Figure 4-2 shows the cross-shore beach profile on the first day of the measurements as well as the instrumentation setup. Three instrument sets were used in the experiment to measure the water level, velocity, water pressure, and sediment concentration. The water levels were recorded using a capacitance-type wave gauge (CHT5-200, KENEK). The velocities were recorded using three Nortek acoustic Doppler velocimeters (ADV) positioned 10 cm above the bed. Pressure gradients were estimated using data recorded by an array of pressure transducers composed of five sensors (BPR-A-50KPS, KYOWA). Sediment concentrations were recorded using three optical backscatter sensors (OBS-3, D&A Instrument Comp.) Additional details regarding the field measurements and

instrumentation can be obtained from the paper by Suzuki et al. (2009). It is noteworthy that seabed erosion occurred after installation; consequently, the seabed level around the array of instruments decreased. Therefore, to avoid the effect of erosion, only data measured on the first day were used in this study. Figures 4-3 show the measurement result in the first round of this experiment.

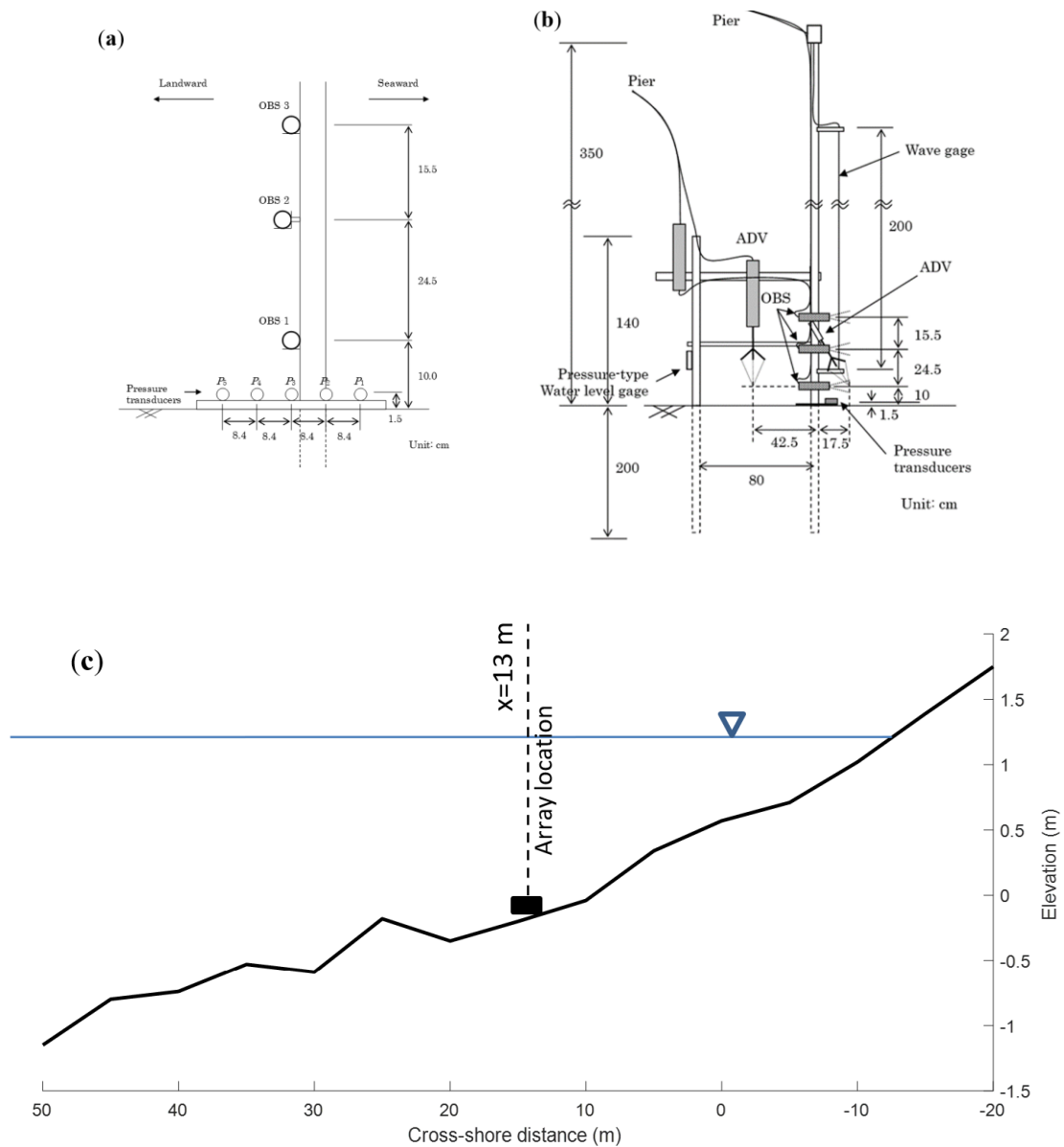


Figure 4-2 Instrument arrangement: (a) Pressure transducers and sediment concentration profiler arrangement, (b) the instrument locations from the top view of the deck, and (c) cross-shore beach profile morphology.

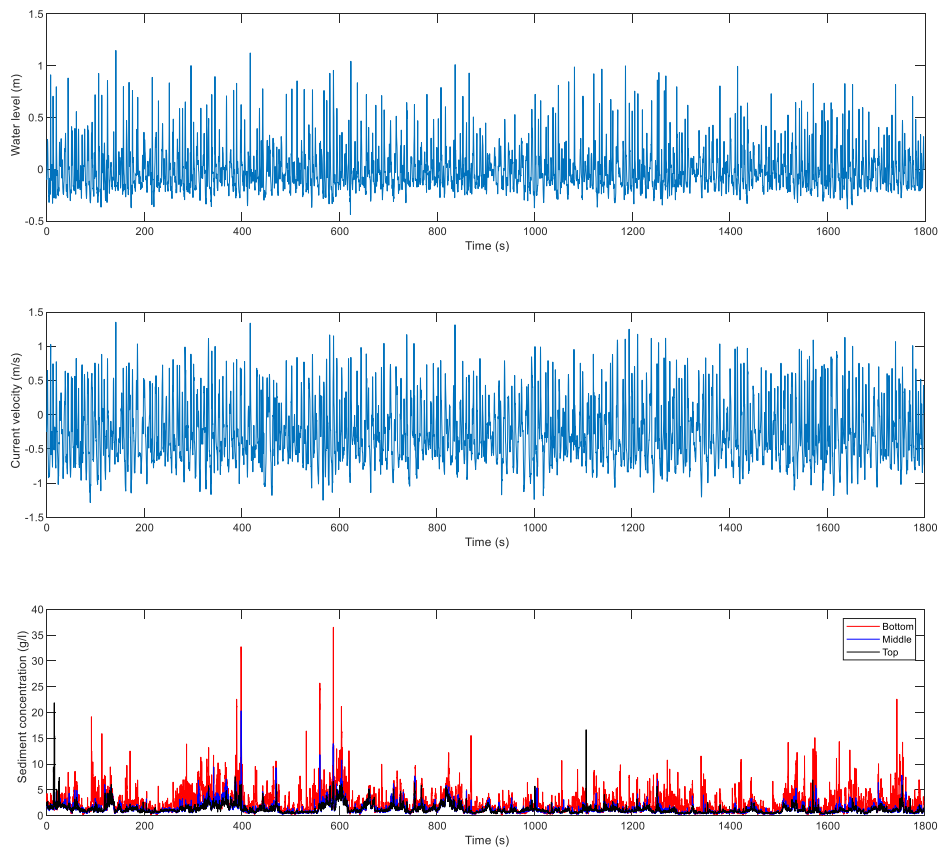


Figure 4-3 Time series of measured parameters at HORS.

#### 4.6.2 Laboratory instrumentation and data

In this study, experimental tests were conducted by Mieras et al. (2017) and Anderson et al. (2017) in a large-scale wave flume at the O. H. Hinsdale Wave Research Laboratory at the Oregon State University (Figure 4-4) were used. The flume had a length of 104 m, a width of 3.7 m, and a depth of 4.6 m, with a fixed barred beach profile constructed based on the average observed beach profile on 11 October 1994 from Duck, NC, during the Duck94 field experiment (Faria et al., 1997; Scott et al., 2005) conducted at the U.S. Army Corps of Engineering Field Research Facility.

The fixed barred profile comprised impermeable slopes of concrete slabs to ensure repeatability, and morphological changes did not cause the position of wave breaking to vary during the experiment. A sand pit composed of two sections was installed on the sandbar crest. The main section had a width of 3.66 m with a depth of 0.18 m. To install the experimental instruments, a subsection with a length and width of 1.2 m and a total depth of 0.61 m was installed beneath the main sand pit. The sand pit was filled with sediments of two different sizes. Because most of the trials were conducted using sediments with  $D_{50} = 0.17$  mm,  $D_{16} = 0.10$  mm, and  $D_{84} = 0.28$  mm, only data obtained from trials using  $D_{50} = 0.17$  mm were used in this study.

A series of approximately 10 monochromatic waves with three different wave periods, i.e.,  $T = 5, 7, \text{ and } 9$  s, was conducted for each trial. The wave heights for each wave within a trial were measured at the toe of the beach profile ( $H_i$ ) and at the seaward boundary of the sandbar crest ( $H_{bar}$ ). The trials were conducted with wave heights  $H_i$  ranging from 0.09 to 0.65 m and  $H_{bar}$  ranging between 0.1 and 0.96 m. The waves were categorized based on the wave period and  $D_{50}$ , as summarized in Table 4-3.

The tests involved measurements of water surface elevation, pore water pressure, instantaneous bed bathymetry, and velocity. To measure the water surface elevations from offshore to onshore, 11 resistance-type wave gauges were deployed. The wave gauges starting from the toe of the beach profile, i.e., 17.7 m from the wave maker, were mounted along the flume wall at intervals of 3.65 m. A wave gauge positioned at the seaward boundary of the sandbar crest was deployed to record the wave transformation over the sandbar. In addition, a pressure gauge was installed immediately above the sediment bed to measure the water depth over the sandbar crest.

Table 4-3 Summary of wave condition

	$D_{50}(mm)$	$H_{bar}(m)$	$T(s)$
Group 1	0.17	0.10	3.5
		0.20	
		0.32	
		0.43	
		0.57	
		0.71	
Group 2	0.17	0.11	5
		0.23	
		0.36	
		0.54	
		0.63	
		0.73	
		0.82	
		0.87	
Group 3	0.17	0.59	7
		0.66	
		0.75	
		0.84	
		0.97	
Group 4	0.17	0.41	9
		0.49	
		0.55	
		0.63	
		0.70	
		0.77	

An array of seven GE Druck PDCR 81 pressure transducers composed of a horizontal row of five pressure transducers and a vertical row of two pressure transducers was embedded beneath the sediment to observe the pore pressure and pressure gradient (Figure 4-4). The pore pressure transducers were spaced equally at 20 mm intervals. A conductivity concentration profiler with a width of 5.6 mm and a thickness of 5.6 mm was installed in the sediment pit to measure the instantaneous bed bathymetry at 8 Hz with 1 mm resolution. Moreover, near-bed velocities were measured using a vertical array of Vectrino I ADVs mounted

approximately 0.1 m above the initial bed level. Additional details regarding the experimental setup, instrumentation, and test conditions can be available in Anderson et al. (2017), Mieras et al. (2017), and Mieras et al. (2019).

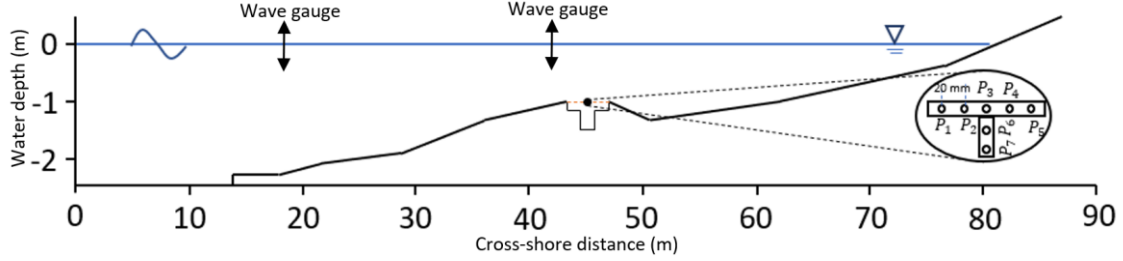


Figure 4-4 Instrumentation and experimental setup.

## 4.7 Data analysis

This research focuses on the dependency structure among the  $\eta_{max}$ , maximum horizontal pore pressure gradient ( $\partial(P/\rho)/\partial x_{max}$ ), maximum vertical pressure gradient ( $\partial(P/\rho)/\partial z_{max}$ ), maximum horizontal acceleration ( $\partial u/\partial t_{max}$ ), maximum vertical acceleration ( $\partial w/\partial t_{max}$ ), and maximum near-bed sediment concentration ( $C_{b,max}$ ) induced by  $\eta_{max}$  based on field and laboratory measured data. First, the results for each dataset were analyzed separately. Subsequently, the relationship between the two datasets was established.

### 4.7.1 Dependent field data

As described in the previous section, the water level, velocity, water pressure, and sediment concentration were measured as field data. The pressure gradients for each water level based on the central difference scheme were estimated as follows:

$$\frac{\partial p}{\partial x} = -\frac{p_1 - 8p_2 + 8p_4 - p_5}{12\Delta x} \quad (18)$$

where  $p$  is the pressure, the subscripts represent the position of each transducer, and  $\Delta x$  is the distance between the transducers, i.e., 8.4 cm. Furthermore, the accelerations were estimated using the measured wave induced velocities based on a centered difference approximation in time, as follows:

$$\frac{\partial u}{\partial t} = \frac{u(i) - u(i - 1)}{\Delta t} \quad (19)$$

where  $u$  is the wave induced velocity, and  $i$  the different time steps.

Wave-by-wave analysis was conducted to assess the measured parameter behaviors. Figures 4-5a, c, and e show the wave-induced pressure gradients, local accelerations, and bottom sediment concentration for different water levels, starting from the still water to maximum water levels for each wave. By considering the maximum water level as  $\eta_{max}$ , Figures 4b, d, f, and g show the multivariate  $(\eta_{max}, \partial(P/\rho)/\partial x_{max}, \partial u/\partial t_{max}, C_{b,max})$  assessed for the copula simulation of the field observations. Red dots in Figures 4-5 show the pressure gradients, local accelerations and sediment concentrations which are corresponding to  $\eta_{max}$ .

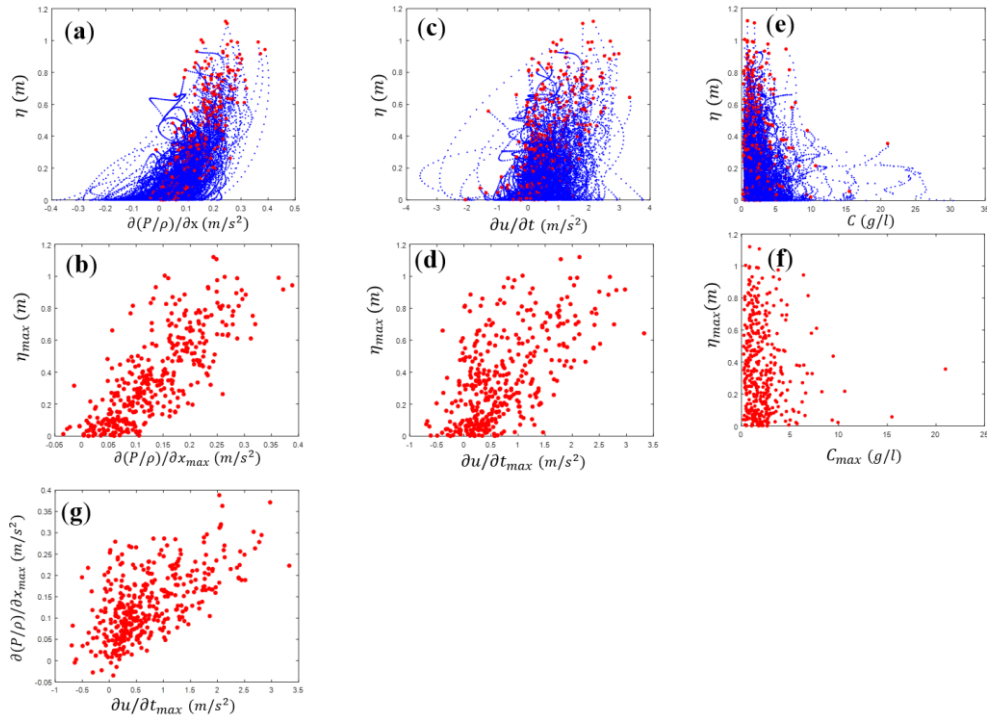


Figure 4-5 Scatterplots of pressure gradients (a), accelerations(c), and bottom sediment concentration (e) induced by different water levels ( $\eta$ ) above the still water level. Red dots denote maximum values corresponding to the maximum water level ( $\eta_{max}$ ); (b), (d), and (f) show maximum pressure gradients, accelerations, bottom sediment concentration, respectively. (g) Scatterplot of  $(\partial u/\partial t_{max}, \partial(P/\rho)/\partial x_{max})$ .

#### 4.7.2 Dependent laboratory data

Anderson et al. (2017) used a method similar to that of Suzuki et al. (2010) to calculate the pressure gradient in both the horizontal and vertical directions. The horizontal gradients can be estimated as follows:

$$\frac{\partial p}{\partial x} = \frac{-2p_2 - 3p_3 + 6p_4 - p_5}{6\Delta x} \quad (20)$$

where  $\Delta x$  was 2 cm. Positive and negative values for  $\partial p/\partial x$  indicate the offshore and onshore directions, respectively. Similarly, the vertical pore pressure gradient is calculated as follows:

$$\frac{\partial p}{\partial z} = \frac{-3p_3 + 4p_6 - p_7}{2\Delta z} \quad (21)$$

where  $\Delta z$  was 2 cm in this study, and positive values indicate the downward direction. Figure 4-6 shows wave induced maximum pore pressure gradients and their corresponding maximum accelerations.

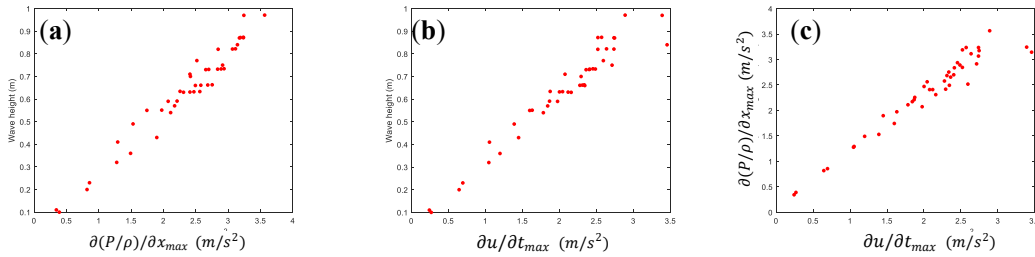


Figure 4-6 Scatterplots of  $(\partial(P/\rho)/\partial x_{max}, \text{Wave height})$ ,  $(\partial u/\partial t_{max}, \text{Wave height})$ , and  $(\partial u/\partial t_{max}, \partial(P/\rho)/\partial x_{max})$  represented by (a), (b), and (c), respectively.

## 4.8 Discussion

### 4.8.1 Multivariate analysis for copula simulation

To assess the correlation between variables, Kendall's  $\tau$  and the corresponding p-values were calculated, and the summary for each pair is presented in Table 4-4. As expected,  $\eta_{max}$  was significantly correlated with the pressure gradients and accelerations. This implies that the larger the  $\eta_{max}$ , the higher is the pressure gradients and accelerations. Meanwhile, the  $(\partial u/\partial t_{max}, \eta_{max})$  and  $(\partial u/\partial t_{max}, \partial(P/\rho)/\partial x_{max})$  pair indicated a significant positive dependence on the laboratory data, whereas a lower correlation was indicated in the field dataset. This can be attributed to the effect of several aggregated phenomena, such as the longshore currents within the surf zone in the natural coastal regions, which are negligible in the wave flume.

On the other hand, the calculated correlation factors between the wave periods and  $(\eta_{max}, \partial(P/\rho)/\partial x_{max}, \partial u/\partial t_{max})$  were not high enough to select for the copula simulation. It is noteworthy that  $\partial(P/\rho)/\partial z_{max}$  and  $\partial w/\partial t_{max}$  are independent. Similarly,  $C_{b,max}$  was not selected for the copula simulation owing to its low correlation with  $\eta_{max}$ . Finally, based on Kendall's  $\tau$ , it was observed that the dependencies among  $(\partial(P/\rho)/\partial x_{max}, \eta_{max})$ ,  $(\partial u/\partial t_{max}, \eta_{max})$ , and  $(\partial u/\partial t_{max}, \partial(P/\rho)/\partial x_{max})$  were perfectly linear for the laboratory dataset and reasonable for the field data. Therefore, the interdependency structure and simulation using the copula approach were provided for a three-dimensional multivariate analysis of  $(\eta_{max}, \partial(P/\rho)/\partial x_{max}, \partial u/\partial t_{max})$ . To render the laboratory data applicable to the field data and to generalize both laboratory and field data for different coastal locations, the datasets were normalized by their root mean square (RMS) values. Figure 4-7 shows the normalized multivariate  $(\eta_{max}, \partial(P/\rho)/\partial x_{max}, \partial u/\partial t_{max})$  for both the laboratory and field datasets.

Table 4-4 Kendall's  $\tau$  correlation coefficient between measured parameters.

Parameters	Field dataset	Laboratory dataset
$\partial P/\partial x_{max}$ vs $\eta_{max}$	0.78	0.97
$\partial u/\partial t_{max}$ vs $\eta_{max}$	0.58	0.97
$\partial u/\partial t_{max}$ vs $\partial P/\partial x$	0.60	0.93
$C_{max}$ vs $\eta_{max}$	-0.0943	-

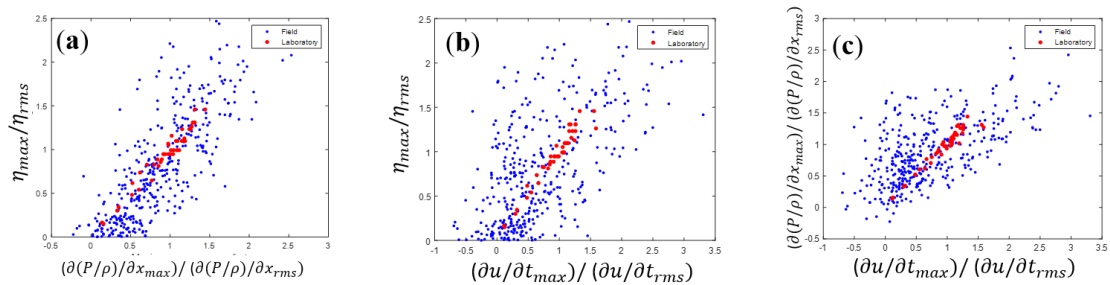


Figure 4-7 Comparison between scatterplots of normalized field and laboratory data.

#### 4.8.2 Distributions and estimations of CDFs

The marginal distributions or TCDFs, as a first step for simulating the correlated variables using the copula approach, should be determined. Therefore, the empirical probabilities for  $(\eta_{max}, \partial(P/\rho)/\partial x_{max}, \partial u/\partial t_{max})$  were calculated using Eq. (1). The TCDFs summarized in Table 4-1 were selected from among the available TCDFs to fit the distribution of cumulative probabilities. The parameters of the TCDFs were approximated using the MLE method.

Figures 4-8 and 9 show the ECDFs of the experimental data (blue asterisks) and TCDFs applicable to non-dimensional  $(\eta_{max}, \partial(P/\rho)/\partial x_{max}, \partial u/\partial t_{max})$ . The estimated parameters for fitting the TCDFs to the ECDFs are provided in Table 4-5 in the Appendix. The values of  $(\eta_{max}, \partial(P/\rho)/\partial x_{max}, \partial u/\partial t_{max})$  were normalized using their RMS values. Generally, the laboratory results of the CDF calculations show that the values of ECDFs for small waves and the associated low pressure gradients and accelerations were higher than those of the TCDFs, whereas the values of the ECDFs for  $\langle \eta_{max} \rangle, \langle \partial(P/\rho)/\partial x_{max} \rangle, \langle \partial u/\partial t_{max} \rangle = 0.5$  to 1, where  $\langle \rangle$  denotes the normalized values, were relatively lower than those of the TCDFs. Additionally, the peak values of the ECDFs were higher than the corresponding TCDF values. It can be concluded that for  $\langle \eta_{max} \rangle, \langle \partial(P/\rho)/\partial x_{max} \rangle, \langle \partial u/\partial t_{max} \rangle = 0$  to 0.5 and for values less than 1, the TCDFs were underestimated, whereas for values between 0.5 to 1, they were overestimated. In addition, the field results of  $\langle \partial(P/\rho)/\partial x_{max} \rangle$  and  $\langle \partial u/\partial t_{max} \rangle$  included negative values, and the TCDFs showed overestimated results. Similarly, for values between 0 and 0.5, it can be concluded that the values of the ECDFs were lower than the estimated values of the TCDFs. The Nakagami function was the only TCDF that fitted well with the field wave height data. Although the Nakagami function yielded favorable results for  $\langle \eta_{max} \rangle$  and  $\langle \partial(P/\rho)/\partial x_{max} \rangle$ , its performance was not reliable for  $\langle \partial u/\partial t_{max} \rangle$ .

Table 4-5 Probability distribution parameters and GOF results for normalized field and laboratory data.

	Rank	Name	Parameter A	Parameter B	Parameter C	P-Value	
<b>Field</b>	$\eta_{max}$	1	Nakagami	0.4520	1	-	0.8034
		2	Weibull	0.8411	1.1730	-	0.3936
		3	Generalized Extreme Value	0.0601	0.4610	0.5050	0.2334
	$\frac{\partial P}{\partial x}$	1	Nakagami	1.2302	1.4595	-	0.9950
		2	Weibull	1.2376	2.2940	-	0.9939
		3	Generalized Extreme Value	-0.1323	0.4512	0.8874	0.9697
		4	Rician	0.8620	0.5985	-	0.9381
		5	Gamma	3.9064	0.2810	-	0.8099
		6	Logistic	0.0089	0.3047	-	0.6894
		7	Normal	1.0976	0.5053	-	0.3920
		8	Rayleigh	0.8542	-	-	0.3280
	$\frac{\partial U}{\partial t}$	1	Generalized Extreme Value	-0.0026	0.5593	1.0787	0.6883
		2	Gamma	3.4941	0.4014	-	0.3790
		3	Weibull	1.5826	2.0564	-	0.3441
		4	Nakagami	1.0803	2.4750	-	0.2997
		5	Rayleigh	1.1124	-	-	0.2458
		6	Rician	0.1037	1.1103	-	0.2458
	<b>Laboratory</b>	$\eta_{max}$	1	Extreme Value	1.0935	0.2510	-
2			Generalized Extreme Value	-0.5567	0.3456	0.8802	0.9955
3			Logistic	0.9796	0.1746	-	0.9585
4			Normal	0.9484	0.3210	-	0.6666
5			Rician	0.8823	0.3328	-	0.6666
6			Weibull	1.0500	3.4652	-	0.6666
7			Nakagami	1.8577	1	-	0.3335
8			Gamma	5.5197	0.1718	-	0.3149
$\frac{\partial P}{\partial x}$		1	Extreme Value	1.09	0.26	-	0.9996
		2	Generalized Extreme Value	-0.48	0.35	0.86	0.9314
		3	Logistic	0.97	0.18	-	0.9290
		4	Normal	0.95	0.32	-	0.8476
	5	Rician	0.87	0.34	-	0.8476	
	6	Weibull	1.05	3.32	-	0.8476	
	7	Nakagami	1.76	1	-	0.4949	
	8	Gamma	4.71	0.2	-	0.4752	
	9	Rayleigh	0.7	-	-	0.2027	
$\frac{\partial U}{\partial t}$	1	Generalized Extreme Value	-0.4396	0.3621	0.8484	0.9338	
	2	Extreme Value	1.0980	0.2835	-	0.9338	
	3	Logistic	0.9732	0.1861	-	0.9338	
	4	Normal	0.9416	0.3407	-	0.8614	
	5	Rician	0.8647	0.3551	-	0.8405	
	6	Weibull	1.0452	3.1198	-	0.6922	
	7	Nakagami	1.6008	1	-	0.4713	
	8	Gamma	4.6353	0.2031	-	0.3210	

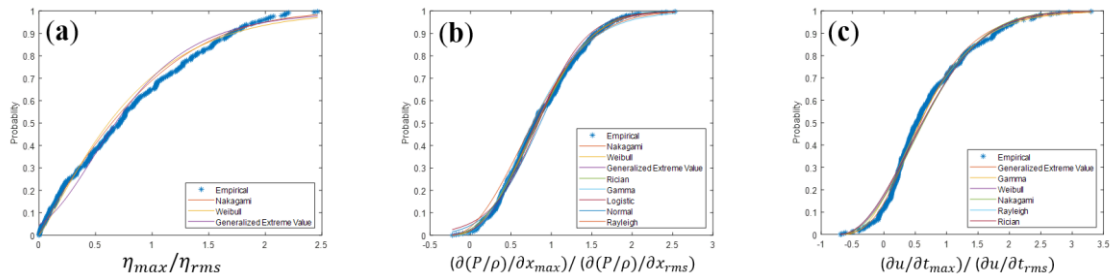


Figure 4-8 ECDFs of measured data and TCDFs applicable to normalized field data.

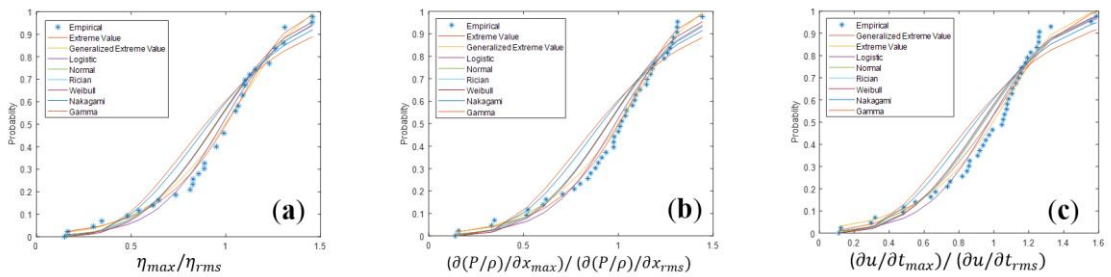


Figure 4-9 ECDFs of measured data and TCDFs applicable to normalized laboratory data.

The GEV distribution as a TCDF with three parameters showed excellent agreement with the laboratory experimental data. Meanwhile, the EV and logistic distributions with two parameters indicated excellent trends for the ECDFs involving the laboratory data, unlike the case for the field dataset calculations. The p-values from the KS tests for the field variable statistical investigations indicated no significant superiorities among the GEV, EV, and logistic distributions because their p-values exceeded 90%. However, the GEV distribution required two empirical parameters, and compared with the EV and logistic distributions, the computational procedure was more complicated. Meanwhile, the low p-values for the Nakagami and Gamma distributions indicated that they did not fit well with the laboratory data compared with the GEV, EV, and logistic distributions. Based on the p-values, the normal, Rician, and Weibull distributions demonstrated

relatively good agreement with the laboratory data. However, it was difficult to select the appropriate distribution among them based on the KS test because they demonstrated similar characteristics.

Figure 4-10a shows a comparison between the marginal functions for field and laboratory data based on p-values. The results indicate that the range of p-values was wide. Therefore, the marginal functions yielded different performances based on the dataset. By contrast, similar fitting parameters were achieved for each coastal parameter regardless of the study location (Figure 4-10b).

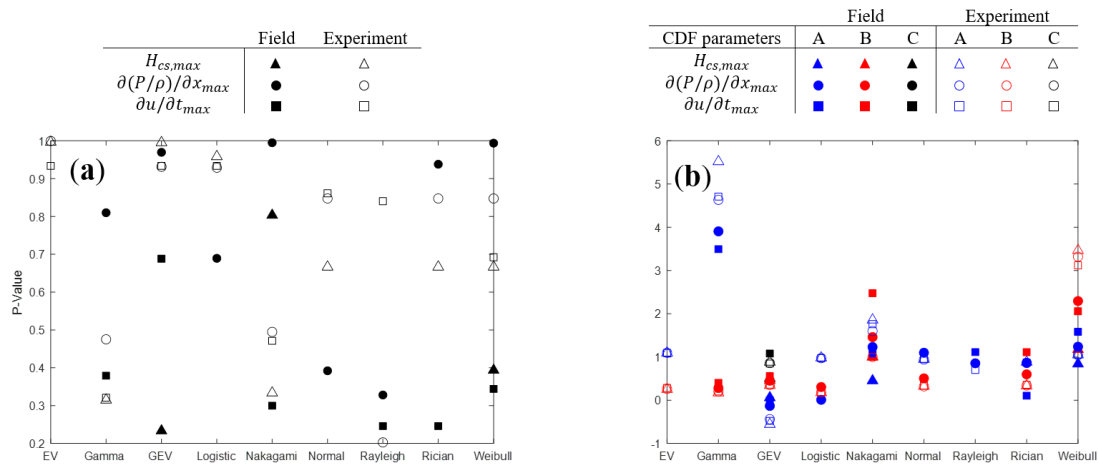


Figure 4-10 Comparison of p-values (A) and TCDFs fitting parameters (B) for field and experimental data.

### 4.8.3 Fitting data to different copulas and comparison of GOFs

The Archimedean and elliptical copulas discussed in Sections 4.3.1 and 4.3.2, respectively, were employed to model the dependency between the variables. The joint probabilities for  $(\eta_{max}, \partial(P/\rho)/\partial x_{max})$  and their corresponding simulated data are shown in Figures 4-11 to 22. For the GOF analysis, the corrected Akaike Information Criteria (AICc) was used. AICc can be calculated by

$$AICc = -2LL + 2P + \frac{2(P + 1)(P + 2)}{n - P - 2} \quad (22)$$

where  $LL$  is the maximized value of the log-likelihood function for the model,  $P$  is the number of parameters, and  $n$  is the sample size. Smaller AICc values indicate better simulation results (Table 4-6). The estimated correlation coefficients, such as Kendall's  $\tau$ , indicate a high linear dependency between the variables. Hence, symmetric copulas such as Archimedean and elliptical copulas can be expected to yield reasonable results. The AICc test was used to compare the performances of the copulas adopted.

Table 4-6 AICc test results for simulations

AICc	$\eta_{max}$ vs $\partial P/\partial x_{max}$		$\eta_{max}$ vs $\partial u/\partial t_{max}$		$\partial P/\partial x_{max}$ vs $\partial u/\partial t_{max}$	
	Field	Laboratory	Field	Laboratory	Field	Laboratory
Clayton	17302	8728	17487	8736	17367	8766
Frank	17461	8699	17566	8723	17373	8698
Gumbel	17492	8749	17384	8694	17384	8870
Student's t	17403	8709	17445	8685	17394	8744
Gaussian	17377	8707	17449	8698	17421	8759

The calculated p-values imply that the field data can be analyzed using Archimedean and elliptical copulas. Among the Archimedean copulas, the Clayton and Frank copula generally performed better than the other member of the Archimedean family. Based on the results, it can be concluded that the Gumbel copula is not a good candidate for simulating the field data of  $(\eta_{max}, \partial(P/\rho)/\partial x_{max})$  and  $(\partial(P/\rho)/\partial x_{max}, \partial u/\partial t_{max})$  then could not accurately characterize the dependency between data points. Nevertheless, the performance of the simulations for  $(\eta_{max}, \partial(P/\rho)/\partial x_{max}, \partial u/\partial t_{max})$  can be ranked as follows:

## Field dataset

- $(\eta_{max}, \partial(P/\rho)/\partial x_{max})$ : Clayton > Gaussian > Student's t > Frank > Gumbel.
- $(\eta_{max}, \partial u/\partial t_{max})$ : Gumbel > Student's t > Gaussian > Clayton > Frank.
- $(\partial(P/\rho)/\partial x_{max}, \partial u/\partial t_{max})$ : Clayton > Frank > Gumbel > Student's t > Gaussian

## Laboratory dataset

- $(\eta_{max}, \partial(P/\rho)/\partial x_{max})$ : Frank > Gaussian > Students' t > Clayton > Gumbel.
- $(\eta_{max}, \partial u/\partial t_{max})$ : Student's t > Gumbel > Gaussian > Frank > Clayton.
- $(\partial(P/\rho)/\partial x_{max}, \partial u/\partial t_{max})$ : Frank > Student's t > Gaussian > Clayton > Gumbel.

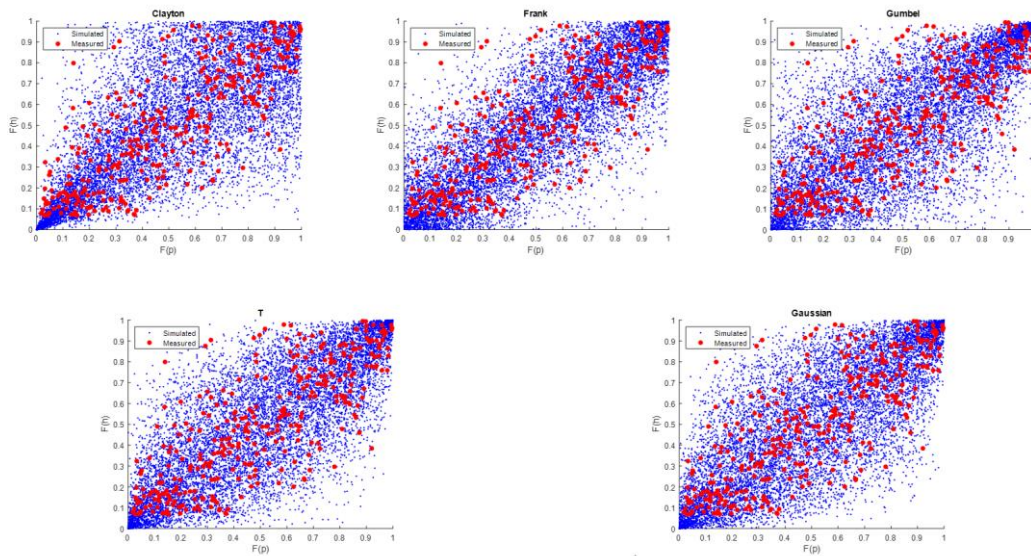


Figure 4-11 Scatterplots of joint probability for observed and simulated field data for  $(\eta_{max}, \partial(P/\rho)/\partial x_{max})$ .

Observed and simulated data shown by red and blue dots, respectively.

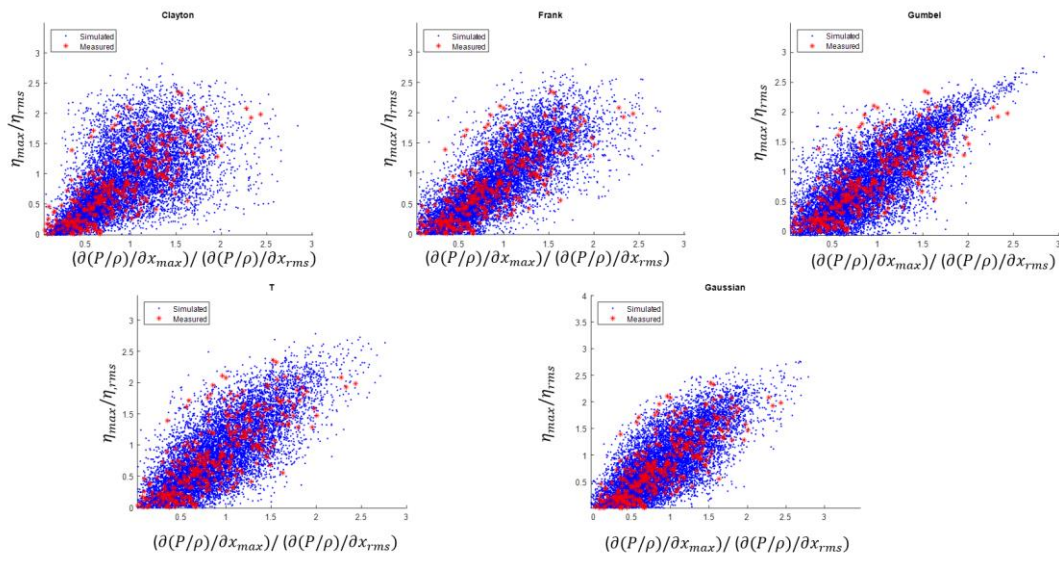


Figure 4-12 Scatterplots of observed and simulated field data for  $(\eta_{max}, \partial(P/\rho)/\partial x_{max})$ . Observed and simulated data shown by red and blue dots, respectively.

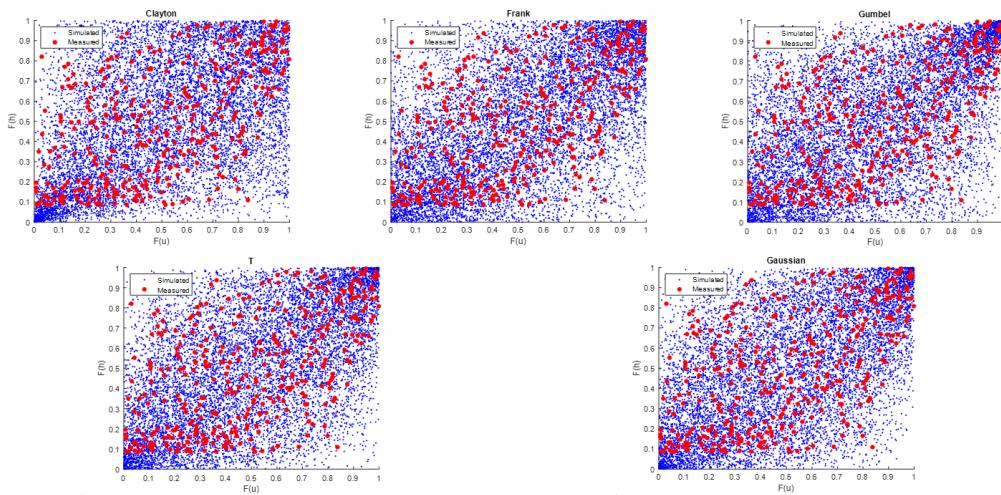


Figure 4-13 Scatterplots of joint probability for observed and simulated field data for  $(H_{s,max}, \partial u/\partial t_{max})$ . The observed and simulated data are shown by the red and blue dots, respectively.

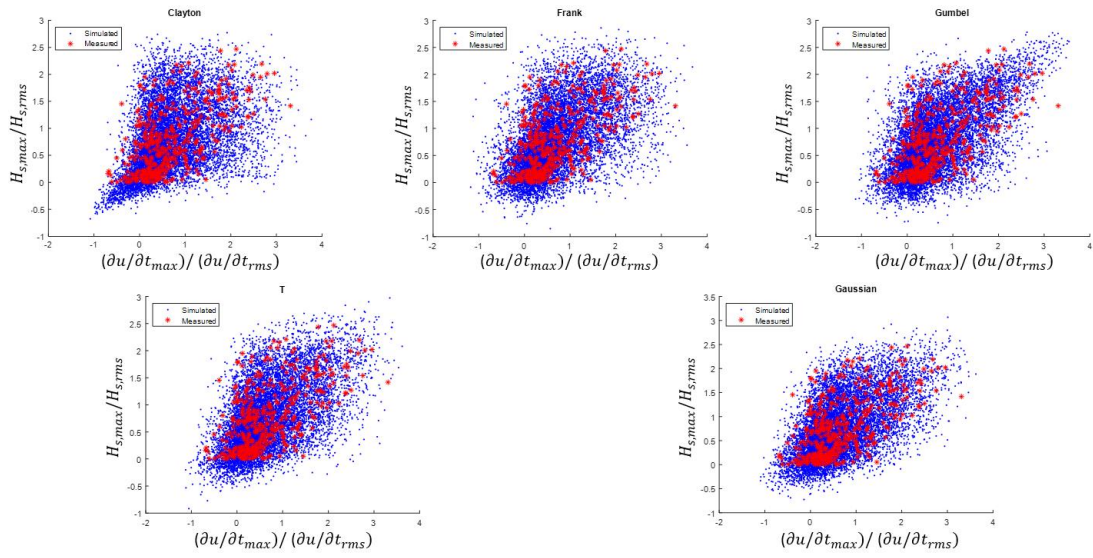


Figure 4-14 Scatterplots of observed and simulated field data for  $(H_{s,max}, \partial u/\partial t_{max})$ . The observed and simulated data are shown by the red and blue dots, respectively.

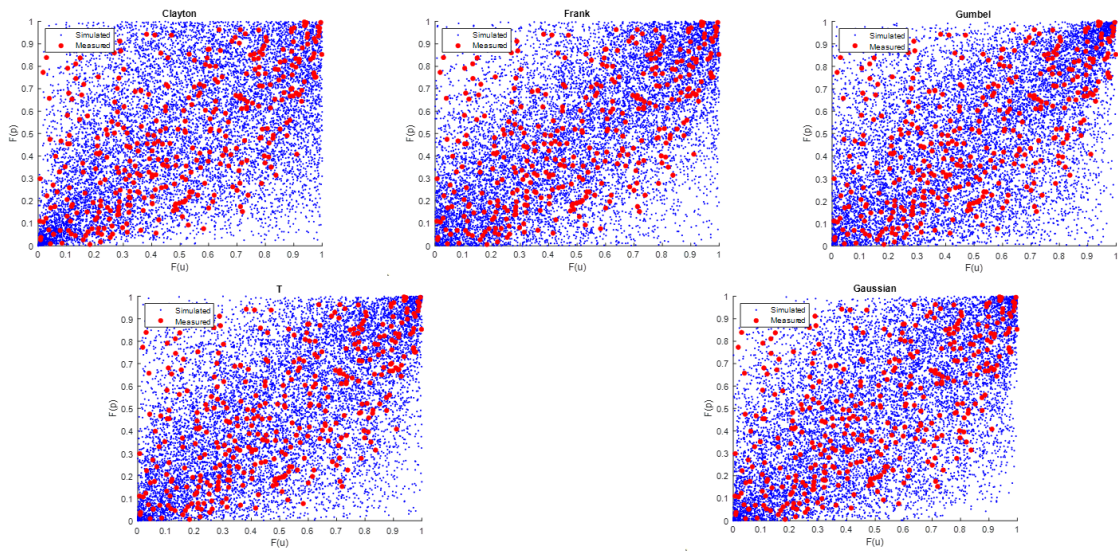


Figure 4-15 Scatterplots of joint probability for observed and simulated field data for  $(\partial(P/\rho)/\partial x_{max}, \partial u/\partial t_{max})$ . The observed and simulated data are shown by the red and blue dots, respectively.

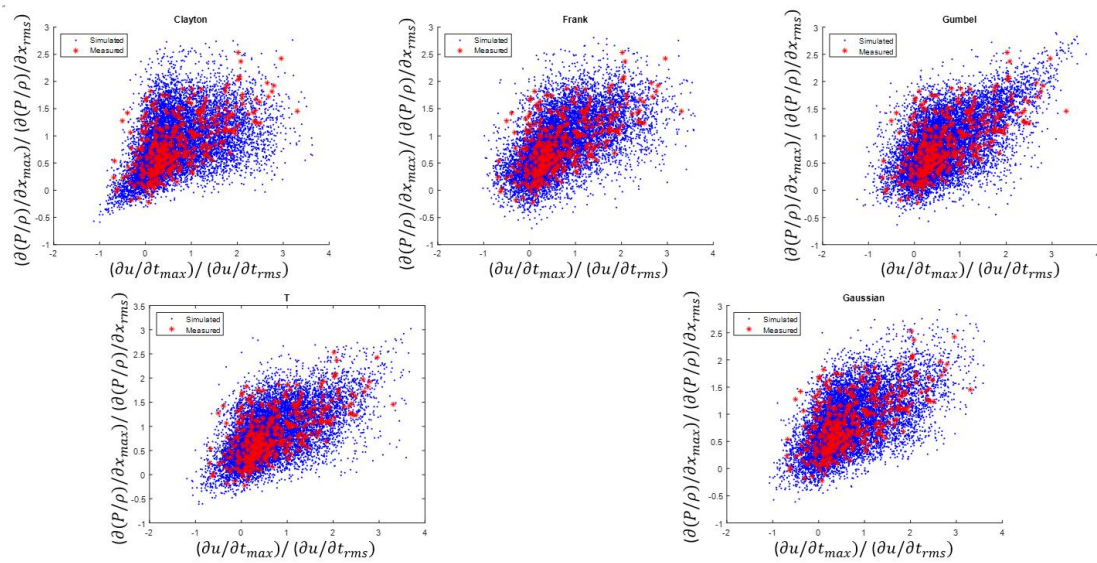


Figure 4-16 Scatterplots of observed and simulated field data for  $(\partial(P/\rho)/\partial x_{max}, \partial u/\partial t_{max})$ . The observed and simulated data are shown by the red and blue dots, respectively.

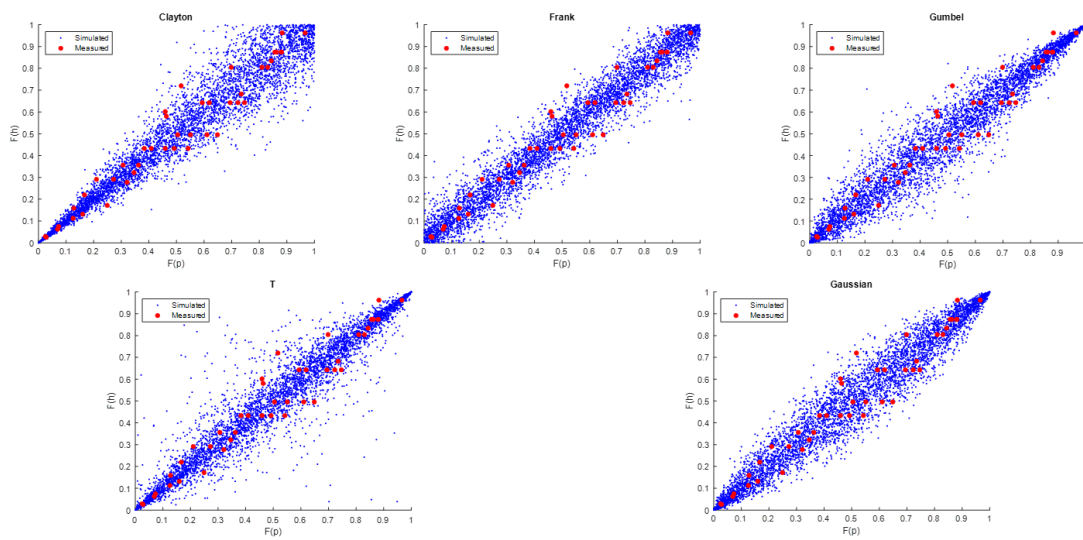


Figure 4-17 Scatterplots of joint probability for observed and simulated laboratory data for  $(H_{s,max}, \partial(P/\rho)/\partial x_{max})$ . The observed and simulated data are shown by the red and blue dots, respectively.

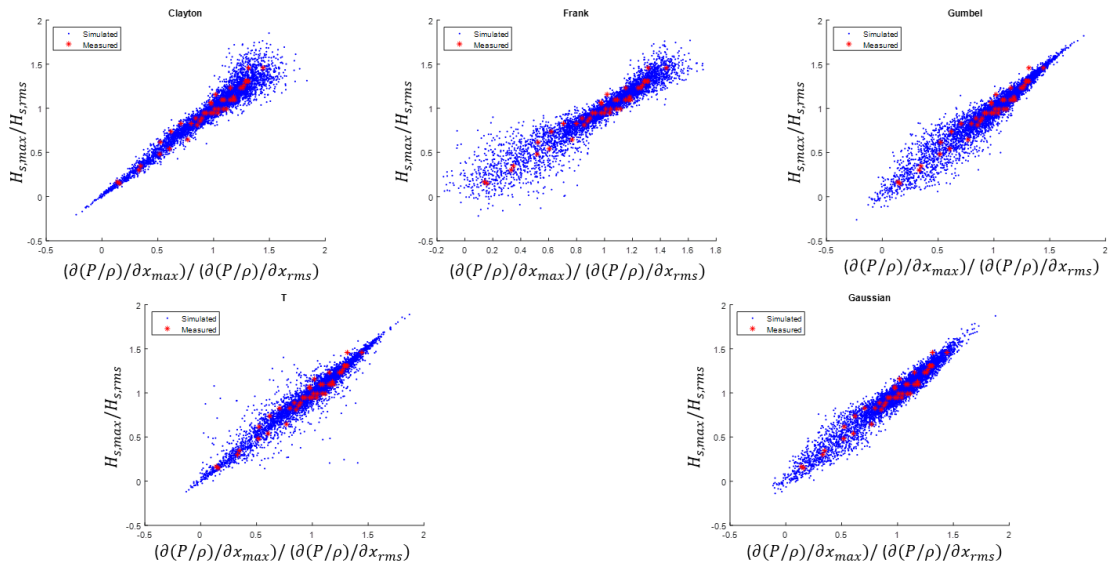


Figure 4-18 Scatterplots of observed and simulated laboratory data for  $(H_{s,max}, \partial(P/\rho)/\partial x_{max})$ . The observed and simulated data are shown by the red and blue dots, respectively.

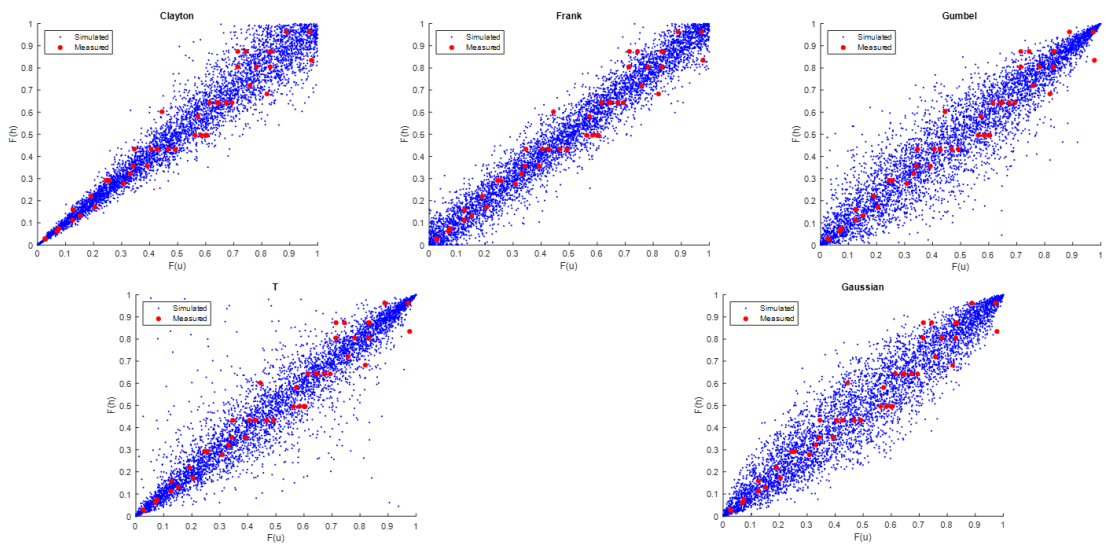


Figure 4-19 Scatterplots of joint probability for observed and simulated laboratory data for  $(H_{s,max}, \partial u/\partial t_{max})$ . The observed and simulated data are shown by the red and blue dots, respectively.

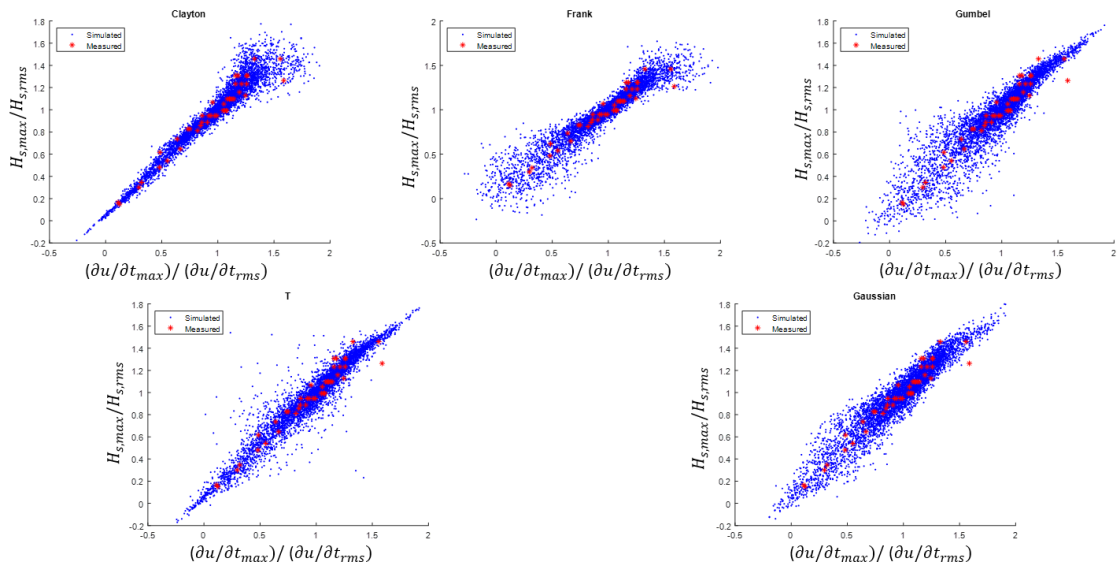


Figure 4-20 Scatterplots of observed and simulated laboratory data for  $(H_{s,max}, \partial u/\partial t_{max})$ . The observed and simulated data are shown by the red and blue dots, respectively.

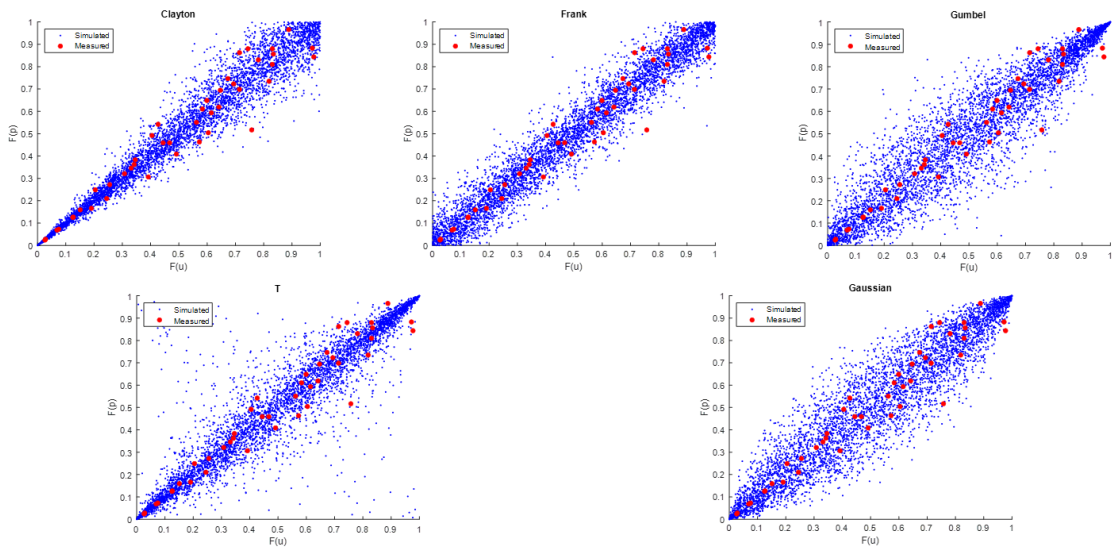


Figure 4-21 Scatterplots of joint probability for observed and simulated laboratory data for  $(\partial(P/\rho)/\partial x_{max}, \partial u/\partial t_{max})$ . The observed and simulated data are shown by the red and blue dots, respectively.

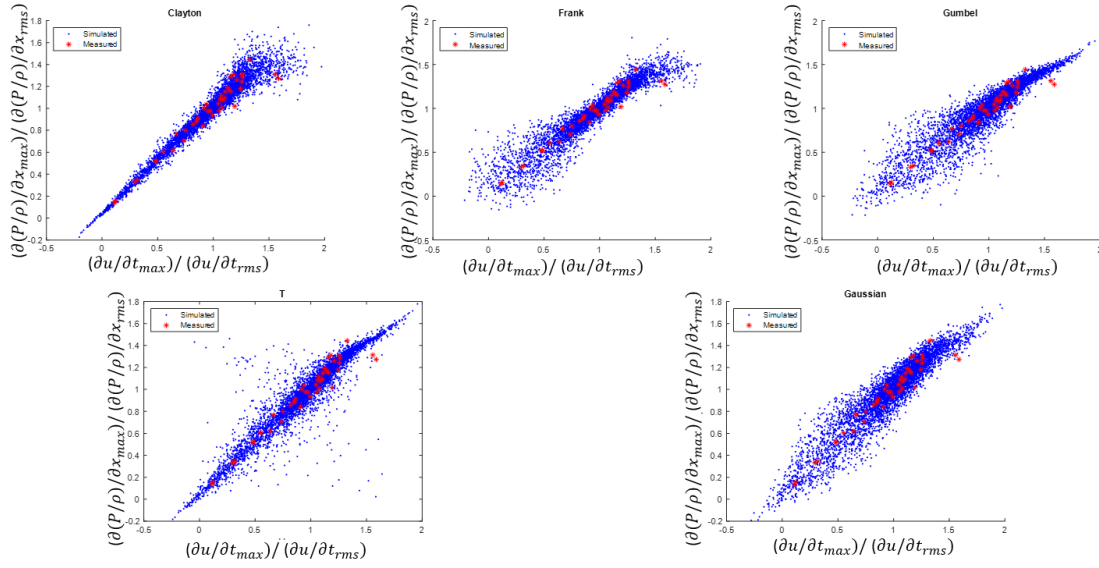


Figure 4-22 Scatterplots of observed and simulated laboratory data for  $(\partial(P/\rho)/\partial x_{max})/(\partial u/\partial t_{max})$ . The observed and simulated data are shown by the red and blue dots, respectively.

#### 4.9 Model application

Researchers who investigated pore water pressure gradients such as Suzuki et al. (2010) indicated that the correlation among the water surface, pore pressure gradient, and horizontal velocity should be investigated in future studies. The results of this study show that the pressure gradient and current acceleration can be estimated using the wave height. Some morphodynamic models such as those developed by Madsen (1974) and Sleath (1999) demonstrated that the pressure gradient over the bar can be considered an important parameter for suspending sediments and can cause a momentary failure of the bed. The pressure gradients estimated in this study can be used for the calculation of the Sleath number which can be defined as

$$S = \frac{dP/dx}{(\rho_s - \rho)g} \quad (23)$$

where  $\rho_s$  is the dry density of sediment,  $\rho$  is the density of fluid, and  $g$  is the gravitational acceleration. Commonly, the incipient motion of the sediment and

momentary bed failure is parameterized with the Shields number (Shields, 1936), which represents the non-dimensional bed shear stress of a single sand grain layer as

$$\theta = \frac{f_w U_m^2}{2(s-1)gd_{50}} \quad (24)$$

where  $f_w$  is the wave friction factor,  $U_m$  is the fluid velocity amplitude, and  $s$  is the sediment specific gravity. The friction factor can be calculated by a modified empirical equation proposed by Swart (1974) as follows

$$f_w = \exp\left(5.5\left(\frac{k_s}{A}\right)^{0.2} - 6.3\right) \quad (25)$$

where  $k_s$  is the grain roughness height and  $A = U_m T / 2\pi$ . Wilson (1989) showed a linear relationship between the sheet flow layer thickness and the maximum Shields parameter which can be written as follows

$$\frac{(\delta_s)_{max}}{d_{50}} = \Lambda \theta_{max} \quad (26)$$

where  $\Lambda$  is a proportionality constant. Mieras et al. (2017) found a wide range of values for  $\Lambda$  using very high accurate measured instantaneous sheet flow layer thicknesses. Since the momentary bed failure in the sheet flow is not the only related to the Shields number, as an attempt to reduce the range of  $\Lambda$ , Sleath number was added to the Shields number in this study. Therefore, Eq. (26) can be rearranged as

$$\frac{(\delta_s)_{max}}{d_{50}} = \Lambda(\theta_{max} + S). \quad (27)$$

Table 4-7 shows the hydrodynamic conditions and sheet flow thicknesses measured by Mieras et al. (2017). It was found that the range of values for  $\Lambda$  is

smaller for the modified equation, i.e., the range of  $\Lambda$  based on values presented in Table 4-7 for the cases with the involvement of the Sleath parameter is from 8 to 12 while the  $\Lambda$  values are between 19 and 31 based on Eq. 26. Thus, using the pressure gradient values estimated by the copula method and calculating the Sleath parameter, it seems more accurate sheet flow layer thicknesses can be obtained.

On the other hand, since there are several empirical equations proposed for the estimation of the Shields parameter, the results achieved by each equation should be different. Mieras et al. (2017) found a wide range for Shields parameter magnitudes using different proposed equations. That is due to the sensitivity of the Shields parameter equation to the estimation of the wave friction factor, fluid velocity amplitude and grain roughness. However, the correlation between the Sleath parameter and sheet flow thicknesses was assessed, in this study. A reasonable correlation between the Sleath parameter and the sheet flow thickness for the laboratory dataset was found. Figures (4-23) show the result of simulated sheet flow thicknesses using the Sleath parameter by the copula method. Using wave heights and pressure gradients obtained in this study, it is possible to achieve a reasonable estimation for the wave-induced sheet flow thickness.

*Table 4-7 Summary of wave, Shields, Sleath parameters, and sheet flow thickness*

$H_{bar}(m)$	$T(s)$	Shields parameter	Sleath parameter	Sheet flow thickness (mm)
0.54	5	1.04	0.13	5
0.63	5	1.37	0.14	5.2
0.73	5	1.77	0.16	7
0.87	5	2.42	0.19	6.5
0.59	7	1.18	0.13	7.9
0.66	7	1.44	0.15	8
0.75	7	1.81	0.18	9.4
0.84	7	2.22	0.19	9.9
0.97	7	2.87	0.20	14.5
0.49	9	0.82	0.09	4.3
0.63	9	1.28	0.14	8.5
0.77	9	1.84	0.15	13.1

The effect of the pressure gradient on momentary bed failure was investigated by Anderson et al. (2017), who analyzed the initiation of erosion as well as the magnitude of erosion depth. The importance of the pressure gradient on momentary bed failure was revealed in numerical simulations (Cheng et al., 2017). Cheng et al. (2017) emphasized the importance of the horizontal pressure gradient for bed instability. Almost all of the beach profile morphodynamic models are including the Shields parameter without the involvement of the Sleath parameter (and therefore the pressure gradient) in the sediment transport modules. The accurate estimation of sediment erosion and sandbar formation is a sort of challenging issue for these models. Since the bed failure is a function of both Sleath and Shields parameters (Cheng et al, 2017). A more accurate simulated beach profile can be expected by using the Sleath parameter. Thus, the results generated by the copula method should be useful for the statistical-process based morphodynamic models.

Wave induced local acceleration has been employed in various sediment transport equations. The simulated data using the copula approach can be useful for all of the abovementioned purposes. In future studies, this approach can be extended to other coastal parameters. In addition, the effect of sediment size on copula-based simulations can be considered for the future studies.

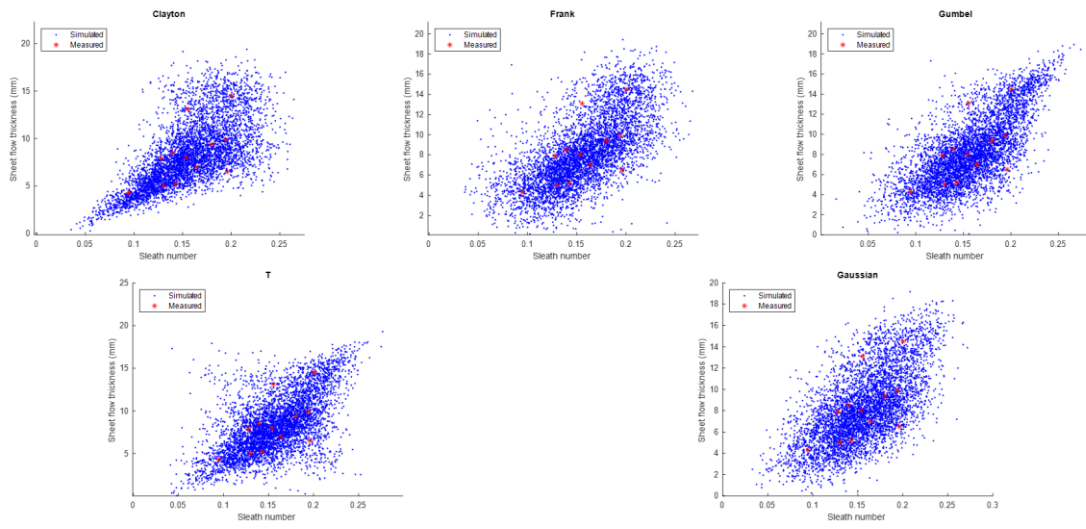


Figure 4-23 Scatterplots of observed and simulated laboratory data for Sleath number and sheet flow thickness. Observed and simulated data shown by red and blue dots, respectively.

## **5 Modeling of berm formation and erosion**

### **5.1 Introduction**

To predict berm formation and erosion, several numerical models have been developed and applied in many coasts in recent years. Many different complex processes from offshore to onshore should be considered when modeling sediment transport mechanisms and beach profile responses. Owing to these complexities, morphodynamic models generally cannot resolve morphodynamic processes explicitly. Therefore, most morphodynamic models cannot reproduce the results correctly under various wave conditions in different coastal regions. Nevertheless, researchers (e.g., Larson and Kraus 1989; Southgate and Nairn 1993; Roelvink et al. 2010; Kobayashi et al. 2008; Jayaratne et al. 2014; Tabasi et al. 2017) have continued their efforts to propose morphodynamic models to obtain reasonable results by improving hydrodynamic and morphodynamic calculations. The hydrodynamic and morphodynamic equations of these models include free parameters that should be calibrated for each specific site to achieve reasonable results.

In this study, a numerical model was used to predict berm formation and erosion under various wave conditions and timescales. The model simulates the evolution of the berm in connection to erosion and accretion based on different wave conditions. It is noteworthy that multiple simulations of berm formation and erosion in various locations with different wave conditions can offer a better judgment regarding the model performance. Therefore, a number of cross-shore beach profiles in the Caspian Sea were measured in different seasons of the year to validate the numerical model.

In the first section of this chapter, field measurements, their locations, and wave datasets for evaluating the performance of the proposed morphodynamic

model are described. The second section presents the fundamental governing equations for the calculation of the hydrodynamics and morphodynamics. The structure of the computer program for the model setup is provided in the third section. Section fourth summarizes the results of the model for different cross-shore beach profiles in the field studies. In addition, the model performance is compared with the field measurement results in this section.

## **5.2 Beach locations and data description**

### **5.2.1 Southern coast of Caspian Sea**

The southern coasts of the Caspian Sea located in Iran were selected for this study (Figure 5-1). The coastline stretches from 49°E to 59°E latitude for a distance of 820 km and is partitioned into three provinces. Furthermore, the southern coastlines of the Caspian Sea are primarily composed of sandy beaches. The cross-shore beach profiles considered in this study were those from Ataei et al. (2018). They reported that these profiles were predominantly composed of sediment, with the median grain size varying from 0.17 to 0.23 mm. Coastal regions with a significant distance in each province were selected for the field measurements. The coastal regions investigated were as follows:

- Astara and Dastak in the Guilan province
- Namakabrud, Mahmudabad and Larim in the Mazandaran province
- Miankaleh in the Golestan province

Cross-shore beach profiles were measured for each coastal region from 2013 to 2014. Although the profiles were measured from offshore to onshore, only the nearshore elevations of the measured profiles were required for modeling. In fact, the measurement of profiles in areas close to the shoreline should be easy as those areas are easily reachable, and the flow is extremely shallow. Nonetheless, compared with the offshore zone, the bed profile near the shore changed rapidly owing to the high gradient of the flow velocity and the sediment concentration in

the nearshore zone. Therefore, the frequency of the measurements in the nearshore region should be significantly higher compared to other regions.

Owing to insufficient measured filed data, a hindcast dataset comprising every-three-hour intervals was employed to obtain wave parameters such as significant wave height and mean period in the present study. The values of each wave parameter provided in the dataset were from 1998 to 2003, i.e., a five-year average of wave parameters was used in the simulation.

Figure 5-2 shows box plots of the hindcast wave height and the period for the abovementioned locations. The wave heights and periods corresponded to different periods of the year. Hence, the wave characteristics differed according to season. The whiskers above and below the boxes indicate the maximum and minimum values, respectively, of the wave height and period in the time histories of the datasets. The central marks on each box plot indicate the median, whereas the top and bottom edges of the boxes represent the 25th and 75th percentiles for each dataset, respectively.

The mean wave heights ranged from 0.7 to 1 m, whereas the wave periods ranged from 4.8 to 5.3 s. Additionally, 75% of the wave heights and periods were approximately below 1 m and 5.3 s, respectively. This reflects that both wave heights and periods are within a reasonable margin.

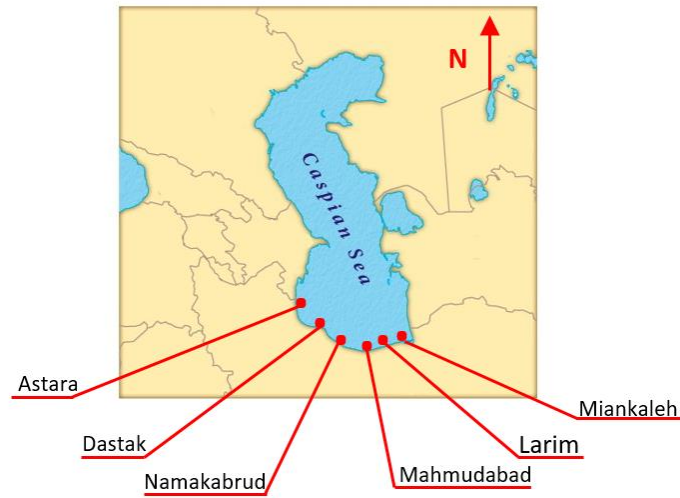


Figure 5-1 Locations of measured (field) beach profiles in the Caspian Sea (Iran).

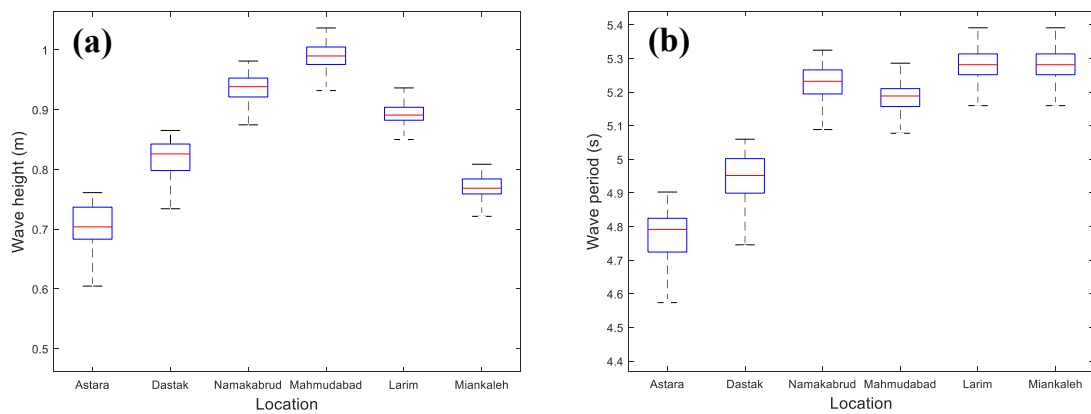


Figure 5-2 Wave condition for each coastal region of Caspian Sea; (a) significant wave height and (b) mean wave period.

## 5.2.2 Narrabeen-Collaroy beach

Narrabeen-Collaroy beach (hereafter referred to as Narrabeen) in Australia as a wave dominated embayed beach was selected for this study. The beach is located on the northern beaches of Sydney in New South Wales (Figure 5-3). The beach with about 3.6 km long stretches from Dee Why to Warriewood beaches. The shoreline has 25° clockwise orientation to the north (Short, 2007) and is mostly composed of medium-sized quartz sand grain with the median sand grain of 0.3-

0.4 mm (Short and Wright, 1981). Since 1971, the beach wave climate has been monitored by Sydney Fort Denison wave rider buoys. The measured wave datasets reveal that the beach is exposed to the moderate to high wave energy condition (Shore and Wright, 1981). However, the beach experience several types of cyclones within a year. The cyclones can be classified mainly into three types: mid-latitude cyclones crossing the Tasman Sea; Tropical cyclones that induce swell from the northeast within summer (Short and Trenaman, 1992); extra cyclones that generate swells from the east and southeast which are known as the most damaging cyclones in this region (Speer et al., 2009). These cyclones are also known as East coast lows (ECLs) which occur four to five times per year and the wave heights can reach more than 8 m.

According to the definition proposed by Callagan et al. (2008) for the storm indicates that events with  $H_s > 3$  m and more than one hour duration can be recognized as a storm event, Narrabeen is subjected to 12 storms in average each year. Figure () shows Subaerial Volume Index (SVI). The SVI describes the ratio of the differences between the average beach profile volume changes in a specific period and its corresponding standard-deviation as follows:

$$SVI(t) = 10 \frac{\left(\frac{1}{5} \sum V_i(t)\right) - V_a(t)}{std(V_a(t))} \quad (1)$$

where  $V$  is the volume through the profiles, index  $i$  indicates the number of profiles,  $V_a$  is the average of  $V$  at the time  $t$ . Positive values for SVI indicate beach accretion while negative values show beach profile erosion. Although huge amount of erosion was observed in different periods (e.g., between 2008 and 2009), the data restates that the beach is relatively stable in the long-term.

Since April 1976, cross-shore beach profiles have been measured monthly by the University of Sydney at five locations across the beach which are marked in Figure 5-4. A simple beach profile measurement method proposed by Emery

(1961) was employed until the year 2006. The cross-shore beach profiles were measured with 10 m cross-shore intervals from the benchmarks at the back of the beach to the mean sea level. However, due to the measurement errors founded by Harley et al. (2006), a high accuracy RTK-GPS method with the approximate error of  $\pm 0.03$  m and 1 m cross-shore resolution has been employed after. Additionally, based on Holm and Stanley (2007), another survey method (ARGUS coastal imaging station) has been used since August 2004 in order to record high frequency coastal parameters.

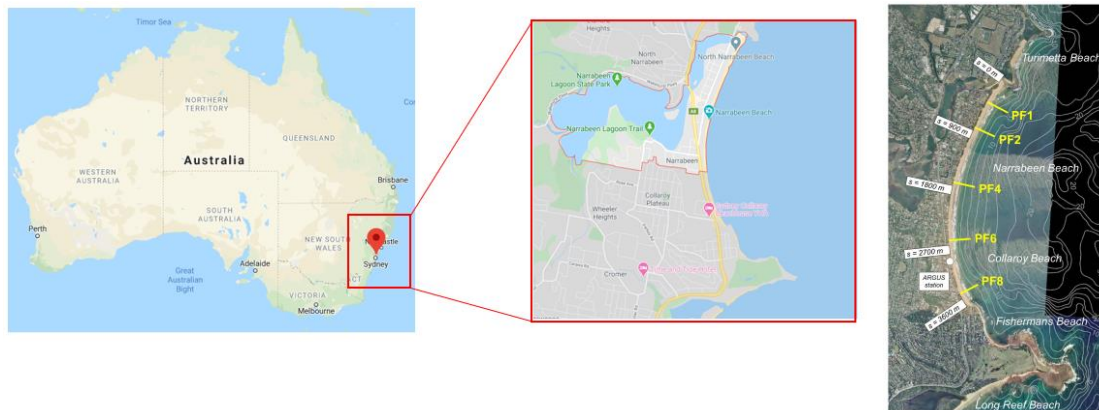


Figure 5-3 Narrabeen and cross-shore beach profile locations

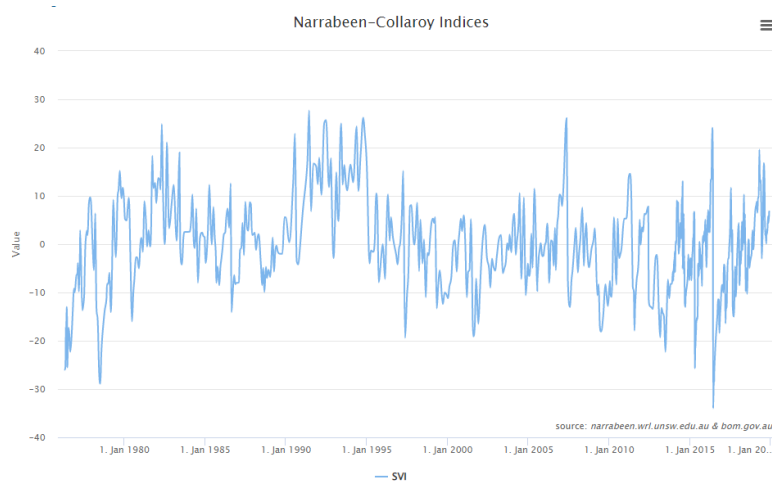


Figure 5-4 SVI values for Narrabeen

### 5.3 Model description

The coastal area based on the spatial scale of the cross-shore can be divided into three main regions: offshore, surf zone, and swash zone. Cross-shore sediment transport models assume the long-shore sediment transport to be negligible. Therefore, cross-shore models determine bed level changes per meter of coastline. Across these main coastal areas, several model formulations have been proposed to predict the amount of sediment transport. Generally, proposed sediment transport equations are valid for a specific cross-shore area and the equations are not able to cover the sediment transport calculations from the offshore to the onshore. Depending on the nature of coastal areas, timescales, hydrodynamic, and morphodynamic conditions, each of the modeling approaches provides different results. Therefore, morphodynamic models should be calibrated based on the abovementioned conditions.

Several studies regarding berm formation and erosion have been published. In some research studies, berm formation and erosion were investigated qualitatively as well as quantitatively (e.g., Duncan 1964; Strahler 1966; Thomas and Baba 1986; Larson et al. 2004). Meanwhile, some researchers have proposed various empirical relationships between wave conditions and berm characteristics (e.g., Bagnold 1940; Bendixen et al. 2013). To simulate the effects of various wave conditions on beach morphology, numerous numerical morphodynamic models have been developed and formulated with various levels of complexity. Generally, morphodynamic models determine bed-level changes in association with the quantification of volumetric sediment transport. The model formulation can be classified into analytical, behavioral, empirical, semi-empirical, and process-based categories.

This study focused on predicting cross-shore beach profile changes in the swash zone. An empirical cross-shore sediment transport model proposed by Suzuki and Kuriyama (2008) was applied for this study. The empirical sediment

transport equations were derived based on sediment transport measurements at Hasaki Oceanographical Research Station (HORS) where is a coastal research facility in Japan. Further information regarding HORS can be found in (ref). The model was designed to estimate the cross-shore sediment transport by calculating the rate of sediment erosion and accretion, separately. The model was also tested at the southern coasts of the Caspian Sea (Tabasi et al. 2020). The sediment transport equations for the sediment erosion and accretion are described below.

To investigate the correlation between hydrodynamic parameters and morphological changes, different thresholds for berm formation and erosion have been proposed. Larson and Kraus (1989) utilized data from Japanese, American, and Canadian beaches for the classification of erosion and accretion events. They hypothesized a relationship between sand fall velocity and wave characteristics. Similarly, Wright and Short (1984) proposed a dimensionless fall velocity parameter using data from three years of observation at 26 beaches around Australia. Furthermore, they classified beaches into dissipative, intermediate, and reflective based on a dimensionless fall velocity. Flatter profiles tend to be formed as dissipative beaches by high energy wave conditions, whereas steeper profiles with a greater amount of sand volume tend to form as reflective beaches. In this study, the model comprised different berm formation and erosion sub-modules based on wave run-up to estimate the sediment transport rate. If the wave run-up reaches the top of the berm, then berm erosion will occur. Otherwise, the berm will form and further develop (Figure 5-5).

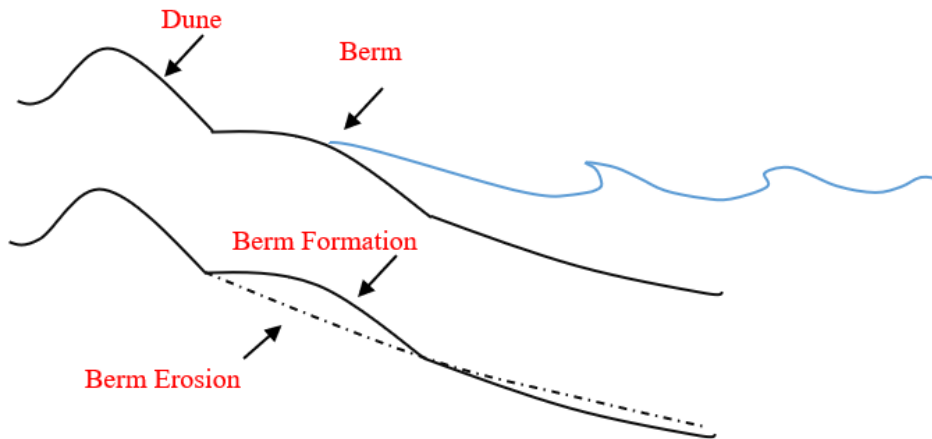


Figure 5-5 Schematic diagram of berm formation and erosion

### 5.3.1 Berm formation

To manage coastal zones, the formation and evolution of berm accretion processes must be predicted. Generally, berm forms after a storm event (beach recovery) and in seasonal variable conditions. However, the simulation of berm formation in numerical models has not been achieved at a high degree of accuracy owing to the deficient understanding of associated highly complex processes, such as the different characteristics of waves, currents, and morphologies.

Numerous studies that involve the physics of berm formation have been conducted. Hine (1979) presented a comprehensive study regarding berm formation and classified berm formation processes into three different mechanisms based on hydrodynamic and morphodynamic characteristics. Weir et al. (2006) added two more modes of berm formation to Hine's theory. Sunamura and Horikawa (1974) proposed a threshold by considering the median grain size ( $D_{50}$ ) for berm formation. Jensen et al. (2009) performed a study to identify the main factor controlling berm formation on gentle slope beaches.

In this study, for the modeling berm formation, the foreshore was partitioned into two zones. The offshore boundary was defined at the shoreline location and set as  $x/X = 1$ , where  $x$  and  $X$  are the cross-shore position and

distance between boundaries, respectively. Furthermore, the onshore boundary was defined at the cross-shore location of the maximum wave run-up elevation and set as  $x/X = 0$ . The boundary between the lower and upper zones was defined as  $x/X = 0.7$  (Figure 5-6).

The sediment transport rate tended to increase gradually from  $x/X = 0$  to 0.7 in the form of a quadratic relationship. Meanwhile, the rates from  $x/X = 0.7$  to 1 were assumed to be constant. The sediment transport rate at  $x/X = 0.7$  is expressed as shown in Eq. (3).

$$Q_{f_{0.7}} = 1.15 \times 10^{-7} E_f + 0.49. \quad (3)$$

The offshore energy flux is expressed as  $E_f = \frac{1}{16} \rho g (H_{1/3})^2 C_g$ , where  $\rho$  is the seawater density,  $g$  the gravitational acceleration,  $H_{1/3}$  the significant wave height, and  $C_g$  the group velocity.

### 5.3.2 Berm erosion

In this study, for the berm erosion cases, the model partitioned the foreshore into three distinct zones (Figure 5-6). The sediment transport rate increased from  $x/X = 0$  to 0.15 and decreased from  $x/X = 0.15$  to 0.7.

$$\begin{cases} Q_{e_{0.15}} = 2.06B_h - 0.29 \\ Q_{e_{0.7}} = -3.07B_h - 1.17 \end{cases} \quad (4)$$

where  $Q_{e_{0.15}}$  and  $Q_{e_{0.7}}$  are the sediment transport rates for berm erosion at  $x/X = 0.15$  and  $x/X = 0.7$ , respectively, and  $B_h$  is the berm height. The free parameters included in the sediment transport equations for both berm formation and erosion conditions can be calibrated based on the characteristics of the sites.

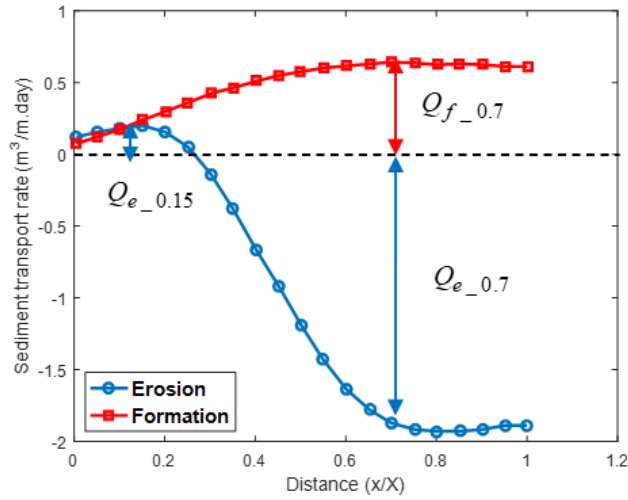


Figure 5-6 Sediment transport rate by Suzuki and Mochizuki (2014).

#### 5.4 Model setup

A computer program was written in MATLAB to simulate berm formation and erosion. The model grids had a constant cell spacing of  $dx = 1\text{ m}$  and  $-m$  for the Caspian Sea and Narrabeen, respectively. The model can be used for irregular waves for the full duration of modeling. The bed level changed owing to the spatial gradient of cross-shore sediment transport. Therefore, the model was sensitive to the free parameters included in the sediment transport equations. In other words, to simulate the bed level changes accurately, the free parameters of the sediment transport equations should be optimized via trial and error during the calibration process. Measured cross-shore profiles, offshore wave heights, and water levels were defined as the inputs to the program. The program comprised three tiers for the calculation of beach profile changes, as follows:

1. The offshore energy flux was calculated and the wave run-up levels estimated;
2. Erosion/formation was determined, and related relationships (Eqs. 3 or 4) were employed for the sediment transport rate calculations;
3. Beach profile updated using sediment mass conservation equation.

In this computer program, waves were classified into destructive and constructive types based on the wave run-up threshold; subsequently, seaward and landward sediment transport fluxes were estimated using the distinct modules.

## 5.5 Results

This study focused on berm formation and erosion at the southern coasts of the Caspian Sea and Narrabeen. The results of the field sites justified the performance and reliability of the numerical model. The Brier skill score (BSS) is a useful method for evaluating model performance. The BSS has been widely applied in beach profile modeling by Splinter et al. (2014), Berard et al. (2017), and Tabasi et al. (2018). The BSS applied to the prediction of beach erosion and formation can be expressed as follows:

$$BSS = 1 - \frac{\sum(|Z_m - Z_s|)^2}{\sum(|Z_m - Z_i|)^2} \quad (5)$$

where  $Z_m$  is the bed elevation after erosion and formation,  $Z_s$  the final simulated bed elevation, and  $Z_i$  the initial bed level. Using BSS values, Van Rijn et al. (2003) categorized the performance of coastal morphodynamic models, as listed in Table 5-1. A BSS value approaching 1 indicates better model performances compared with lower values. The BSS values revealed that the model agreed well with the field measurements for both berm formation and erosion conditions.

*Table 5-1 Classification of Brier Skill Score (BSS) by Van Rijn et al. (2003)*

Score	Bad	Poor	Fair	Good	Excellent
Classification	<0	0–0.3	0.3–0.6	0.6–0.8	0.8–1.0

### 5.5.1 Caspian Sea

The erosional conditions for the Mahmudabad and Namakabrud beach profiles were dominant during the periods July 6–November 6, 2013, and November 25, 2013–January 8, 2014, respectively. Meanwhile, berm formation was the most effective during the periods May 6–October 19 and June 29–November 1, 2013; December 21, 2013–January 13, 2014; and October 12, 2013–January 16, 2014, at Miankaleh, Larim, Dastak, and Astara beaches, respectively. The durations of model simulations and wave characteristics for each site are summarized in Table 5-2.

*Table 5-2 Duration of model simulation and wave parameters for selected beach*

Beach	Mahmudabad	Namakabrud	Miankaleh	Larim	Dastak	Astara
Duration of Simulation (days)	123	44	166	125	23	96
Mean Wave Height (m)	0.71	0.80	0.64	0.71	0.71	0.62
Mean Wave Period (s)	4.85	4.95	4.50	4.80	4.65	4.77
Mean Wave Direction (°)	192.5	87.6	293.0	250.0	93.0	77.0

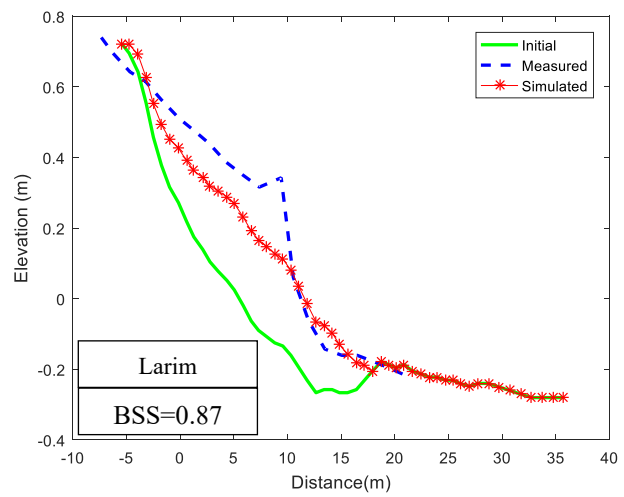
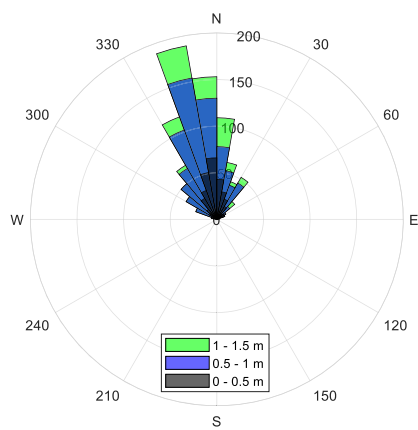
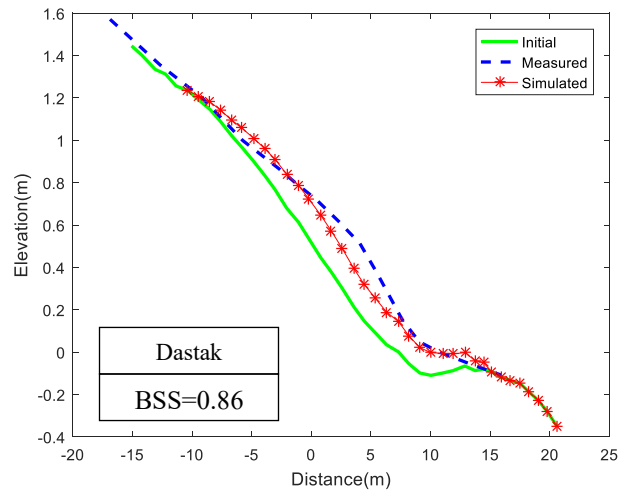
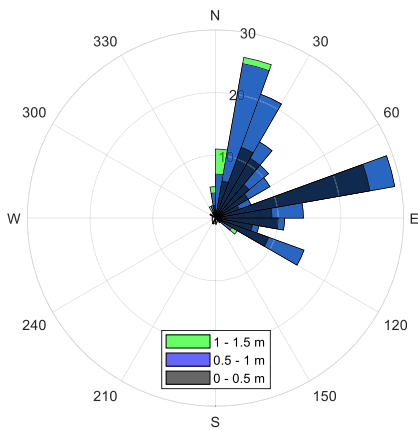
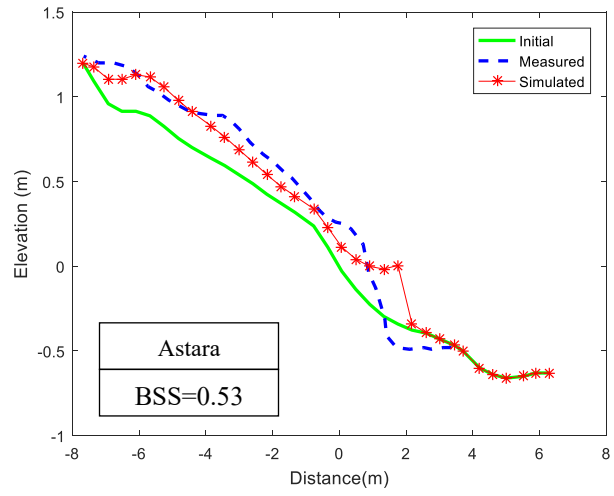
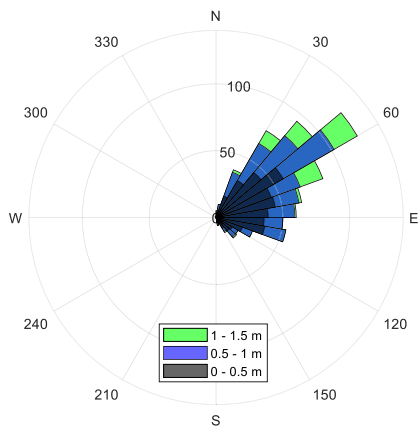
As shown in Table 5-2, the model incorporates the ability for onshore and offshore sediment transport with beach profile predictions ranging from short to medium time scales. As an example, for berm formation modeling, the model demonstrated high performance in simulating the Dastak profile in 23 days as well as the Miankaleh profile in 166 days. However, the duration of simulation for berm formation is expected to be relatively longer than that for berm erosion.

The net sediment transport rates for the Miankaleh, Larim, Dastak, and Astara beaches during the study were primarily landward, and berm formation occurred continuously across the beach profile (Figure 5-7). Although berm was formed in the Miankaleh, Larim, Dastak, and Astara profiles, the net sediment transport rates were not completely landward, and the direction of sediment transport shifted between onshore and offshore based on the wave conditions.

Therefore, berm erosion/formation couplet patterns frequently appeared during the measurements. Similarly, in the Mahmudabad and Namakabrud profiles (Figure 5-8), the sediment transport was primarily seaward and erosion occurred; however, berm erosion/formation couplet patterns appeared during the model simulation.

The calculated BSS values are shown in Figures 5-7 and 5-8. As depicted in Figure 5-7, the model performance was excellent for all the berm formation cases except that of Astar. In addition, the BSS values in Fig. 6 show that the model performance was excellent and good for the Nakamabrud and Mahmudabad cases, respectively. The average BSS values for berm formation and erosion were 0.80 and 0.77, respectively. These values signified satisfactory performances for both the berm formation and erosion cases. Meanwhile, as no significant difference was observed between the average BSS values, it was difficult to judge the case in which the model performed better.

Finally, the accurate prediction of the sediment transport rate is crucial for simulating beach profile changes. The sediment transport rate relationships comprise the wave energy flux, berm height, and numerical (free) constants. They can be fitted with the field observations using a time series of wave characteristics with daily intervals and by changing the numerical constants.



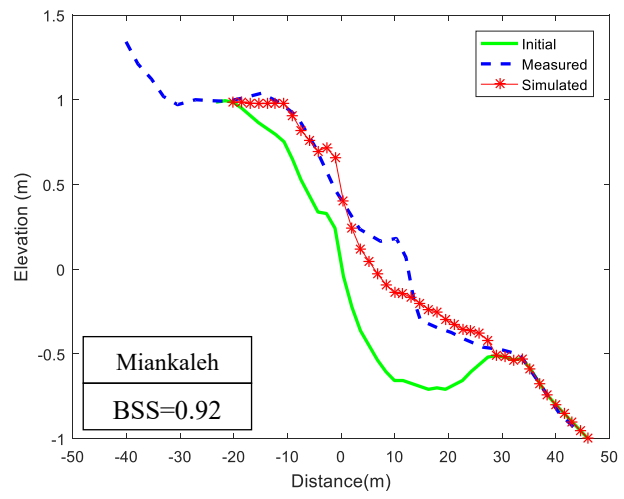
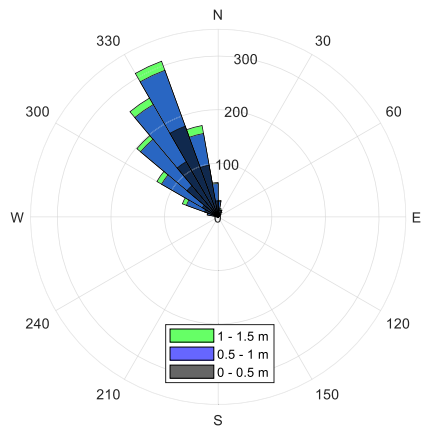
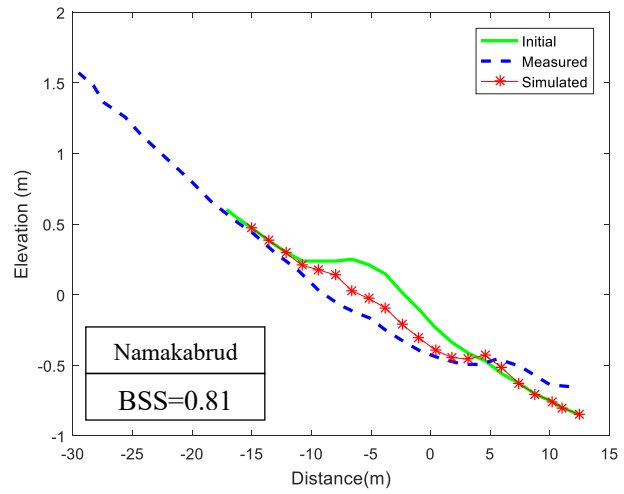
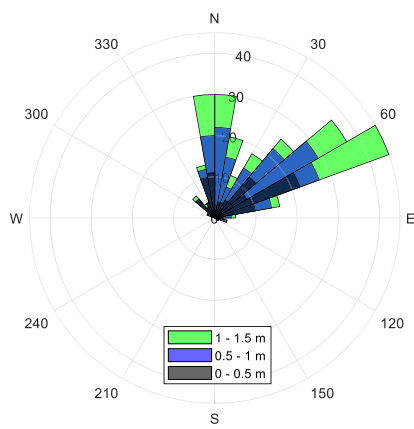


Figure 5-7 Right panels: Evolution of berm formation in Astara (a), Dastak (b), Larim (c), and Miankaleh (d) for measured (blue dashed line) and simulated beach profiles (red asterisk line). Green lines represent initial beach profiles. Left panels: Hindcast wave rose.



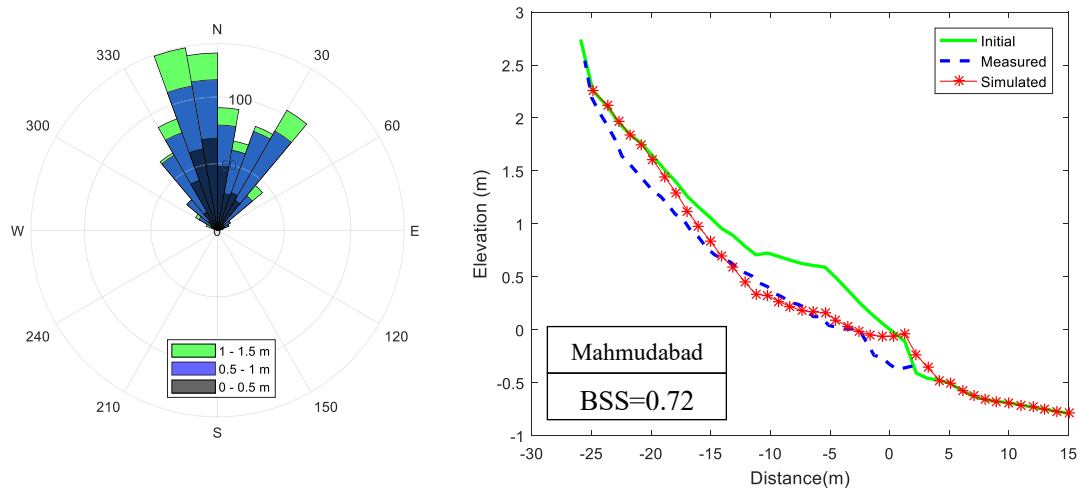


Figure 5-8 Right panels: Evolution of berm erosion in Namakabrud (a) and Mahmudabad (b) for measured (blue dashed line) and simulated beach profiles (red asterisk line). Green lines represent initial beach profiles. Left panels: Hindcast wave rose.

## 5.5.2 Narrabeen

Cross-shore beach profiles have been measured at five locations along the shoreline. Harley et al. (2009) concluded that cross-shore sediment transport is the dominant morphodynamic mechanism in this beach and Narrabeen is a sort of offshore-onshore sediment transport beach. However, since the model can only estimate the cross-shore sediment transport, the central cross-shore profiles (PF4) were selected in this study to minimize the effect of any possible longshore sediment transport. Narrabeen experienced very significant erosion due to storms. For example, a serious erosion was reported by Harley et al. (2009) during late 2008 and early 2009. However, Narrabeen can be categorized as a beach with inter annual cycles of erosion and accretion.

The selected modeling periods were chosen between 2010 to 2014. Since the beach profile survey has been conducted with monthly intervals, monthly simulations were considered as the main objective in the beginning of this study. Then, the simulations were conducted for different periods from two to six-month simulations. Empirical equations in the morphodynamic models are the main

components of the model prediction uncertainties. Nevertheless, most empirical equations are composed of several free parameters which can be used to minimize discrepancies between simulation results and actual data. Trial and error method is the most common method to complete the model calibration process. However, a physical meaning exists behind of many parameters that should be realized before starting calibration procedure to achieve optimal parameters within few numbers of trials. The importance of this issue more significant for the calibration of morphodynamic models with the large number of free parameters. In the present model, sediment transport equations and criteria for erosion and accretion should be calibrated mainly.

### 5.5.2.1 Sediment transport calibration

Since the sediment transport equations were proposed based on HORS datasets, the results achieved by the model using the original free parameters exhibited inadequate model skill. The median grain size of sediment in Narrabeen is coarser than Hasaki. It is a significant morphological difference between these two coastal areas. The sediment grain size affects various sediment transport parameters such as sediment fall velocity, local sediment concentration, bedload and suspended load rate. In the same hydrodynamic condition, less sediment transport rate for the coastal area with larger sediment size can be expected. Thus, free parameters of the sediment transport equations were decreased as follows:

$$\begin{cases} Q_{e_{0.15}} = 1.24B_h - 0.17 \\ Q_{e_{0.7}} = -1.84B_h - 0.7 \end{cases} \quad (6)$$

$$Q_{f_{0.7}} = 0.57 \times 10^{-7} E_f + 0.25 \quad (7)$$

### 5.5.2.2 Criteria for distinguishing erosion and accretion

As the sediment particles are moved by the hydrodynamic forces, morphological features such as surf zone sandbars and swash zone berms form and

erode consistently. In other words, coastal zones react to the fluid motion accordingly. For realistic prediction of sediment transport direction, there is a need to identify the influence of waves on the beach shape. Several criteria for predicting the direction of net sediment transport exist (e.g., Dean 1973; Sunamura and Horikawa 1974; Sunamura 1980; Larson and Kraus 1989). Almost all criteria have been derived from experimental or/and field datasets empirically. The sediment transport direction has been distinguished by a line that separates accretive and erosive and erosive waves. However, several hydrodynamic and morphodynamic parameters have involvement in both erosion and accretion processes. Thus, due to lack of knowledge regarding the involvement of complex morphodynamic processes, the accurate simulation of morphological changes is still sophisticated. To predict erosion or accretion events, distinguishing criteria for sediment transport direction can be helpful. Several methods are available for distinguishing the sediment transport direction as follows.

#### **5.5.2.2.1 Sediment transport threshold**

Sediment transport thresholds are mostly based on the initiation of sediment particle movement. Several sediment transport thresholds have been proposed. For example, Henderson (1966) proposed a diagram based on Shields parameter for defining a sediment transport threshold. Almeida et al (2011) developed a sediment transport threshold based on morphological changes at Faro beach using wave height. The methodology is composed of five steps based on cross-shore processes using the definition of the profile active zone, cross-shore sectors, volumetric changes, vertical variability and finally the threshold of sediment transport using wave height and profile vertical variability. The relationship between the significant wave height at the 99th percentile ( $H_{s99}$ ) and the maximum vertical variation ( $MVV$ ) for each sector is as follows:

$$\begin{cases} MVV_A = 0.1712H_{s99} \\ MVV_B = 0.0916H_{s99} \\ MVV_C = 0.0635H_{s99} \\ MVV_D = 0.0488H_{s99} \end{cases} \quad (8)$$

where sectors, A, B, C, and D represent waves higher than 2.3, 3.2, and 4.1 m, respectively.

#### 5.5.2.2.2 Dominant parameters for sediment transport direction

In several studies a single parameter such as the Ursell parameter (Ursell, 1953) has been chosen for investigating the direction of sediment transport. The Ursell parameter is composed of the wave height (H), the wavelength (L), and the water depth (h) as follows:

$$U = \frac{HL^2}{h^3} \quad (9)$$

Nishimura and Sunamura (1986) used the Ursell number and the Hallermeier parameter for defining the sediment transport direction as follows:

$$\phi = \frac{U_b^2}{(s-1)gd_{50}} \quad (10)$$

where  $U_b = \frac{a\pi}{T}$  is the wave orbital velocity amplitude,  $a$  is the near bottom orbital diameter. The direction of sediment transport can be recognized based on the following statement.

- If  $U > 230$ , net sediment transport occurs
- If  $\frac{7000}{U} < \phi < 0.13U$ , onshore sediment transport occurs
- If  $\phi > 0.13U$ , offshore sediment transport occurs

### 5.5.2.2.3 Equilibrium beach profile

The equilibrium beach profile concept was proposed by Brunn (1954) and it has been used as a fundamental assumption in many beach morphological change models such as Edleman (1972), Inman et al. (1975), Dean and Maurmeyer (1983), Dean and Dalrymple (1985). According to equilibrium beach profile concept, the beach profile remains in its equilibrium state without a significant shape change (Larson and Kraus, 1989). This assumption is reasonable for the long term morphological change scale. In other words, the beach consistently will erode until reach to its equilibrium profile during a storm event.

### 5.5.2.2.4 Fall velocity

Fall velocity plays a significant role in many morphological models based on the force balance between the hydrodynamic forces and sand grain gravity force. The fall velocity can be represented as

$$\omega = \sqrt{\frac{4(\rho_s - \rho)gd_{50}}{3\rho C_D}} \quad (11)$$

where  $\rho_s$  is the density of sand grain,  $\rho$  is the fluid density, and  $C_D$  is the drag coefficient that depends on Reynolds number. Bagnold (1963) suggested that the fall velocity can be used as a factor to illustrate sediment suspension and consequently sediment movement to the offshore. Komar (1998) proposed that horizontal wave orbital velocity ( $U_b$ ), bed slope ( $S$ ), and fall velocity are related to sediment suspension and sediment movement direction. When  $\omega < U_b S$  sediments tend to be suspended and move to the offshore. It was similar to the research work conducted by Dean (1983) to propose a relationship between fall velocity, water depth, wave period and a friction factor ( $\delta$ ) as follows

$$\omega < \frac{\delta h}{T} \quad (12)$$

According to this equation if  $\frac{\delta h}{T}$  is greater than the fall velocity, the sediment will suspend and probably move to the offshore.

#### 5.5.2.2.5 Line separation

Separation of sediment transport direction using a line is the most well-known and common method chose in several study. Most of the proposed lines are derived based on laboratory experiment under monochromatic waves. It can make inaccurate results under various irregular wave conditions. This method was selected for this study. In the beginning, the equation proposed by Sunamura (1980) was evaluated for Narrabeen. Figure (5-9) shows the scatterplot of the calculated values based on different wave conditions using Sunamura's (1980) approach. The results were categorized based on eroded or formed beach profile.

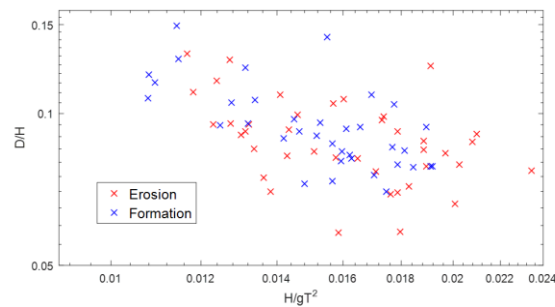


Figure 5-9 Calculated wave criterion values based on Sunamura (1980).

As it is obvious from figure (5-9), defining a line to separate the accretion and erosion events is not possible for this dataset. This sort of error to distinguish erosion and accretion event was investigated by Jackson (1999). Jockson (1999)

tested the validity of several line separation approaches proposed by different researchers using field dataset achieved in Delaware Bay. The result of this investigation did not reveal good performance of the line separation approaches to predict the direction of sediment transport.

Figure (5-10) shows the calculated accretion-erosion criterion values based on Larson and Kraus (1989). This criterion includes the sediment fall velocity as well as offshore wave characteristics. This criterion could not separate accretion and erosion events very accurately. Among line separation approaches, one-parameter criteria due to ease of calculation and application can be more helpful to separate sediment transport direction for applying in numerical sediment transport models.

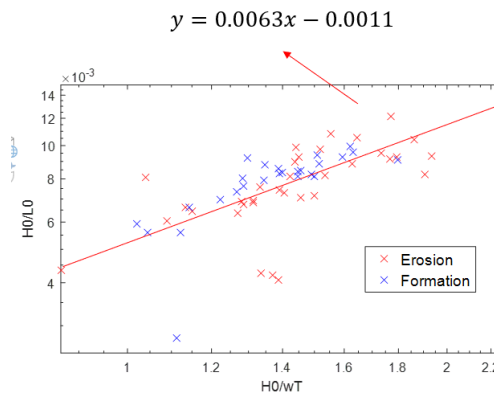


Figure 5-10 Calculated wave criterion values based on Larson and Kraus (1989).

Johnson (1949) emphasized on the importance of the wave steepness parameter ( $H/\omega T$ ) in distinguishing the sediment transport direction. Therefore, in this study the dimensionless sediment grain fall velocity as a one-parameter criterion containing wave asymmetry as well as sediment characteristic was selected to distinguish the direction of sediment transport. Several values have been suggested for this criterion.

Kraus et al (1991) suggested that when  $H/\omega T$  is approximately larger than 1.4 erosion happens. In this equation,  $H$  is the wave height,  $\omega$  is the sediment particle fall velocity, and  $T$  is the wave period. Conversely, accretion is expected when  $H/\omega T$  is less than 1.4. Similarly, Wright and Short (1984) proposed that values larger than 6 form sandbars and values less than 1 create berms. Values between 1 to 6 can also cause mixed bar and berms.

The sediment transport direction criterion was selected as one of the calibration parameters in the model. Generally, calibration parameters are necessary and important for obtaining accurate results and significantly affect the simulation results. Using calibration procedure, the simulation results can be adjusted to the measurements. In this model sediment transport equations and the criterion for distinguishing the sediment transport direction were calibrated. The model performance is very sensitive to the criterion for distinguishing the sediment transport direction. Y axis in figures (5-11) shows the values were selected for the criterion to achieve good results for the erosional and accretional cases separately. The values were achieved using trial and error method. The average of  $H/\omega T$  for the corresponding simulation periods represent good correlation between values selected for modeling and their average. Therefore, it can be concluded that the average values of  $H/\omega T$  are appropriate for starting the trial-and-error procedure.

### **5.5.2.3 Monthly simulation**

Simulation procedure was started based on the monthly simulation of the beach profile changes. The last four-year available datasets were selected for the simulation. In other words, the simulation period starts from 2010 to 2013. From the mid of January to the mid of February the coastline was under storm condition (Figure 5-12). Therefore, a severe erosion occurred during this period. Within September the wave condition was under storm. Blue color in this figure indicates that no simulation was conducted within that period. Figures 5-13 show the result

of simulations and their comparison with the measured profiles. Similarly, Figure 5-14 to 5-18 show the wave conditions as well as simulation results.

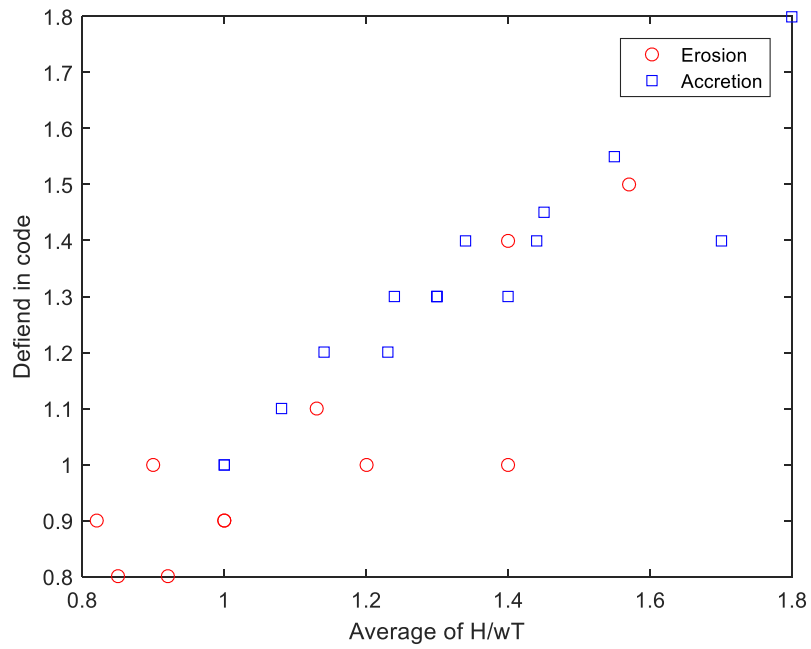


Figure 5-11 Sediment erosion and accretion separation values defined in model.

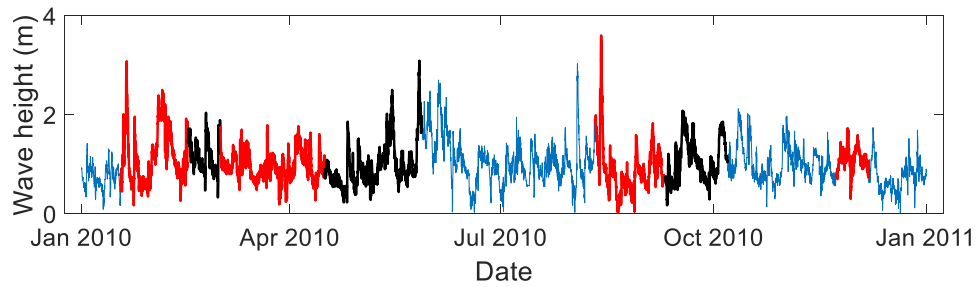


Figure 5-12 Wave height condition for 2010.

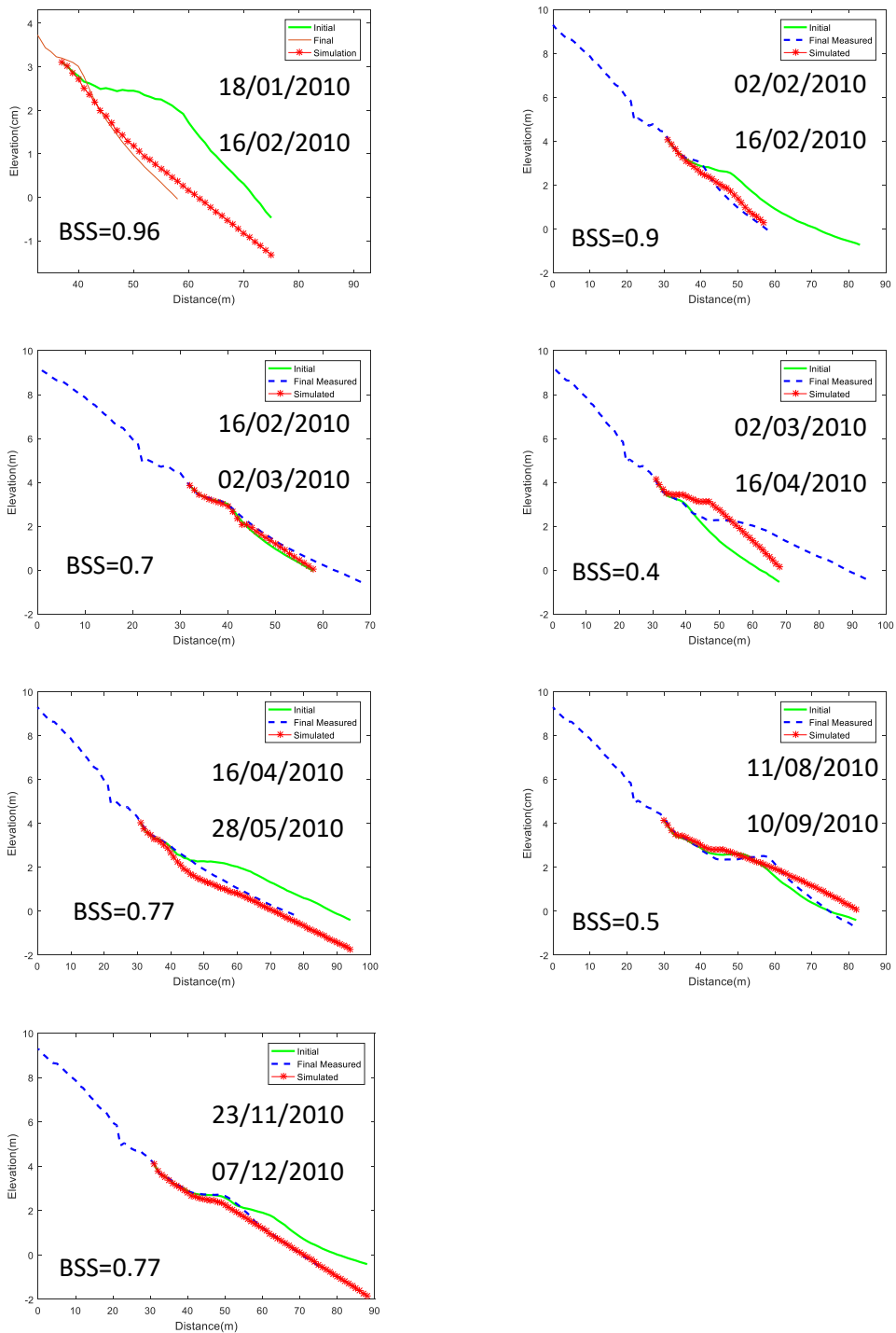


Figure 5-13 Monthly beach profile simulation results for 2010.

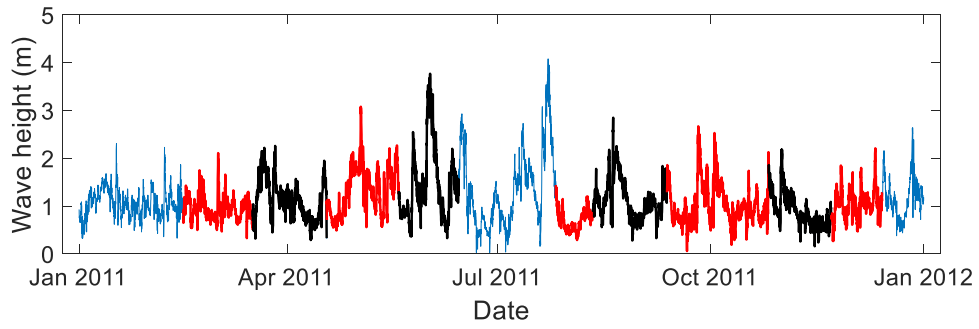


Figure 5-14 Wave height condition for 2011.

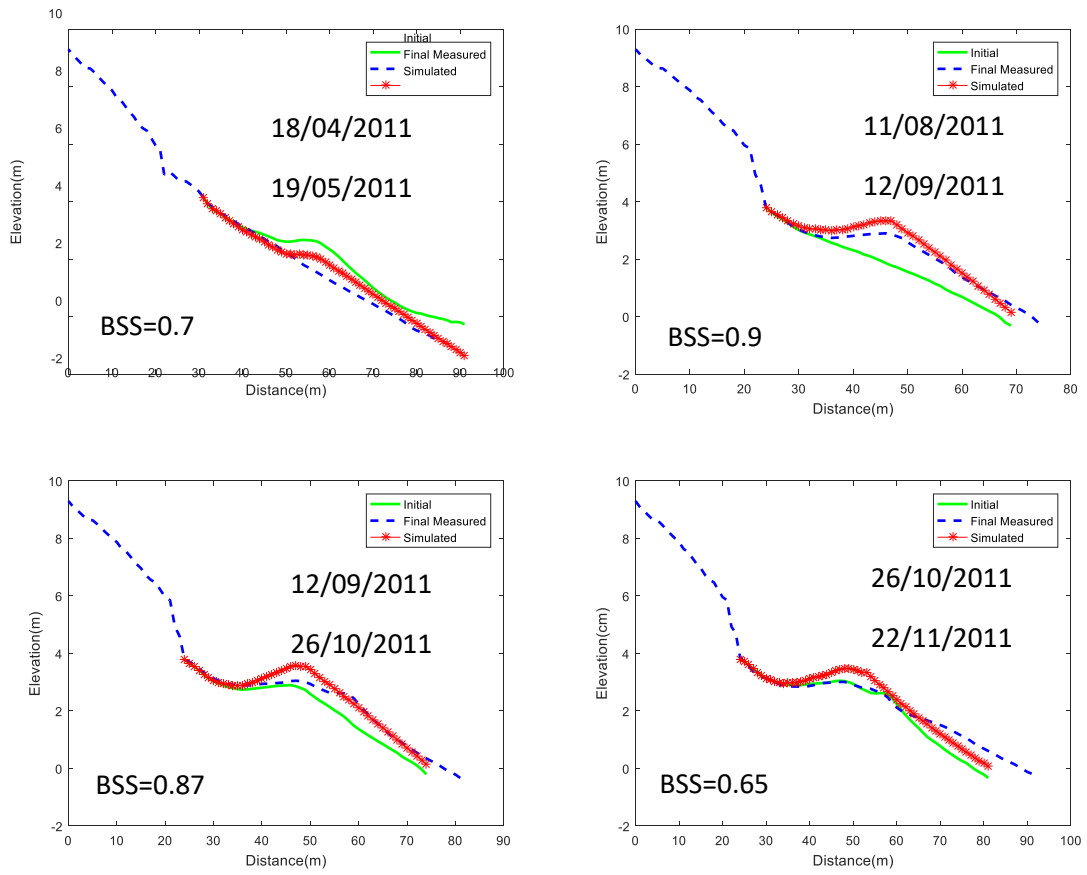


Figure 5-15 Monthly beach profile simulation results for 2011.

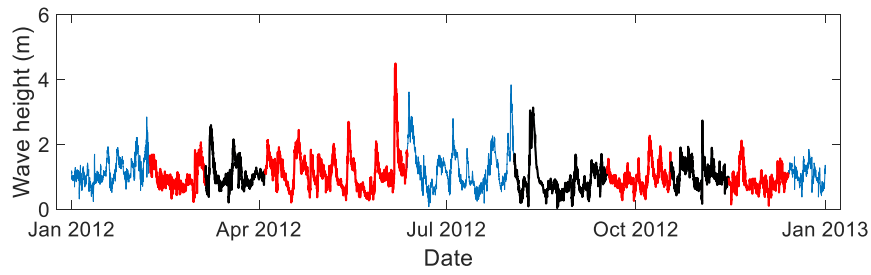


Figure 5-16 Wave height condition for 2012.

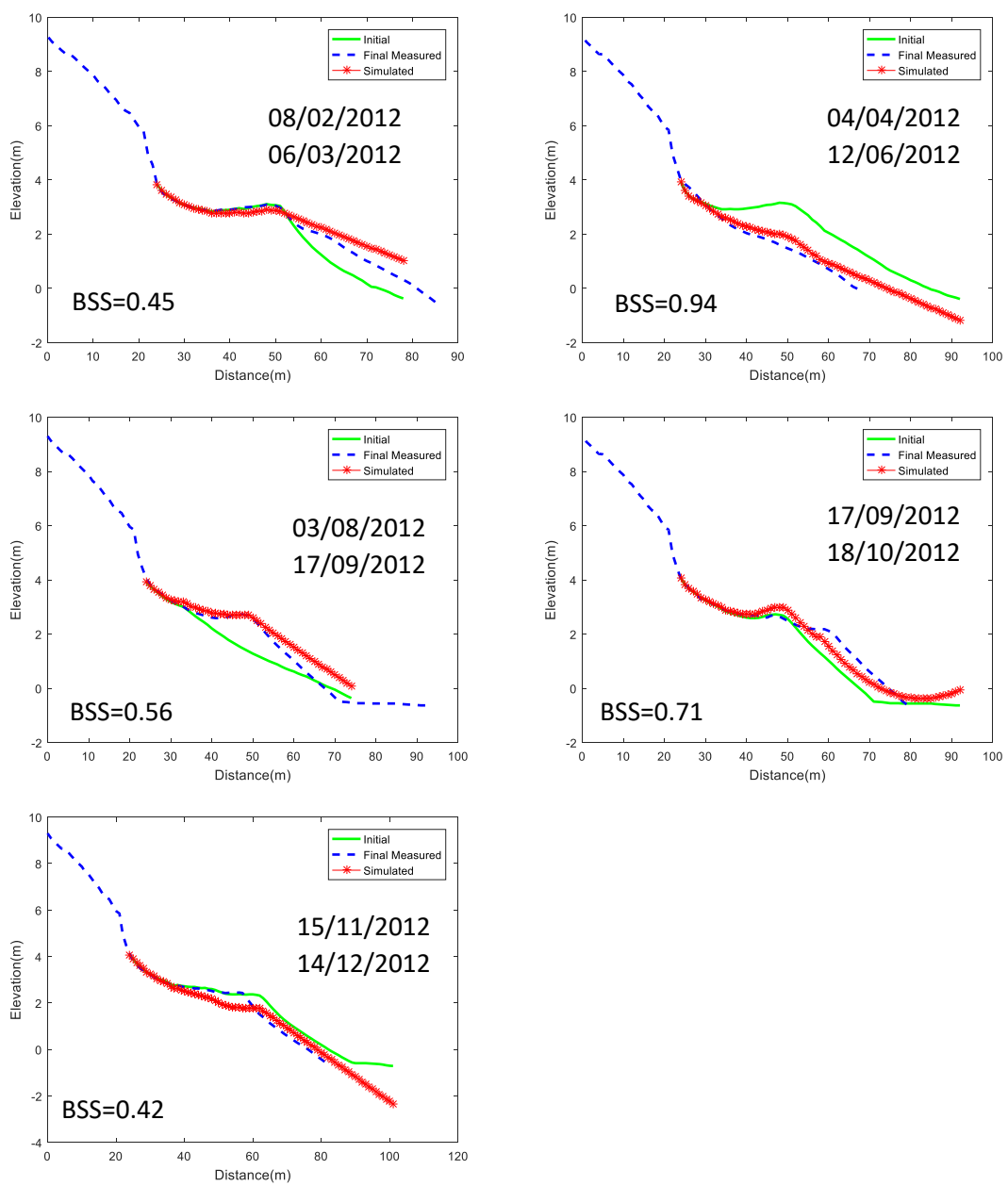


Figure 5-17 Monthly beach profile simulation results for 2012.

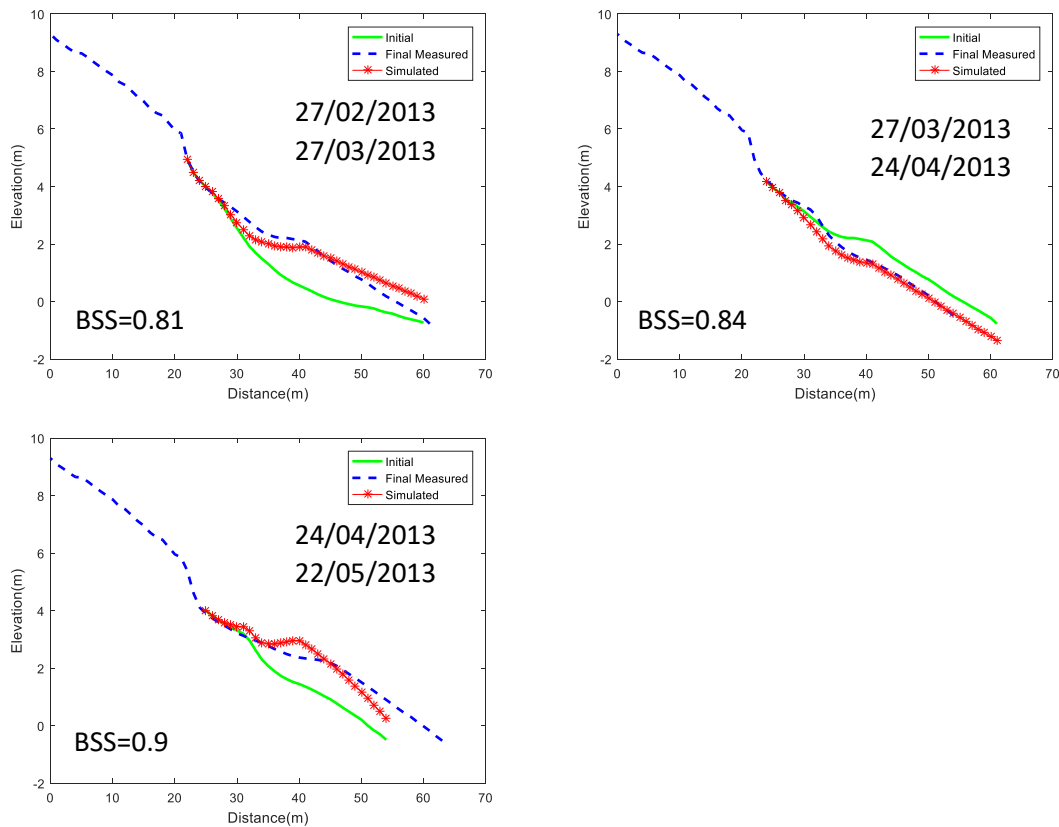


Figure 5-18 Monthly beach profile simulation results for 2013.

#### 5.5.2.4 Simulation for different periods

In order to evaluate the performance of the model, simulations were conducted based different durations from 2010 to 2013. Because the shortest period for the measurement is a month, in this study the shortest simulation period is monthly. However, because the beach profile behavior is seasonal (summer and winter), the longest period was 6-month simulation. In other words, beach profiles have sediment transport behavior changes every six-month based on the wave conditions. Figure 5-19 to 5- show the result of simulation for different durations. These figures show the entire profiles measured during each half year. Beach profiles within the half year are shown by P and indexes. Indexes indicate the order of measured profiles after initial measurement. Blues dash lines represent the last measurement for each half year.

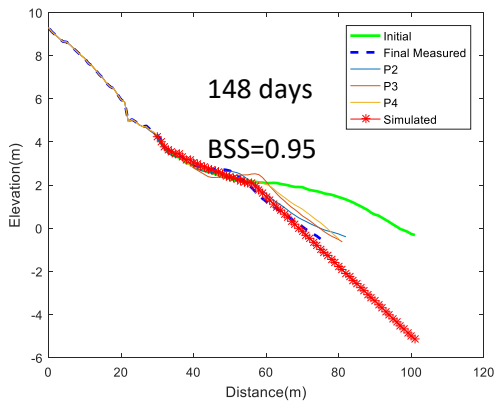
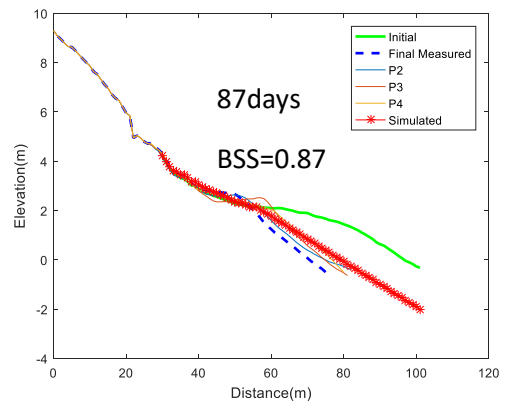
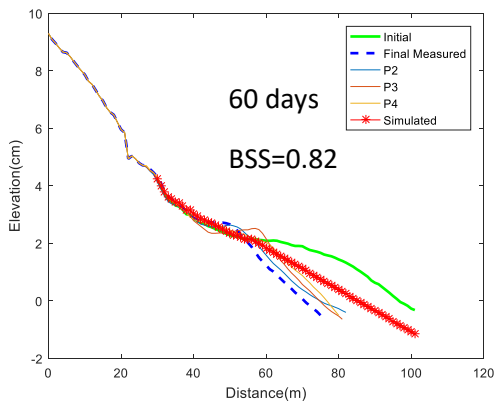
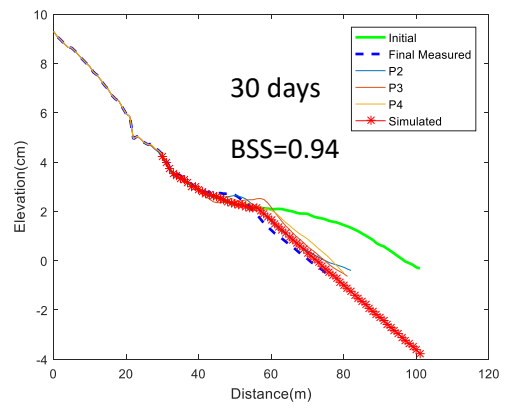
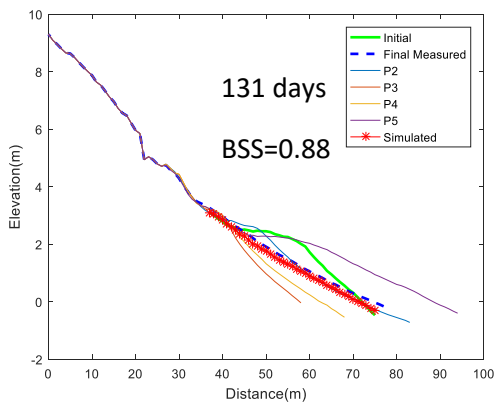
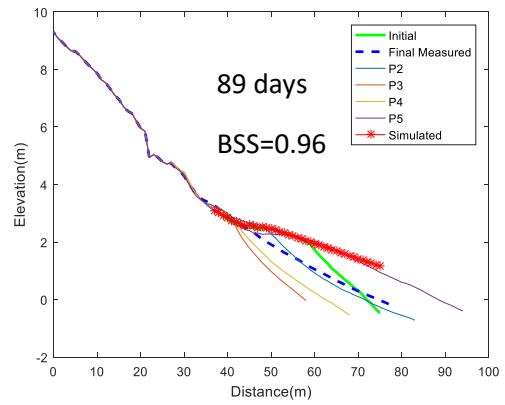
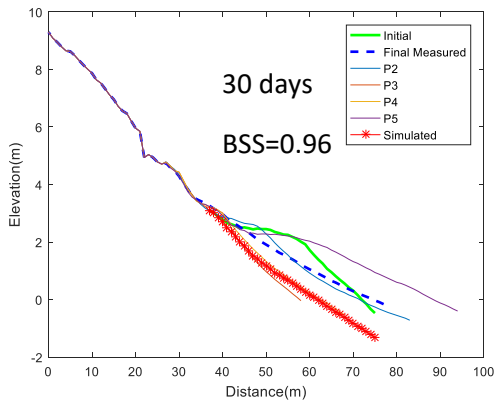


Figure 5-19 Beach profile simulation for different durations in 2010.

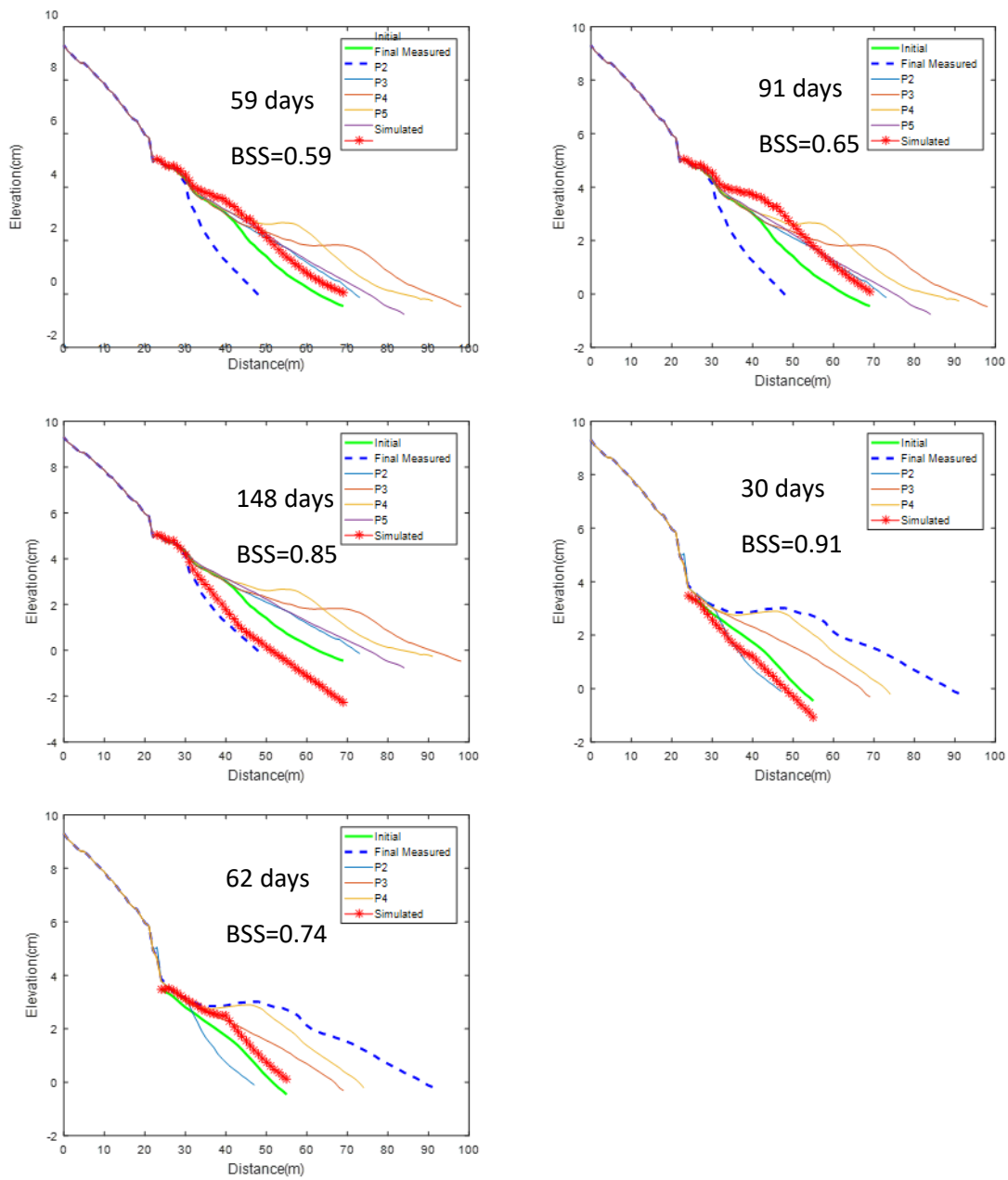


Figure 5-20 Beach profile simulation for different durations in 2011.

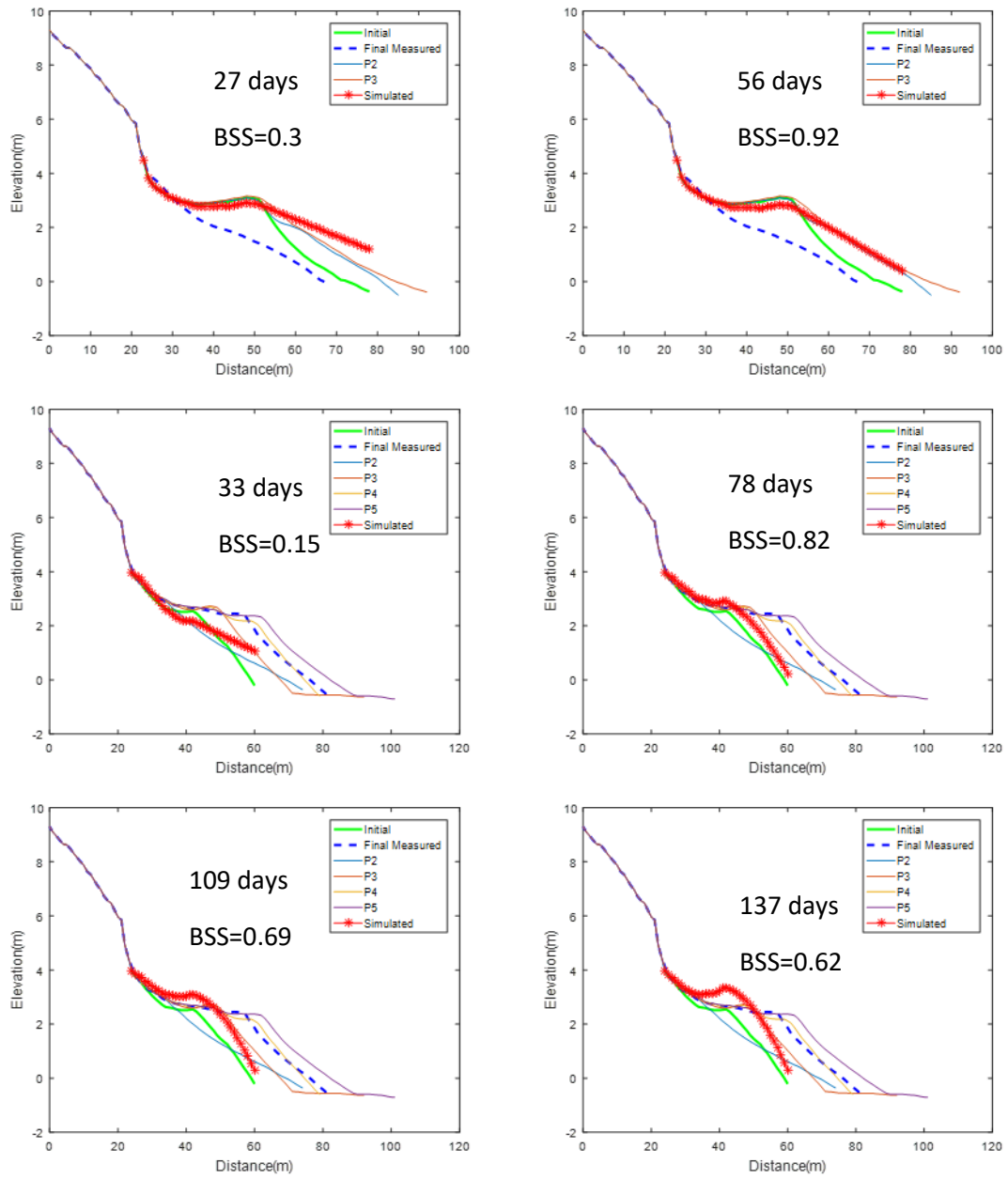


Figure 5-21 Beach profile simulation for different durations in 2012.

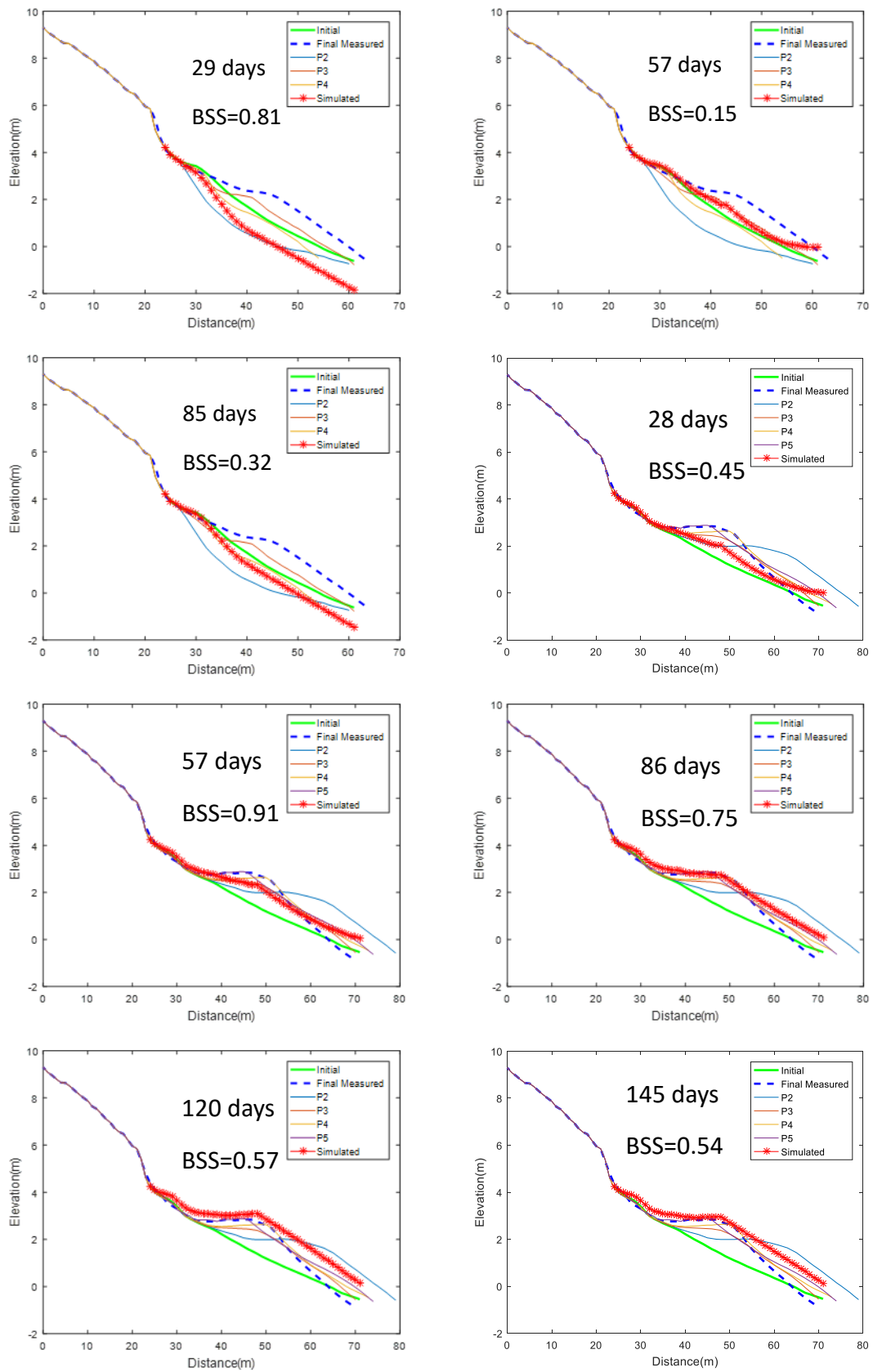


Figure 5-22 Beach profile simulation for different durations in 2013.

## 6 Conclusion

In the first part of this study, the response of sandbar as an important component of the beach profile to different hydrodynamic conditions under different sediment compaction levels was treated analytically. Observations in this research provided a more holistic understanding of the effect of sediment compaction on the pore water pressure gradient within the sediment layers.

A sandbar was created within a small-scale 2D wave flume. Eight different wave conditions, with a 10-minute duration, were generated to transform across the sandbar profile with high and low sediment compaction conditions. Vertical components of pore water pressure were measured using an array of four pressure transducers buried within the sandbar. Sand grains suspended by waves were monitored using a concentration meter during the experiment.

The results indicate that in contrast to pressure gradients, the magnitudes of maximum pore water pressure for trials with low sediment compaction conditions were larger than trials with high sediment compaction conditions. Additionally, the results revealed that the magnitudes of minimum pore water pressures had similar behavior to pressure gradients. In other words, maximum pressure gradients in all trials revealed larger values under high compaction sediment conditions but larger values for the minimum and maximum pore water pressures and minimum pressure gradients were not observed in some trials.

In each trial, the pore water pressure near the bed surface was higher than at the lower sediment layers. It was observed for both low and high sediment compaction conditions. The range of differences between the maximum and minimum pore water pressure became smaller for the lower sediment layers. It was more significant for pore water pressures induced by waves with the shorter periods.

The level of sediment compaction had a significant effect on pressure gradients. The rate of sediment compactions for the upper layer were observed almost the same for all trials. However, the rate of sediment compactions for the middle and top layers were up to about 2 and 1.6 times larger than the low compaction sediment conditions, respectively. Accordingly, the range of pressure gradients within sediments layers for high compaction conditions were varied from 1.1 to 1.8 times larger than low compaction conditions.

Depending on the pressure transducer positions and sediment compaction conditions, time lags between the measured pore water pressures were observed. These time lags can be due to both sediment compaction and the distance from the bed surface. Generally, the lower sediment layers showed larger time lags.

In this study, a fully statistical model was also used to investigate and simulate the interdependency of coastal parameters. Because the water level is one of the most important and well-known parameters for most coastal applications, this parameter and its effect on other coastal parameters should be considered. In addition, the effects of pressure gradient and acceleration on sediment transport mechanisms have been investigated extensively (e.g., Sleath, 1970; Madsen, 1978; Tabasi et al., 2021). To investigate the effects of different parameters on the sediment transport mechanism, Suzuki et al. (2009) and Mieras et al. (2017) conducted field measurements and large-scale experiments, respectively. The results highlighted the importance of the dependencies of  $\partial(P/\rho)/\partial x_{max}$ , and  $\partial u/\partial t_{max}$ . In this study, it was discovered that  $\eta_{max}$  can be used to correlate  $\partial(P/\rho)/\partial x_{max}$  and  $\partial u/\partial t_{max}$ . Moreover, among the variables, the dependence among  $(\eta_{max}, \partial u/\partial t_{max})$ ,  $(\eta_{max}, (P/\rho)/\partial x_{max})$ , and  $(\partial(P/\rho)/\partial x_{max}, \partial u/\partial t_{max})$  was significant.

The copula approach was used to simulate the abovementioned parameters. To obtain a reliable simulation, a group of TCDFs was utilized to fit the variables. Multivariate dependency structures were constructed and fitted with Archimedean

and elliptical copulas for  $(\eta_{max}, \partial u/\partial t_{max})$ ,  $(\eta_{max}, (P/\rho)/\partial x_{max})$ , and  $(\partial(P/\rho)/\partial x_{max}, \partial u/\partial t_{max})$  pairs. The KS test allowed us to assess the GOF and hence the performance of the models.

The AICc test results revealed that both Archimedean and elliptical copulas can generate and extrapolate correlated parameters using limited observational data. Because acquiring data from different coastal zones for a long period is an expensive process, the observational data were limited. Hence, laboratory experiments and statistical models suitable for calibration using limited measured data should be employed. It was discovered in this study that the laboratory dataset of multivariate  $(\eta_{max}, \partial(P/\rho)/\partial x_{max}, \partial u/\partial t_{max})$  can be applied to simulate the same natural conditions using normalized data. Hence, the results achieved by the statistical models were not site dependent.

The copula models selected for a specific site have the potential to be generalized for other case studies with the normal (non-storm) hydrodynamic condition. However, in addition to providing sufficiently accurate simulations, the models were based on a fully statistical approach, and physical constraints could not be considered for very different hydrodynamic and morphodynamic applications. Both the laboratory and field datasets were under normal wave conditions (non-storms) within the surf zone. Therefore, the results might not be valid for other zones, such as the swash zone under storms or other extreme conditions.

The numerical model conducted for the simulation of berm formation and erosion in the swash zone. The performance of model was evaluated using two field sets in Iran and Australia. Multiple erosion/formation couplets that appeared within the modeled period were simulated successfully. The simulation was conducted for various simulation periods from one month to six-month. The model was calibrated using two main sub-modules; wave criteria, and sediment transport module. The calibration results revealed that the model is very sensitive

to the wave criteria as calibration parameter and the result will be dramatically changed if inappropriate values are selected. It was figured out that the wave criteria value is very close to the average of values during the simulation periods. However, the model showed acceptable results after calibration procedure.

## 7 Reference

- Aagaard, T., Black, K. P., and Greenwood, B. (2002). Cross-shore suspended sediment transport in the surf zone: A field-based parameterization. *Mar. Geol.* 185, 283–302. doi:10.1016/S0025-3227(02)00193-7.
- Anderson, D., Cox, D., Mieras, R., Puleo, J. A., and Hsu, T. J. (2017). Observations of wave-induced pore pressure gradients and bed level response on a surf zone sandbar. *J. Geophys. Res. Ocean.* 122, 5169–5193. doi:10.1002/2016JC012557.
- Bacigál, T., Komorníková, M., and Komorník, J. (2019). State-of-the-art in modeling nonlinear dependence among many random variables with copulas and application to financial indexes. *J. Autom. Mob. Robot. Intell. Syst.* 13, 84–91. doi:10.14313/JAMRIS/3-2019/31.
- Bang Huseby, A., Vanem, E., and Natvig, B. (2013). A new approach to environmental contours for ocean engineering applications based on direct Monte Carlo simulations. *Ocean Eng.* 60, 124–135. doi:10.1016/j.oceaneng.2012.12.034.
- Berard, N. A., Mulligan, R. P., da Silva, A. M. F., and Dibajnia, M. (2017). Evaluation of XBeach performance for the erosion of a laboratory sand dune. *Coast. Eng.* 125, 70–80. doi:10.1016/j.coastaleng.2017.04.002.
- Bitner-Gregersen, E. M., and Haver, S. (1989). Joint long term description of environmental parameters for structural response calculation. in *2nd International Workshop on Wave Hindcasting and Forecasting* (Vancouver).
- Brown, S. A., Greaves, D. M., Magar, V., and Conley, D. C. (2016). Evaluation of turbulence closure models under spilling and plunging breakers in the surf zone. *Coast. Eng.* 114, 177–193. doi:10.1016/j.coastaleng.2016.04.002.

- Cheng, Z., Hsu, T. J., and Calantoni, J. (2017). SedFoam: A multi-dimensional Eulerian two-phase model for sediment transport and its application to momentary bed failure. *Coast. Eng.* doi:10.1016/j.coastaleng.2016.08.007.
- Clarindo, G., Teixeira, A. P., and Guedes Soares, C. (2021). Environmental wave contours by inverse FORM and Monte Carlo Simulation with variance reduction techniques. *Ocean Eng.* 228. doi:10.1016/j.oceaneng.2021.108916.
- Condon, A. J., and Sheng, Y. P. (2012). Optimal storm generation for evaluation of the storm surge inundation threat. *Ocean Eng.* 43, 13–22. doi:10.1016/j.oceaneng.2012.01.021.
- Corbella, S., and Stretch, D. D. (2013). Simulating a multivariate sea storm using Archimedean copulas. *Coast. Eng.* doi:10.1016/j.coastaleng.2013.01.011.
- Dawson, T. H., Kriebel, D. L., and Wallendorf, L. A. (1993). Breaking waves in laboratory-generated JONSWAP seas. *Appl. Ocean Res.* 15, 85–93. doi:10.1016/0141-1187(93)90023-Q.
- De Michele, C., Salvadori, G., Passoni, G., and Vezzoli, R. (2007). A multivariate model of sea storms using copulas. *Coast. Eng.* doi:10.1016/j.coastaleng.2007.05.007.
- De Waal, D. J., and Van Gelder, P. H. A. J. M. (2005). Modelling of extreme wave heights and periods through copulas. *Extremes* 8, 345–356. doi:10.1007/s10687-006-0006-y.
- Edwards, S. J., Troesch, A. W., and Collette, M. (2021). Estimating extreme characteristics of stochastic non-linear systems. *Ocean Eng.* 233. doi:10.1016/j.oceaneng.2021.109042.
- Faria, A. F. G., Thornton, E. B., and Stanton, T. P. (1997). Small-scale morphology related to wave and current parameters over a barred beach. in *Proceedings of the Coastal Engineering Conference*, 3391–3404.

doi:10.1061/9780784402429.262.

- Forristall, G. Z. (2000). Wave crest distributions: Observations and second-order theory. *J. Phys. Oceanogr.* doi:10.1175/1520-0485(2000)030<1931:WCDOAS>2.0.CO;2.
- Garcia-Jorcano, L., and Benito, S. (2020). Studying the properties of the Bitcoin as a diversifying and hedging asset through a copula analysis: Constant and time-varying. *Res. Int. Bus. Financ.* 54. doi:10.1016/j.ribaf.2020.101300.
- Jane, R., Dalla Valle, L., Simmonds, D., and Raby, A. (2016). A copula-based approach for the estimation of wave height records through spatial correlation. *Coast. Eng.* 117, 1–18. doi:10.1016/j.coastaleng.2016.06.008.
- Katoh, K., and Yanagishima, S. ichi (1995). Changes of sand grain distribution in the surf zone. in *Coastal Dynamics - Proceedings of the International Conference*.
- Kwon, H. H., and Lall, U. (2016). A copula-based nonstationary frequency analysis for the 2012–2015 drought in California. *Water Resour. Res.* 52, 5662–5675. doi:10.1002/2016WR018959.
- Li, F., Gelder, P. H. A. J. M. va., Vrijling, J. K., Callaghan, D. P., Jongejan, R. B., and Ranasinghe, R. (2014a). Probabilistic estimation of coastal dune erosion and recession by statistical simulation of storm events. *Appl. Ocean Res.* doi:10.1016/j.apor.2014.01.002.
- Li, F., van Gelder, P. H. A. J. M., Ranasinghe, R., Callaghan, D. P., and Jongejan, R. B. (2014b). Probabilistic modelling of extreme storms along the Dutch coast. *Coast. Eng.* doi:10.1016/j.coastaleng.2013.12.009.
- Lin, Y., Dong, S., and Tao, S. (2020). Modelling long-term joint distribution of significant wave height and mean zero-crossing wave period using a copula mixture. *Ocean Eng.* 197. doi:10.1016/j.oceaneng.2019.106856.

- Lowe, R. J., Buckley, M. L., Altomare, C., Rijnsdorp, D. P., Yao, Y., Suzuki, T., et al. (2019). Numerical simulations of surf zone wave dynamics using Smoothed Particle Hydrodynamics. *Ocean Model.* doi:10.1016/j.ocemod.2019.101481.
- Madsen, O. S. (1978). Wave-Induced Pore Pressures and Effective Stresses in a Porous Bed. *Geotechnique* 28, 377–393. doi:10.1680/geot.1978.28.4.377.
- MADSEN, O. S. (1974). Stability of a Sand Bed Under Breaking Waves. *Proc. 14Th. Asce Coast. Engng. Conf. (Copenhagen, Denmark).* 2, 776–794. doi:10.1061/9780872621138.048.
- Mariño-Tapia, I. J., Russell, P. E., O’Hare, T. J., Davidson, M. A., and Huntley, D. A. (2007). Cross-shore sediment transport on natural beaches and its relation to sandbar migration patterns: 1. Field observations and derivation of a transport parameterization. *J. Geophys. Res. Ocean.* 112. doi:10.1029/2005JC002893.
- Mieras, R. S., Puleo, J. A., Anderson, D., Cox, D. T., and Hsu, T. J. (2017a). Large-scale experimental observations of sheet flow on a sandbar under skewed-asymmetric waves. *J. Geophys. Res. Ocean.* 122, 5022–5045. doi:10.1002/2016JC012438.
- Mieras, R. S., Puleo, J. A., Anderson, D., Cox, D. T., and Hsu, T. J. (2017b). Large-scale experimental observations of sheet flow on a sandbar under skewed-asymmetric waves. *J. Geophys. Res. Ocean.* doi:10.1002/2016JC012438.
- Mieras, R. S., Puleo, J. A., Anderson, D., Hsu, T. J., Cox, D. T., and Calantoni, J. (2019). Relative Contributions of Bed Load and Suspended Load to Sediment Transport Under Skewed-Asymmetric Waves on a Sandbar Crest. *J. Geophys. Res. Ocean.* 124, 1294–1321. doi:10.1029/2018JC014564.
- Myrhaug, D., Ong, M. C., and Holmedal, L. E. (2015). Suspended sediments due to random waves including effects of second order wave asymmetry and

- boundary layer streaming. *Ocean Eng.* doi:10.1016/j.oceaneng.2015.05.022.
- Nelsen, R. B. (2006). *An Introduction to Copulas*. doi:10.1007/0-387-28678-0.
- Plackett, R. L. (1965). A Class of Bivariate Distributions. *J. Am. Stat. Assoc.* 60, 516–522. doi:10.1080/01621459.1965.10480807.
- Repko, A., Van Gelder, P. H. A. J. M., Voortman, H. G., and Vrijling, J. K. (2004). Bivariate description of offshore wave conditions with physics-based extreme value statistics. *Appl. Ocean Res.* doi:10.1016/j.apor.2004.10.001.
- Ruggiero, P., Walstra, D. J. R., Gelfenbaum, G., and van Ormondt, M. (2009). Seasonal-scale nearshore morphological evolution: Field observations and numerical modeling. *Coast. Eng.* 56, 1153–1172. doi:10.1016/j.coastaleng.2009.08.003.
- Ryabkova, M., Karaev, V., Guo, J., and Titchenko, Y. (2019). A Review of Wave Spectrum Models as Applied to the Problem of Radar Probing of the Sea Surface. *J. Geophys. Res. Ocean.* 124, 7104–7134. doi:10.1029/2018JC014804.
- Salvadori, G., De Michele, C., and Durante, F. (2011). On the return period and design in a multivariate framework. *Hydrol. Earth Syst. Sci.* doi:10.5194/hess-15-3293-2011.
- Salvadori, G., Durante, F., De Michele, C., Bernardi, M., and Petrella, L. (2016). A multivariate copula-based framework for dealing with hazard scenarios and failure probabilities. *Water Resour. Res.* doi:10.1002/2015WR017225.
- Schmidt, T. (2006). “Coping with Copulas,” in *Copulas - From Theory to Applications in Finance*, 1–23.
- Scott, C. P., Cox, D. T., Maddux, T. B., and Long, J. W. (2005). Large-scale laboratory observations of turbulence on a fixed barred beach. *Meas. Sci. Technol.* doi:10.1088/0957-0233/16/10/004.

- Sellés Valls, S. (2019). A vine-based approach for defining critical infrastructure loads. Available at: <https://repository.tudelft.nl/islandora/object/uuid%3A9a133d6d-00ca-4fcc-a244-b88215dfd578>.
- Shields, A. (1936). Anwendung der Aehnlichkeitsmechanik und der Turbulenzforschung auf die Geschiebebewegung. *Technology* 26, 26.
- Sklar, A. (1959). Fonctions de Répartition a n Dimensions et Leurs Marges. *Publ. l'Institute Stat. l'Universite Paris*.
- Sleath, J. F. A. (1970). Wave-Induced Pressures in Beds of Sand. *J. Hydraul. Div.* 96, 367–378. doi:10.1061/jyceaj.0002325.
- Sleath, J. F. A. (1999). Conditions for plug formation in oscillatory flow. *Cont. Shelf Res.* 19, 1643–1664. doi:10.1016/S0278-4343(98)00096-X.
- Suzuki, T., Inami, Y., Yanagishima, S., Sakihama, S., and Cox, D. (2018). OBSERVATIONS OF SEDIMENT PARTICLE MOVEMENTS UNDER ACCRETIVE WAVE CONDITIONS. *Coast. Eng. Proc.* doi:10.9753/icce.v36.sediment.68.
- Suzuki, T., Mori, N., and Cox, D. T. (2009a). Statistical modeling of near-bed pressure gradients measured on a natural beach. *Coast. Eng. J.* doi:10.1142/S0578563409001965.
- Suzuki, T., Mori, N., and Cox, D. T. (2009b). Statistical modeling of near-bed pressure gradients measured on a natural beach. *Coast. Eng. J.* 51, 101–121. doi:10.1142/S0578563409001965.
- Suzuki, T., Shin, S., Cox, D. T., and Mori, N. (2010). Spatiotemporal Characteristics of Near-Bed Pressure Gradients on a Barred Beach. *J. Waterw. Port, Coastal, Ocean Eng.* 136, 327–336. doi:10.1061/(asce)ww.1943-5460.0000055.

- SWART, D. H. (1974). Offshore Sediment Transport and Equilibrium Beach Profiles.
- Tabasi, M., Soltanpour, M., Suzuki, T., and Jayaratne, R. (2020). Modeling of Berm Formation and Erosion At the Southern Coast of the Caspian Sea. *Coast. Eng. Proc.*, 19. doi:10.9753/icce.v36v.papers.19.
- Tabasi, M., Yamada, M., and Suzuki, T. (2021). Laboratory Investigation of the Influence of Sediment Compaction on Wave-Induced Pore Pressure Gradient and Sediment Concentration for a Sandbar. *J. Japan Soc. Civ. Eng.* 77.
- Tayfun, M. A., and Fedele, F. (2007). Wave-height distributions and nonlinear effects. *Ocean Eng.* doi:10.1016/j.oceaneng.2006.11.006.
- Vrijling, J. K., and Bruinsma, J. (1980). No Title. in *Hydraulic boundary conditions* (Hydraulic aspects of coastal structures), 109–133.
- Wahl, T., Jensen, J., and Mudersbach, C. (2011). A MULTIVARIATE STATISTICAL MODEL FOR ADVANCED STORM SURGE ANALYSES IN THE NORTH SEA. *Coast. Eng. Proc.* doi:10.9753/icce.v32.currents.19.
- Wahl, T., Mudersbach, C., and Jensen, J. (2012). Assessing the hydrodynamic boundary conditions for risk analyses in coastal areas: A multivariate statistical approach based on Copula functions. *Nat. Hazards Earth Syst. Sci.* doi:10.5194/nhess-12-495-2012.
- Wang, P., Smith, E. R., and Ebersole, B. A. (2002). Large-scale laboratory measurements of longshore sediment transport under spilling and plunging breakers. *J. Coast. Res.*
- Wilson, K. C. (1989). Friction of wave-induced sheet flow. *Coast. Eng.* 12, 371–379. doi:10.1016/0378-3839(89)90013-6.
- Zachary, S., Feld, G., Ward, G., and Wolfram, J. (1998). Multivariate extrapolation in the offshore environment. *Appl. Ocean Res.* 20, 273–295. doi:10.1016/S0141-1187(98)00027-3.